Three-dimensional Nanostructures Fabricated by Ion-Beam-Induced Deposition

PhD Thesis

Three-dimensional Nanostructures Fabricated by Ion-Beam-Induced Deposition

proefschrift

ter verkrijging van de graad van doctor aan de Technische Universiteit Delft op gezag van de Rector Magnificus Prof. ir. K. C. A. M. Luyben, voorzitter van het College voor Promoties in het openbaar te verdedigen op woensdag 6 oktober 2010 om 14:00 uur

 door

Ping Chen

Master of Electronic Engineering Tsinghua University, China geboren te Jiangxi, China Dit proefschrift is goedgekeurd door de promotor:

Prof. dr. H. W. M. Salemink

Copromotor:

Dr. P. F. A. Alkemade

Samenstelling promotiecommissie:

Rector Magnificus

Prof. dr. H. W. M. Salemink Dr. P. F. A. Alkemade Prof. dr. ir. P. Kruit Prof. dr. K. K. Berggren Prof. dr. U. Stauffer Dr. ir. J. J. L. Mulders

Dr. ir. D. J. Maas

Prof. dr. H. W. Zandbergen

voorzitter

Technische Universiteit Delft, promotor Technische Universiteit Delft, copromotor

Technische Universiteit Delft

Massachusetts Institute of Technology, USA

Technische Universiteit Delft

FEI company

TNO Science and Industry

Technische Universiteit Delft, reservelid

Keywords: three-dimensional nanostructures, ion-beam-induced deposition

Cover page: Pt IBID of "Li Bai Strolling and Chanting a Poem" painting by Liang Kai (13th century, South Song Dynasty). Li Bai, a poet (8th century, Tang Dynasty).

Casimir PhD-series, Delft-Leiden, 2010-27

ISBN/AEN 978-94-6108-094-3

Copyright © 2010 by P. Chen

All rights reserved. No part of the material protected by this copyright notice may be reproduced or utilized in any form or by any means, electronic or mechanical, including photocopying, recording or by any information storage and retrieval system, without written permission from the author.

The research described in this thesis was performed at the Kavli Institute of Nanoscience at the faculty Applied Sciences, Delft University of Technology.







This research was supported by NanoNed, a national nanotechnology program coordinated by the Dutch Ministry of Economic Affairs (project number DTF 7093).

Abstract

The direct writing technology known as ion-beam-induced deposition (IBID) has been attracting attention mainly because of its high degree of flexibility of locally prototyping three-dimensional (3D) nanostructures. These high-resolution nanostructures have various research applications. However, no systematic study of the capability of IBID to fabricate 3D nanostructures has been published to date. This is partly caused by the lack of suitable methods to monitor and to access the numerous time-varying process parameters and our lacking overview of the interplay between the relevant parameters. This thesis partially aims to fill this gap. This thesis mainly includes three parts:

- (1) Exploration of the limits of IBID to fabricate nanopillars. Firstly to fabricate IBID pillars in a controllable and reproducible manner, we have studied the optimization of the pillar growth conditions. With the conventional Ga⁺ FIB and the novel He⁺ FIB approaches, the influence of precursor surface density and of the ion beam interaction have been investigated, respectively. Moreover, relevant simulation work is discussed to explain the interplay between vertical and lateral growth and their dependence on precursor depletion and replenishment. Combining these results, a comparison between Ga⁺ and He⁺ IBID pillar growth is made. Secondly, to improve the quality of IBID pillars, we have studied the formation of the irregular sidewall surface and the halo viz. the deposits around the bases of a typical Ga⁺ IBID pillar by comparing pillars grown on either an insulating Si₃N₄ membrane or on a semiconducting Si wafer. Thirdly, by changing the substrate properties and the distance between neighboring pillars, we have studied the proximity effect in IBID pillar growth. This proximity effect is important when fabricating dense pillar arrays. The proximity effect of He⁺ IBID is similar to that of Ga⁺ IBID, though the trend is much less pronounced.
- (2) Exploration of the limits of IBID to fabricate nanopores in thin membranes. We have demonstrated that sub-10-nm-diameter nanopores in a $\rm Si_3N_4$ membrane can be fabricated in a single $\rm Ga^+$ IBID step by carefully adjusting the ion beam and gas exposure conditions. This is accomplished by exploiting the competition between sputtering and deposition processes during IBID. Apart from the simplicity and the speed, another advantage is a broad choice of material for the deposit and the membrane. At various stages of pore formation we have studied the chemical composition and the shape of the pore, which are the factors that determine the functionalization of the nanopores. For this purpose, energy dispersive x-ray (EDX), electron energy

loss spectroscopy (EELS) analysis have been used for determining the chemical composition, and 3D electron tomography for determining the shape of the pore. It is found that the chemical structure in the rim of the pore depends on the properties of the precursor gas. Furthermore, simulation shows that the forward and the backward sputtering depend differently on membrane thickness. This difference can also play a role in the pore formation and shrinkage.

(3) Study of the IBID process mechanisms. We have done a series of experiments to distinguish the roles of different mechanisms involved in IBID. Firstly we have found a significant contribution of secondary particles to Ga⁺ IBID. This result was obtained by comparing the volume of a deposited box with that of the material deposited onto a nearby sidewall. Subsequently we have investigated two models that describe IBID in terms of the impact of secondary electrons and of sputtered atoms, respectively. For this purpose, the yields of deposition, sputtering, and secondary electron emission as well as the energy spectra of the secondary electrons were measured in situ during Ga⁺ IBID as functions of ion incident angle and energy. The results indicate that the sputtered atom model describes Ga⁺ IBID better than the secondary electron model. I also briefly discuss the contribution of primary ions. Based on these results, we review the studies on the mechanisms of IBID with Ga⁺ or He⁺ ion beams and EBID mechanisms reported in the literature. I conclude that IBID has to be described by multiple mechanisms. The dominating mechanism is in Ga⁺ IBID related to sputtering, while in He⁺ IBID and EBID to secondary electron emission.

In this thesis work, we have studied the capability of IBID to grow 3D nanostructures. Future efforts, for instance improvement of the purity of the deposits, will be necessary to functionalize IBID nanostructures.

Contents

1	Inti	oduct	ion	1
	1.1	Nanot	sechnology	2
	1.2	Nanof	abrication	3
		1.2.1	Optical lithography	3
		1.2.2	Next-generation lithography	4
		1.2.3	Beyond next-generation lithography: Maskless and resistless	
			techniques	6
	1.3	3D na	nofabrication by IBID	12
		1.3.1	State-of-the-art and applications	12
		1.3.2	Fundamentals of IBID	13
	1.4	Outlin	ne of this dissertation	22
2	Set	ups an	d methods	25
	2.1	Abstra	act	25
	2.2		EM DualBeam system: FEI STRATA 235	26
	2.3	Heliur	m Ion Microscopy: Carl Zeiss Orion TM plus SHIM	26
	2.4	Addit	ional accessories for tuning the substrate bias and temperature .	28
3	Nar	nopilla	r growth by IBID	31
	3.1		act	31
	3.2		luction	33
		3.2.1	Process dependences of IBID pillar growth	33
		3.2.2	Formation of rough sidewalls and halos by Ga ⁺ IBID	34
		3.2.3	Proximity effect in IBID of pillars	35
	3.3	Exper	imental	35
	3.4		ss dependences of IBID pillar growth	39
		3.4.1	Pillar growth by Ga ⁺ IBID	39
		3.4.2	Pillar growth by He ⁺ IBID	43
		3.4.3	Comparison of Ga ⁺ and He ⁺ IBID pillar growth	43
		3.4.4	Discussion	46
	3.5	Forma	ation of rough sidewalls and halos by Ga ⁺ IBID	56
		3.5.1	Pillars grown on Si and Si_3N_4	58
		3.5.2	Discussion	59
	3.6	Proxir	mity effect in IBID of pillars	63
		3.6.1	Proximity effect in Ga ⁺ IBID of pillars	63
		3.6.2	Proximity effect in He ⁺ IBID of pillars	68

		3.6.3 Discussion	69	
	3.7	Conclusions	74	
4 Fabrication and characterization of IBID nanopores				
-	4.1	Abstract	77 77	
	4.2	Introduction	79	
	4.3	Experimental	80	
	4.4	Fast single-step fabrication of nanopores by IBID	81	
	1.1	4.4.1 Beam current dependence of nanodot or nanopore fabrication on a Si_3N_4 membrane	81	
		4.4.2 Dwell time dependence of nanopore fabrication with CPC and TEOS precursors	81	
		4.4.3 Exposure time dependence of nanopore fabrication with CPC and TEOS precursors	81	
		4.4.4 Investigation of the geometry of IBID nanopores	82	
		4.4.5 Discussion	82	
	4.5	TEM study of nanopores fabricated by IBID	88	
	4.0	4.5.1 EDX & EFTEM analysis and 3D electron tomography of nanopore		
		fabricated by FIB milling and by IBID with CPC precursor	-88	
		4.5.2 EDX & EFTEM analysis of nanopores fabricated by IBID with	00	
		TEOS precursor	93	
		4.5.3 SRIM simulation	94	
		4.5.4 Discussion	94	
	4.6	Conclusions	96	
5	Mu	ltiple mechanisms of IBID	97	
9	5.1	Abstract	97	
	5.2	Introduction	99	
	5.3	Experimental	100	
	5.4	Contributions of secondary particles in IBID mechanisms	101	
	5.5	Roles of secondary electrons and sputtered atoms in IBID mechanisms	103	
	3.3	5.5.1 Incident ion energy and angular dependences of the yields of deposition, sputtering, and secondary electron emission during	100	
		IBID	103	
		5.5.2 Incident ion energy and angular dependences of the energy spec-		
		trum of secondary electrons emitted during IBID	106	
	5.6	Contribution of primary ions in IBID mechanisms	106	
	5.7	Discussion	107	
	5.8	Conclusions	109	
Sı	ımm	ary	111	
Sa	men	vatting	113	
Bi	Bibliography 1			
\mathbf{Li}	List of publications			

Curriculum Vitae	139
Acknowledgments	141



Chapter 1

Introduction

This chapter provides a general introduction of the direct-write technology known as ion-beam-induced deposition (IBID) by discussing broader research fields which encompass IBID. First, a brief introduction of the fields of nanotechnology is given. Then follows a sequential introduction of nanofabrication techniques including conventional optical lithography, next generation lithographies (mask-based approaches), and maskless techniques before turning to IBID. In particular, an overview is given on the applications of IBID three-dimensional (3D) nanostructures and the importance of a systematic study of the limits of IBID 3D nanofabrication. Subsequently, the fundamentals of IBID and especially the determining factors of IBID for 3D nanofabrication are discussed in detail. The chapter ends with an outline of this dissertation.

1.1 Nanotechnology

Nanotechnology is defined as manipulation, fabrication and utilization of any matter having a size of 100 nanometers or less at least in one dimension. The term "nanotechnology" was coined in 1974 [1]. Since then, nanotechnology has attracted widespread attention and has become a collective term for scores of technologies and techniques. The label of "nano-" has become attached to more and more subject areas, including nanomaterials, nanoeletronics, nanomechanics, nanophotonics, nanomedicince, to name but a few. Today, almost every major research institution throughout the world has announced its activities in some field of nanotechnology. In our everyday lives, there are various commercial products which use the term nanotechnology, ranging from the fields of information, medicine, environment, and even consumer goods.

We cannot recall the history of nanotechnology without mentioning the seminal talk "There is plenty of room at the bottom" [2] by Richard Feynman, who would later become a Nobel laureate. It might be not completely true to say that Feynman's talk gave birth to nanotechnology, however, it is surely fair enough to conclude that it predicted and catalyzed the development of nanotechnology and inspired many researchers. In his talk, Feynman described a field of "manipulating and controlling things on a small scale". He emphasized the importance of this new field, saying "a point that is most important is that it would have an enormous number of technical applications". He predicted that things can be miniaturized by scaling their size smaller and smaller by stripping away unwanted material to produce the desired structures. This would subsequently be called the top-town approach. Feynman also introduced the possibility of the bottom-up approach which starts with materials from the atomic or molecular level, allowing them to self-assemble into useful nanostructures. It is amazing to see how many of the concepts Feynman talked about have actually been established and developed into very important and diverse scientific and technical fields today. Some are nanofabrication technologies: electron- and ion-beam fabrication such as electron- and ion- projection lithography (EPL and IPL), molecular-beam epitaxy (MBE), nanoimprint lithography (NIL), scanning probe techniques such as scanning tunneling microscopy (STM) and atomic force microscopy (AFM). The rest are integrated circuits (also known as ICs, or silicon chips), micro-/nano-electro mechanical systems (MEMS/NEMS), spintronics, quantum-effect electronics and nanobiotechnology.

Nanotechnology has made huge progress over the past 30 years. Some subject areas have already achieved huge success in applications, for instance IC industry. Nevertheless, many are still in their early stages of research, for instance quantum computers.

1.2 Nanofabrication

A key to nanotechnology is fabricating functional nanostructures with arbitrary patterns. After the transistor was invented in 1947, the IC industry has been the main driving force for pushing the limits of nanofabrication techniques. Following the so-called Moore's law, the critical length of IC devices has shrunk at a rate of 30% every three years. Today, it is already as small as 32 nm. In 2005, the International Technology Roadmap for Secomiconductors (ITRS) suggested that the features in complementary metal-oxide-semiconductors (CMOS) would shrink to at least 22 nm [3]. As it comes closer and closer to the limits of optical lithography, a variety of emerging nanofabrication techniques have been studied [4–6]. The main reasons optical lithography can survive in the IC industry are that it can be used in a parallel process which guarantees a high throughput, and the inventions of phase-shift masks and immersion lithography. Any technique that competes with optical lithography has to work in a parallel process usually involving masks and resists. However, with decreasing feature sizes, mask fabrication has caused more and more engineering difficulties. Therefore, maskless or even resistless approaches have been investigated. So far, most maskless techniques have been applied only for the purpose of research and prototyping. In other words, they only fulfill academic requirements.

1.2.1 Optical lithography

Lithography technology has been applied in the semiconductor industry since IC was invented in 1958. The basic idea of optical lithography is using light to transfer a geometric 2D pattern from a mask to a light-sensitive chemical resist, which is coated on the substrate. Afterwards, a series of chemical treatments engraves the exposure pattern into the material underneath the resist to form a 3D nanostructure. This technology soon migrated to optical projection lithography to avoid the defects caused by the repeated contact of the mask and the resist and to improve the resolution and overlay. After passing through the mask, the light goes through a lens system that projects the light to create a demagnified image of the mask on a resist-coated substrate. The resolution of optical lithography is limited by the wavelength of light because of the optical diffraction. The wavelength of exposure light is decreased to produce smaller feature sizes [4]. At its early stage, lithography used visible G-line (436 nm) and I-line (365 nm) wavelengths produced by mercury arc lamps, then excimer lasers at deep ultraviolet (DUV) 248 nm KrF and 193 nm ArF. Until 2009, state-of-art lithography was a combination of 193 nm lithography and immersion technology in which water is used as an immersion medium between the lens and the wafer surface to have a high dielectric, concentrating medium for the light-path. It has already taken the minimum feature size down to 32 nm. However, this technology is unlikely to be suitable beyond the 32 nm node due to extreme challenges such as alignment and overlay accuracy as well as the lack of high-index materials and immersion liquids.

1.2.2 Next-generation lithography

With decreasing feature sizes and increasing wafer sizes, to overcome the diffraction limits of optical lithography, shorter wavelength lithography using 157 nm, extreme ultraviolet (EUV) at 13.5 nm, x-ray at ~1 nm, and even shorter wavelengths of electron and ion beams (for instance, 0.01 nm for 10 kV electrons) have been studied. In addition, a technique called nanoimprinting lithography (NIL) has the parallel patterning capability of optical lithography. In NIL, the shape of a rigid mold (usually silicon) is replicated into a resist (usually polymer) coated on a hard substrate by mechanical contact [7]. All of these techniques are known as next-generation lithography (NGL) candidates. Electron projection lithography (EPL) was most popular during the 1970s, but was replaced by X-ray lithography (XRL) during the 1980s and early 1990s, and then by EUV lithography from the mid-1990s till today. NIL's popularity is rising, and is positioned to succeed EUVL as the NGL of choice. Ion projection lithography (IPL) has a niche market in defect repair.

Extreme ultraviolet lithography (EUVL) and X-ray lithography (XRL)

The maturation of immersion technology delayed the development of EUVL and caused the semiconductor industry to abandon 157 nm lithography because 157 nm can only last one generation of IC manufacturing. Today, EUVL is widely accepted as the most promising NGL for the 32 nm node and beyond [5, 8]. In many aspects, EUVL retains the image of optical lithography in practice, though EUV at 13 nm wavelength actually should be called soft X-ray. However, the conventional refractive optics do not work for EUVL because of their strong absorption in virtually all types of materials. Instead, reflective mirrors have to be used for both masks and focusing optics. Up to now, fabrication of sub-30 nm features has been demonstrated. The lithography company ASML has announced that it is on track to ship its first EUVL tools in 2010. However, many critical challenges still exist: developing reliable EUV sources with high output power and sufficient lifetime, controlling contamination of projection and illuminator optics, developing defect-free masks, developing resists with high resolution and sensitivity. All these factors make it difficult for EUVL to replace optical lithography in the near future.

XRL was supposed to be an ideal candidate for NGL due to its short wavelength. However, X-ray masks are so expensive that they have ended XRLs prospects [4].

Electron projection lithography (EPL) and ion projection lithography (IPL)

In EPL, electrons that are extracted from a source and collimated through a mask are accelerated through a series of electrostatic lenses that project the electrons to create a demagnified image of the mask on a resist-coated substrate. Owing to the negligible wavelength of electrons (for instance, 0.01 nm for 10 kV electron beam), the resolution of EPL is mostly limited by lens aberrations, not by diffraction as in

optical projection lithography. As a consequence, EPL can offer a higher resolution. On the other hand, mask-based EPL has increased throughput significantly compared to beam-based direct writing. Since the early 1990s, types of EPL systems have been developed: the cell projection system by Hitachi (HL-800D) [9], the scattering with angular limitation projection e-beam lithography (SCALPEL) by Lucent Technologies [10], and the projection reduction exposure with variable axis immersion lens (PREVAIL) by IBM [11]. Nikon has achieved a resolution of 70 nm for dense lines and 50 nm for isolated lines [12]. However, a key engineering difficulty is still the mask. Typical masks used in EPL are the stencil type [9, 11] or the membrane type [10]. Both types are difficult to make, inspect, and repair. A key fundamental difficulty is the space charge effect (particle-particle repulsion), which is especially serious considering the high current needed in EPL.

In parallel with the development of EPL, another charged-particle-based projection lithography known as ion projection lithography (IPL) has also attracted considerable attention since the late 1990s [13–16]. In IPL, collimated ions, instead of electrons, are used. IPL has several advantages over EPL [13, 17]. The resists are normally two orders of magnitude more sensitive to ions than to electrons, because in the 1-200 keV energy range ions lose most of their energy in the resist whereas electrons pass through the resist but lose little energy. Ions, particularly the light ions H⁺, H₂ and He⁺ used in IPL systems, suffer little or no scattering in the resist and substrate; hence they exhibit a much weaker proximity effect than electrons, which have a proximity effect of a few tens of micrometers. In addition, the penetration depth of ions can be easily adjusted by the ion energy. Thus, high-aspect-ratio and multi-layer structures can be relatively easily fabricated by IPL. In the late 1980s, IMS Nanofabrication developed the first generation of IPL systems, called the ion projection lithography machine (IPLM), which was already able to demonstrate 0.2 μm resolution [18]. In 1992, the Advanced Lithography Group (ALG), a consortium of universities and industry in the US and Europe, was formed to build a next-generation IPL system. The result was ALG-1000 [19], the goal of which was to project sub-0.18 μ m patterns in a stencil mask onto a wafer substrate. In 1997, MEDEA, another international consortium was founded to build an IPL process development tool (PDT) to achieve 50 nm resolution [15, 16]. Up to now, 50 nm resolution has been demonstrated [20, 21]. Like EPL, IPL also has the difficulty of mask fabrication and space charging effects. In addition, ions can induce damage in the mask and the underlaying substrate.

Nanoimprint lithography (NIL)

In 2003, nanoimprint lithography (NIL) was formally accepted by ITRS as an NGL candidate for the 32 nm node and beyond, and scheduled for industrial manufacturing in 2013 [22]. NIL is a parallel patterning method in which the shape of a rigid mold (usually silicon) is replicated into a resist (usually a polymer) coated on a hard substrate by mechanical contact [7]. Invented in 1995 [23], NIL has attracted a great deal of attention as a low-cost, high-throughput, high-resolution parallel patterning lithography technique. Types of NIL have been developed, but the most important

ones are thermal NIL [23–25] and UV-NIL [26]. The main difference is the resist. In thermal NIL, a thermoplastic polymer resist is heated to above its glass transition temperature, where the solid resist becomes a viscous liquid. Then, it is pressed into the mold. In UV-NIL, first a photo-curable (often UV light) liquid instead of a solid polymer resist is pressed into a UV-transparent mold, then the resist is solidified by UV light exposure at room temperature. Up to now, NIL can fabricate polymer pattern features as small as 5 nm [27] with an aspect ratio up to 40 [28]. NIL is a promising fabrication technique for the community of sensors, lab-on-a-chip, nanooptics, and compact disks which require a cheap method to produce a multitude of identical devices. However, both thermal NIL and UV-NIL are not ready for mass production. They are still time-consuming, either due to the slow heating and cooling or the slow curing and air dissolution processes. Besides the resolution and the speed, many problems are caused by the mechanical nature of the process. Unlike optical lithography, which avoids mechanical contact between the mask and the resist, the 3D mechanical contact is an essential part of NIL. In NIL, high-temperature- and high-pressure-induced mechanical deformations of the mold and the resist can happen during or after the pattern transfer and mold removal. Other concerns are the pattern overlay due to the thermal expansion mismatch, the defects caused by air bubbles, and the patterning of the nanometer-sized mold. Thus, in a long-term view, NIL will be an integral part of nanofabrication, not the replacement of optical lithography.

1.2.3 Beyond next-generation lithography: Maskless and resistless techniques

Some relatively slow approaches that work in a serial process are being pursued for the high resolution required by the 32 nm node and beyond. Besides the advantage of the resolution, these approaches can lower manufacturing costs because they do not need the very expensive masks required by optical lithography. Though excluded from the list of NGLs, these approaches play active roles in research and prototyping individual devices, for instance when making high-resolution masks for optical lithography.

Maskless lithography (ML2)

Electron beam lithography (EBL) and ion beam lithography (IBL)

At energies higher than 2 keV, the wavelengths of both electrons and ions are so short as to be of negligible concern (for instance, 0.01 nm and 2.8×10^{-4} for 10 kV electrons and ions, respectively). Moreover, electron or ion beams can be focused finely in the sub-nanometer regime, giving electron and ion beam lithography (EBL and IBL) advantages in terms of resolution.

EBL emerged in the early 1960s at approximately the same time as optical lithography. An EBL system is very much like a scanning electron microscope (SEM),

which evolved into EBL mainly because of the discovery of an electron-sensitive polymer resist material called polymethylmethacrylate (PMMA). Later, with the improvement of electron beam size, writing strategy, resist material, and development process, the resolution of EBL has been improved over the past four decades. In the early 1970s, EBL was already able to pattern features as small as 60 nm [29]. Today with the special resist material hydrogen silsesquioxane (HSQ), 5 nm features can be written with EBL [30]. However, the best resolution using HSQ has never been below 5-6 nm even with a resist layer as thin as 5 nm and a 100 keV electron beam [31]. It is believed that the key limiting factors are the electron-resist interaction and the resist development, not the accuracy of the width of the electron beam and the procedure for the beam movements. Therefore, the roadblock to further resolution improvement is the nature of the resist materials. So far, at least two commercial EBL systems (JEOL and VISTEC), which are used for prototyping individual devices, have been developed.

In the early days, IBL was hampered because a fine size ion beam was difficult to achieve from the early gas discharge ion sources before the introduction of the focused ion beam (FIB) based on liquid metal ion sources (LMIS) [32–34]. IBL work has been performed based on Ga⁺ FIB, and light ions such as H⁺, He⁺ and Be⁺, as reported in an early overview given by Melngailis [35]. Today, the smallest Ga⁺ FIB spotsize is as small as 5 nm [36]. The main differences between IBL and EBL are caused by the different masses of ions and electrons. Compared to EBL, IBL has the advantages of higher resist exposure sensitivity as a result of the higher efficiency of energy transfer [37], and a lower proximity effect because of negligible ion scattering in the resist and low backscattering from the substrate [38]. The disadvantages of IBL are a lower resolution due to a larger beam diameter and contamination from Ga⁺ FIB exposure. Smallest features including 12.5 nm linewidth in PMMA resist [39] and a 30 nm dot size in polyphenylsilsesquioxane resist [40] have been reported. In 2006, helium ion microscopy (HIM) with a sub-nm probe size became commercially available [41]. Recent work demonstrates that with a HSQ resist, sub-10 nm resolution and a very low proximity effect have been achieved with HIM lithography [42].

In order to improve throughput, several multi-electron beam lithography approaches have been proposed: multiple aperture pixel-by-pixel enhancement of resolution (MAPPER) [43–45] and projection maskless lithography (PML2) [46–48]. Arrays of several hundreds or thousands of individually addressable electron beamlets have been realized by MAPPER and PML2. The space charge effects are supposed to be minimized due to the absence of crossover among the beamlets. The idea is that a single electron source illuminates an array of apertures, forming electron beams that are focused by electrostatic lens arrays on the wafer. Underneath the apertures there are deflector plates, which can blank or unblank electron beams individually. MAPPER Lithography has demonstrated a massively parallel electron-beam lithography (110 beamlets) by writing 45 nm dense patterns (32 nm node) [49]. IMS Nanofabrication has realized a PML2 proof-of-concept tool. In parallel with the development of multi-electron beam lithography, multi-ion beam lithography has also attracted attention: Projection maskless patterning (PMLP). IMS Nanofabrication has also realized a PMLP proof-of-concept tool [50, 51]. A broad ion beam (H⁺, He⁺,

 Ar^+ , Xe^+ , C_{60}^-) is directed to a programmable aperture plate system with thousands of apertures, then ion beams pass the deflector plate underneath. Those undeflected beamlets are focused onto to the wafer with nanometer resolution. With an ion optics of 200x reduction, the PMLP tool has demonstrated 16 nm half-pitch (= half distance between two neighboring lines) resolution. In summary, these multi-beam lithography technologies are still in an early stage of development.

Scanning probe lithography (SPL)

SPL techniques, which feature sub-100 nm resolution, are based on the variety of probe microscopes including scanning tunneling microscopy (STM), atomic force microscopy (AFM), and near-field scanning optical microscopy (NSOM). STM, invented in 1981, was the first SPM [52, 53]. By approaching a sharp conductive tip to a sample surface within the atomic range (< 1 nm) and applying a bias between the tip and the sample, one can observe the tunneling of electrons across the gap. As the tunneling current depends exponentially on the gap distance, STM can achieve sub-angstrom vertical resolution and sub-nanometer lateral resolution with a feedback control of the tunneling current. AFM evolved from STM but with a significant difference: an AFM-tip is mounted on a flexible cantilever, whereas an STM tip is rigidly mounted. Depending on the conditions, AFM operates by measuring forces mechanical contact force, van der Waals forces, capillary forces, magnetic forces, etc. The force causes deflections of the cantilever, which can be detected optically and translated into a surface topography image. Using tunneling electrons for imaging, STM has to be operated in an ultra-high vacuum environment, whereras AFM can be operated in air. STM requires a conductive tip and sample, whereas AFM can work on any material. NSOM uses an optical fiber with a small aperture at the end to emit laser light to form the optical probe and a detector very close to the sample surface ($< \lambda$ the wavelength of the illuminating light). NSOM exceeds far-field resolution limits by exploiting the propagation of near-field optical evanescent waves which is no longer limited by diffraction [54].

The possibilities of SPL were first discovered shortly after the STM was invented. Lines were found on a sample surface scanned with an STM probe, which is a phenomenon called local oxidation [55]. This was the first time sub-100 nm structures were obtained without using photons or charged beams. SPL is cheaper, simpler and much slower compared to conventional lithography. Based on the different mechanisms they use, SPL techniques can be sorted into three groups: material modification, addition and removal [4, 56, 57]. In addition, a special SPL technique is atomic manipulation. If the tip-sample gap in STM is very small, the tip-sample interaction can be great enough to move adsorbed atoms on the sample surface. In 1990, Eigler used a W-tip in STM to manipulate single Xe atoms adsorbed onto Ni (111) surface to form the company logo "IBM" [58] or Fe atoms adsorbed onto Cu (111) to form the Chinese characters "atoms" [59]. This atomic manipulation is the ultimate limit achieved so far with nanofabrication.

Material modification can be realized by resist exposure to field-emitted electrons

or optical probe and electrically induced local oxidation. Resist exposure by STM was first reported in 1988 when a 22-nm-wide and 12-nm-thick Au-Pd line was deposited on Si [60]. Besides PMMA, other polymer resists such as SAL601 have been applied as well [61]. AFM with a metal-coated tip has also been applied to provide a local electron source for PMMA resist exposure, which produced a 35-nm-wide line [62]. With an aperture-less metal tip, 40 nm resolution lithography has been obtained in NSOM [63]. Because the electrons in STM and AFM have very low energy and the evanescent wave in NSOM decays exponentially in the resist, very thin resist layers (<50 nm) are required. Owing to the low energy of electrons and the slow scanning speed (typical scanning speed of STM and AFM is 1 μ m/s), the efficiency of SPL is much lower than in EBL. The field-enhanced oxidation around the tip-sample interface in the presence of oxygen or OH groups was firstly reported using STM [64]. On a Si sample, 23 nm resolution has been achieved using AFM [65]. The direct-patterned oxide can be used as dielectric barrier in various electronic devices, such as single-electron transistors [66] and single-electron memories [67].

Material addition can be realized by field-induced deposition and dip-pen lithography (DPN) [4]. Field-induced deposition is based on the well-known phenomenon of field evaporation: atoms or ions can be pulled out of a material surface under very high electrical field (for instance, 5 V/angstrom). With a bias between the tip and the sample, metal-coated STM or AFM tips can serve as emission sources to transport atoms or nanoparticles from the tip to the sample. Tips made of different materials have been used to deposit different nano-dots on samples, for instance 20 nm Au [68] and 22 nm Pt dots [69]. In the presence of precursor molecules such as organometallic gases, the electrons emitted from STM and AFM tips can induce chemical vapor deposition (CVD) by decomposing the precursor molecules. With this approach, Si dots as small as 3.4 nm have been deposited using SiH₂Cl₂ as precursor [70]. Since the first paper on DPN published in 1999 [71], DPN has attracted a great deal of interest and has become the most popular AFM-based SPL technique [4, 72–74]. With DPN, an "ink"-coated AFM tip is used to pattern a sample surface. Unlike other SPL techniques, which can be considered "destructive", DPN is a direct-write "constructive" tool that allows to pattern many types of ink materials, including organic molecules, polymers, DNA, proteins and metals, with sub-50 nm resolution. For some materials, a resolution as small as 15 nm has been achieved [74]. DPN is a unique tool to pattern biological and soft materials since these materials are usually sensitive to the harsh conditions under exposure to the ultraviolet, electron or ion beams. In addition, unlike "destructive" SPL approaches, which have difficulties with parallelization [74], DPN is particularly suitable for parallel operation because the deposition is much less dependent on the applied force on the tip. Many multi-pen systems have been developed and the number of the pens has increased dramatically. An eight-pen nanoplotter for parallel DPN was reported in 2002 [75]. In 2007, ~55 000 cantilevers were used to pattern 450 million sub-100 nm features in 30 min [74].

Material removal can be achieved by electrochemical etching, field-induced decomposition and mechanical scratching. In the presence of an acid solution of HF, materials such as Si(100) can be etched with a resolution of a few tens of nanometers by scanning STM tips over the sample surface [76, 77]. Material removal can also

occur without the presence of a chemical solution. At a bias pulse, STM and AFM tips can make holes on a sample surface directly, ranging in size from a few to a few tens of nanometers. Unfortunately, the location and the size of the holes are usually unpredictable. Mechanisms ranging from field-induced decomposition [78] to local heating [79] are still controversial. By applying force on AFM tips, mechanical scratches measuring a few tens of nanometers in width and a few nanometers in depth can be left on a sample surface. A groove as narrow as 3 nm and as shallow as 1 nm was achieved by the scratching of AFM tip over a mica substrate [80]. Though this approach is simple, it is limited by the shallow scratch depth, the slow speed, the damage of the tip or the short tip lifetime. Generally speaking, the quality of SPM-etched nanostructures is poor and the mechanism is not yet fully understood. There is still a long way to go to before this application can become suitable for industrial applications.

Resistless techniques

Electron-beam-induced deposition (EBID) and ion-beam-induced deposition (IBID)

EBID and IBID are direct writing techniques that do not need masks and resists. With EBID or IBID, precursor molecules adsorbed on a substrate surface are dissociated by an electron- or ion-beam-induced reaction, respectively. This reaction takes place locally only in the vicinity of the irradiated area of the beam. The non-volatile products of the dissociation are locally deposited on the substrate, whereas the volatile products are pumped out of the vacuum chamber. Depending on the types of the precursor, many different materials can be deposited by EBID and IBID, insulators or conductors. The IBID process is illustrated schematically in Figure 1.1. The EBID process only differs in that it uses an electron beam instead of an ion beam.

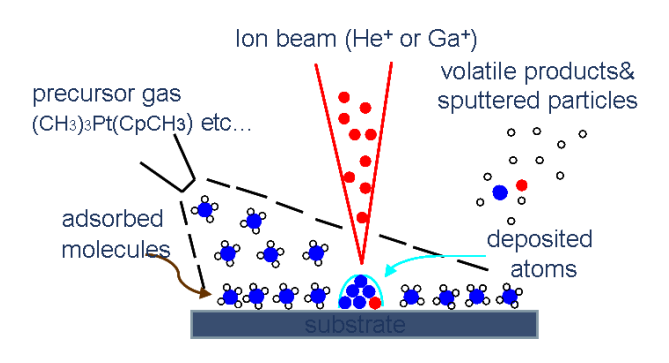


Figure 1.1: Schematic drawing of IBID.

As early as 1934, Stewart observed an insulating film, which was a carbon compound grown in an electrical optical system [81]. At the time, these deposits were

considered as contamination, which was to be avoided. Much research followed to study the contamination induced by electron beam bombardment [82–84]. Until 1960, Christy first recognized the potentially useful feature of this phenomenon by observing that thin (<10 nm) films deposited on a substrate in the presence of silicone oil vapor "had excellent electrical insulation properties" [85]. Actually, in the early days the sources of the precursor were just vapors of diffusion pump oils inside the vacuum chamber. Similarly, the deposits induced by ion beam bombardment were originally also considered to be contamination [86]. In the early stages, IBID was demonstrated only by a wide ion beam until Gamo demonstrated IBID with FIB in 1984 [87]. The deposition yield of IBID was found to be several hundreds of times higher than that of EBID because of the higher dissociation cross sections [86, 88].

Today, most EBID work is performed on the systems such as SEM, TEM and scanning transmission electron microscopy (STEM). Most IBID work is carried out on Ga^+ FIB systems or, only very recently, with helium ion microscope (HIM), which can produce sub-nm He^+ ion beams [89]. As reviewed in [88, 90], the existing precursors allow to deposit most elements by EBID or IBID: C, Al, Si, SiO_x, Au, Cu, Fe, W, Pt, Ge, Co, Cr, Ga, GaAs, Ir, Mn, Mo, Ni, Os, Pb, Pd, Rh, Ru, Sn, and Ti, although purity (low metal content) is a problem, which will be discussed below.

Experimental work related to the ultimate resolution of EBID can be found in [91–101]. Van Dorp demonstrated the best lateral resolution of EBID with 0.72 nm (full width at half maximum FHWM) W dots deposited on a 30-nm-thick Si_3N_4 membrane substrate with a 1-nm-diameter electron beam in an STEM system [91]. The same author declared in a following work that at such a small scale, deposition does not happen exactly locally at the irradiation point, but behaves in a random manner [102]. On a bulk Si substrate in a SEM system, the best lateral resolution achieved was 3.0 nm (FHWM) Pt dots [103]. However, the aspect ratios of these dots are all below unity. The resolution of high-aspect-ratio structures (pillars) is believed to be limited by the generation of secondary electrons along the trajectory of the incident electron beam in the deposit, which can cause a broadening of 5-20 nm according to simulation work [104]. Experimentally, the best resolution of EBID pillars was ~ 50 nm carbon pillars fabricated with phenanthrene ($C_{14}H_{10}$) as precursor [105]. With the same precursor, the minimum diameter of a suspended rod deposited by moving the electron beam laterally was only 5 nm [105]. The different diameters of the pillar and a suspended rod indicate that the interaction volume of primary electrons in the deposits plays a role in the broadening of the high-aspect-ratio structures compared to low-aspect-ratio structures.

Apart from the resolution, the purity of the deposits is another important factor to consider when deciding whether the deposits can be useful. As most precursors used for metal deposition are organic, numerous carbon atoms are also deposited with the metal atoms. Although it varies according to the type of precursor and the electron beam parameters, the metal atomic composition of most EBID deposits is about 10-15% [88, 90, 106]. Fortunately, their purity can be increased significantly (in some case even as high as 95%) by using purification techniques such as heating the substrate during growth, post-annealing after growth, adding a second gas such

as O_2 or H_2 during growth to burn the embedded carbon, or post-annealing in O_2 or H_2 [88, 90, 106].

The resolution of Ga⁺ IBID is generally poorer than that of EBID. The reasons are the larger Ga⁺ FIB diameter (10 nm FHWM) [107] and the more serious depletion of the precursor in the central irradiation area as a result of the higher deposition yield of IBID [88]. The best resolution of IBID pillars was 150 nm Au, which is much larger than the FIB diameter [108]. The metal composition of Ga⁺ IBID deposits is about 35-70%, which is higher than that of EBID 10-15% [88, 90, 106], whereas the metal composition of He⁺ IBID deposits [89] is similar to that of EBID. It is interesting to note that the dissociation mechanism is thought to be a key factor that determines the purity of deposits [88, 109].

In addition, for 3D nanostructure fabrications, IBID nanostructures have advantages over EBID in terms of 3D morphology [110], mechanical behavior [111, 112] and complex 3D structures [113]. Most of these advantages are linked to the shallow penetration of ions compared to that of electrons [110, 113].

1.3 3D nanofabrication by IBID

1.3.1 State-of-the-art and applications

As discussed in the previous section, IBID is considered to be a powerful tool for local prototyping 3D nanostructures [108, 113]. In fact, not only simple 3D structures such as pillars can be fabricated by IBID. With a 3D computer-aided-designed (CAD) software to control the beam scanning in a precise manner (Fig. 1.2a), more complex 3D structures such as branches, coils, beakers, drills, and wine glasses (Fig. 1.2b-f) have been fabricated by IBID [113, 114].

The nanostructures fabricated by IBID have various applications. Examples are mask repair for lithography systems [108], nanoelectrostatic actuators and nano-space-wirings as parts of nanomechanical systems [115], cantilevers as a mass sensor [116], bridge structures as a thermal sensor [117], four-wings rotors [118], electrostatical nano-manipulators [119, 120], electrostatical actuators [120], bio nano-tools such as nano-injectors [121], nano-nets [122], nano-filters [123], nano-sensing probes [124], vacuum microcapsules used as a diode, a triode or a sensor [125], nano-tubes used in nanomechanics and as drug delivery [126], field emitters [127, 128], magnetic dot arrays for data storage [129–132], and nanogap electrodes for single-molecule devices [133, 134]. Despite these listed applications, so far IBID is limited to academic research, due to its serial nature and thus low throughput.

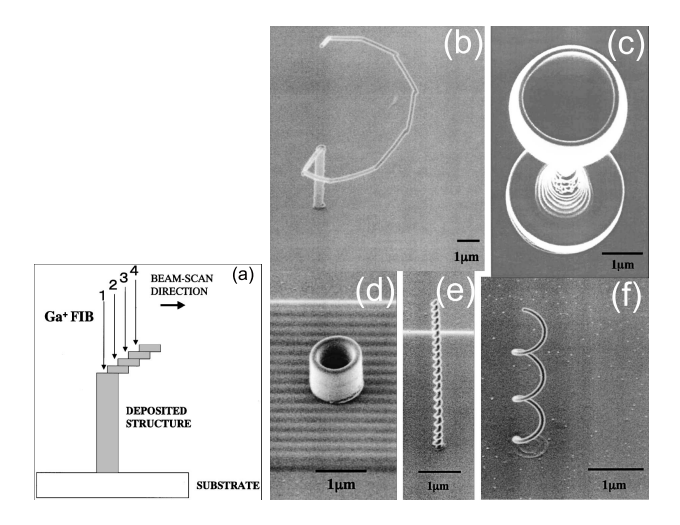


Figure 1.2: 3D nanostructure fabrication by 0.4 pA 30 keV Ga⁺ IBID with phenanthrene (C₁₄H₁₀) as precursor [113]. (a) Fabrication process; (b) branch structure with 80 nm diameter; (c) micro-wine glass measuring 2.75 μ m tall; (d) micro-beakers with 1.0 μ m diameter and 1.0 μ m height; (e) micro-drill with 0.25 μ m diameter, 0.20 μ m pitch and 3.8 μ m height; (f) micro-coil with 0.6 μ m diameter, 0.7 μ m pitch and 80 nm linewidth.

1.3.2 Fundamentals of IBID

Properties of focused ion beams

This section briefly discusses two types of field ionization sources that are applied in modern FIB systems. One is the gas field ionization source (GFIS), which is the central component of He⁺ FIB systems, and the other one is the liquid metal field ionization source (LMIS), which is the central component of Ga⁺ FIB systems. Ga⁺ and He⁺ are the two types of FIB applied in this dissertation. More details of the development of GFIS and LMIS can be found in a book by Orloff [135].

GFIS was invented by Müller in 1951 [136–138] and successfully applied as the surface analytical technique of field ion microscopy (FIM) [139, 140]. In the field ionization process, an atom or molecule (such as H_2 , He, Ne) is trapped by a polarization force near the end of a cryogenically cooled sharp field emitter that is maintained at a very high positive electrical field strength (1 V/angstrom). Then the atom or molecule is ionized by the quantum mechanical tunneling of an electron from this atom or molecule to the field emitter. The material of the field emitter is normally tungsten and the curvature radius of the end is ~50 nm. As we know, the ions have a negligible deBroglie wavelength $(1.4 \times 10^{-4} \text{ nm})$ for 10 keV He⁺ beam), so they follow nearly radial paths from the emitter and appear to originate from a virtual source measuring less than 1 nm in diameter. In the 1970s, applying GFIS to produce a FIB system was reported [141–146]. Because the virtual source size is so small,

the size of the FIB is limited by the aberrations of the beam focusing optics rather than by the source size itself. Therefore, it is convenient to characterize the source in terms of its angular intensity, i.e. by the current emitted per solid angle. For GFIS, the source current density is only $\sim 100 \text{ A/cm}^2$ and the largest typical angular intensity reported is only 1 μ m/sr [147] but the optical brightness is as high as 10⁹ A/cm²sr. These FIB systems based on GFIS can produce beam currents of only ~ 10 pA, which is much lower than the field emission electron source (FES). However, due to this very low current the space charge effects of the ion source caused by the Coulomb interaction between the ions in the beam are almost negligible compared to FES, which is operated at very high intensity ($\geq 0.5 \text{ mA/sr}$). Furthermore, due to the very short wavelength of the ions, diffraction effects are absent for the ion source. The low beam current due to the low angular intensity and the inconvenience of cryogenic operation made GFIS FIB much less popular than Ga⁺ LMIS FIB in the past 30 years, until GFIS recently attracted new interest when helium ion microscope (HIM) with a sub-nm probe size developed at Carl Zeiss SMT (formally the ALIS Corporation) became commercially available in 2006 [41, 148, 149]. The most significant feature of the ALIS helium ion source is its very sharp tungsten tip. The curvature radius of the tip is 50 nm, which is first made by a standard electron-chemical etching procedure. Then by applying a high electrical potential (5 V/angstrom) to the tip, atoms at the most protruding points will be field-evaporated away until the end of the tip can be assumed to have the shape of a three-sided pyramid. With this shape, the electric field is concentrated at the apex of the pyramid, so the field ionization takes place predominantly at the topmost few atoms instead of the hundreds of atoms at the end of the field emitter. The ions from one atom will be selected to travel through the ion optics, yielding a single-atom emitter with high brightness (> 10⁹ A/cm²sr). Conventional FIM and ALIS are compared in Figure 1.3.

Besides field ionization, ions can be directly produced from the atoms of an emitter or a coating film on an emitter at a high electrical potential. This process is known as field evaporation which is responsible for the ion production in LMIS. LMIS FIB was introduced in the late 1970s and early 1980s [32–34]. An LMIS consists of a blunt field emitter (usually tungsten) with an end radius of curvature of $\sim 5~\mu m$. The emitter is connected to a supply reservoir of a metal, which has a low vapor pressure and high surface tension at its melting point. The emitter is heated until the metal becomes liquid, while the emitter is applied with a high positive electrical potential ($\sim 10~\rm kV$) relative to a nearby extraction electrode. When the electrical field is strong enough, the liquid metal is pulled into a conical shape (Taylor cone) by the balance between the electrostatic force and the liquid surface tension [151]. The curvature diameter of this cone is only $\sim 5~\rm nm$ [33, 34, 152]. The TEM image of an operating LMIS in Figure 1.4 shows clearly the formation of the Taylor cone.

Various ion species have been produced by LMIS: Al, As, Au, B, Be, Bi, Cs, Cu, Ga, Ge, Fe, In, Li, Pb, P, Pd, Si, Sn, U and Zn [135]. Ga has become the most popular material for LMIS FIB because it can be operated without heating and remains stable for many hours. As discussed above, the emitting area of LMIS is only 5 nm in diameter, which is much less than hundreds of nanometers as in the case of GFIS. This results in a much higher source current density $\sim 10^6$ A/cm² and

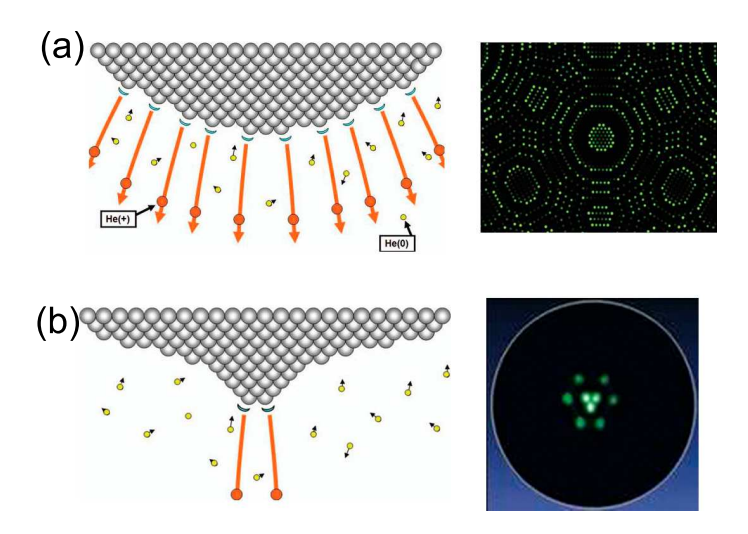


Figure 1.3: Comparison of FIM and the ALIS set-up [41, 150]. (a) Illustration of FIM emitter and the actual FIM image of the geometry. (b) Illustration of ALIS emitter and the actual ALIS image of the geometry.

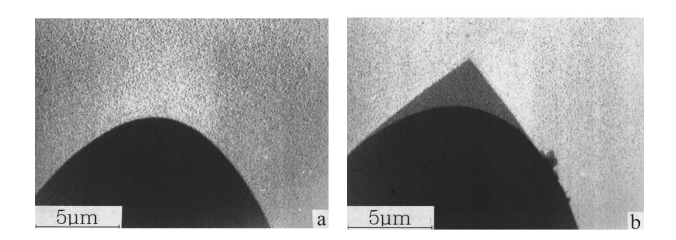


Figure 1.4: TEM image of the shape of the emitter tip coated with a liquid AuGe alloy [152]: (a) without Taylor cone; (b) with Taylor cone.

a higher angular intensity of LMIS of 20 μ m/sr compared to GFIS. Today LMIS FIB can provide a beam current of 1 pA to 30 nA. However, LMIS is limited by the more serious space charge effect because of the larger current density. Though the emission is from 10 nm in diameter, the emission appears to originate from a virtual source of 50-100 nm [135, 153, 154]. Owing to the larger virtual source size, the brightness of LMIS is only 10^6 A/cm²sr, which is less than that of GFIS. The Coulomb repulsion of the ions can also cause the beam to get larger, which is called radial broadening. Experiments and simulations show that a 10 nm beam can be broadened to 70 nm, even to hundreds of nanometers [88, 135, 153, 155–157]. Gaussian distribution cannot precisely describe the beam profile, and a Holtsmark distribution has been proposed to fit the beam profile, as can be seen in Figure 1.5. Clearly, this long tail in the beam distribution can affect the resolution of imaging, implantation and nanofabrication performed by LMIS FIB.

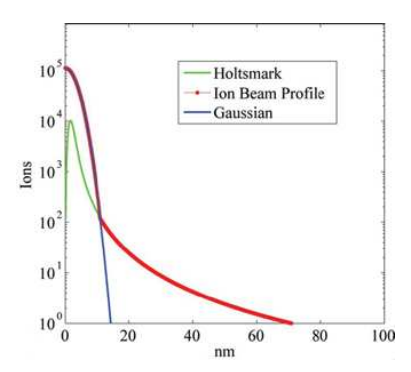


Figure 1.5: Simulated Gaussian-Holtsmark distribution of 30 keV Ga⁺ beam at 1 pA [88].

Supply of the precursor

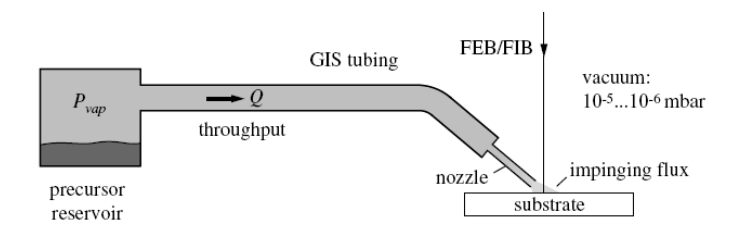


Figure 1.6: Schematic of a nozzle-based GIS for IBID or EBID [158].

Clearly, injection of the precursor into the vacuum chamber and the flux distribution of the precursor molecules on the substrate surface, especially in the irradiated area are important aspects in IBID. A nozzle-based gas injection system (GIS), normally a straight cylindrical tube, is used to deliver the precursor into the chamber for most IBID and EBID systems. In practice, to provide high local precursor flux in the irradiated area while keeping a low total pressure in the entire chamber, the nozzle is brought very close to the substrate surface with a typical distance of about $100~\mu m$ to 1~mm. This setting allows the substrate to move freely below the nozzle.

According to the kinetic gas theory, the mean free path (λ) of the precursor molecule can be calculated by

$$\lambda = \frac{kT}{\sqrt{2\pi\delta^2 P}}\tag{1.1}$$

where k is the Boltzmann constant, T is the absolute temperature of the precursor gas, δ is the molecule diameter, and P is the pressure. In our system the local pressure at the outlet of the nozzle is in the range of 10^{-2} - 10^{-3} mbar. According to the kinetic gas theory, the corresponding MFP of the precursor molecules at room temperature is roughly 1-10 mm, which is much larger than the distance from the nozzle to the irradiated point. Therefore, most molecules do not encounter a gas phase collision before impinging onto the surface. This can explain the observed shading and the proximity effects that I will discuss in Chapter 3.

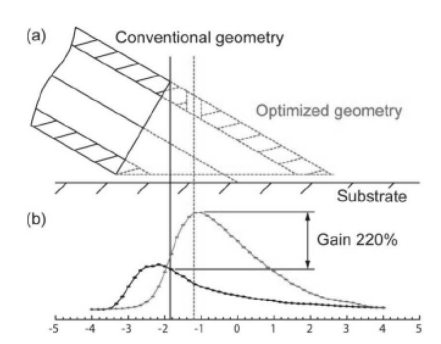


Figure 1.7: Simulated molecule flux impinging on the substrate for a conventional and an optimized tube by a Monte Carlo-based GIS simulator program [88, 158]. The vertical line shows the impinging direction of the electron beam; there is a hole in the optimized tube. (a) Cross section of tube geometries along the tube axis. (b) Molecule flux distribution taken along the tube axis. The x-axis is in units of the inner tube radius.

Though the spatial distribution of the precursor molecule on the substrate surface is crucial for IBID (and EBID), only a few quantitative studies have been published and a Monte Carlo-based GIS simulator program was developed by Fredili [88, 158]. This program considers the molecular and transient flow which can be applied for most IBID (and EBID) systems in reality. A molecular flow regime refers to the situation that no molecule collisions happen when λ is larger than the diameter of the

nozzle tube d, or in other words, when the Knudsen number is $\lambda/d>1$. A transient flow regime refers to $0.1<\lambda/d<1$. For known geometric parameters of the GIS system setup, the spatial distribution can be calculated by this GIS simulator program. This work of Fredili bears several interesting conclusions [88, 158]. Firstly, the experimental deposition shape agrees very well with the simulated precursor spatial distribution. It also indicates that most IBID (and EBID) are in the molecule-supply-limited regime. Secondly, the spatial distribution within an area as small as 100×100 $\mu\mathrm{m}^2$ cannot be considered constant (Fig. 1.7). This is one of the factors that hinder the reproducibility of IBID. Thirdly, two new types of nozzle have been proposed to enhance the efficiency of delivering the precursor molecules to the irradiated area (Fig. 1.7).

Ion-substrate interaction

When an energetic ion penetrates into a solid material, there are two basic classes of interaction processes that slow down the ion and dissipate its energy: (1) nuclear energy losses and (2) electronic energy losses. Nuclear and electronic energy losses result from the elastic collision cascade between the ion and the target atoms within the solid, and from the inelastic scattering between the ion and the lattice electrons, respectively. The dominant energy loss mechanism depends on the energy of the ion and the masses of the ion and the target atom. Roughly speaking, the nuclear energy losses dominate for ions with medium energy and the electronic energy losses take over for ions with high energy. For most Ga⁺ FIB applications, nuclear energy losses dominate [135, 159, 160], whereas electronic energy losses dominate for He⁺ applications [160, 161]. Nuclear losses displace the atoms (usually lattice atoms) in the solid and cause damage and surface sputtering. Electronic energy losses result in the emission of secondary electrons, X rays, photons and phonons.

Figure 1.8 shows a schematic diagram illustrating the sputtering and the secondary electron emission and several parameters used to quantify three-dimensional (3D) spatial distribution of the ion traveling in the target material: the distance from the final position of the ion along the parallel direction to the target surface is the projected range R_p , the transverse projected range is the transverse straggling distance R_t . I will not cover all of these emissions here, but discuss only sputtering and secondary electron emission, which are most probably related to the IBID process. The interested reader can find more details on ion-solid interaction in the extensive review papers or books on this subject [135, 159, 162–167].

Sputtering occurs when a surface atom receives sufficient energy transferred from the primary ion by the collision cascade to overcome the surface binding energy, which is the potential energy between a surface atom and the rest and has a typical value of a few eV. In this case, the surface atom will be removed from the target surface. The energy of the sputtered atoms is typically a few eV. A small portion (<1%) of these sputtered atoms will be ionized and become secondary ions, which can be used for imaging or can be collected and mass separated as a surface analytic technique known as secondary ion mass spectrometry (SIMS) [162]. The sputtering

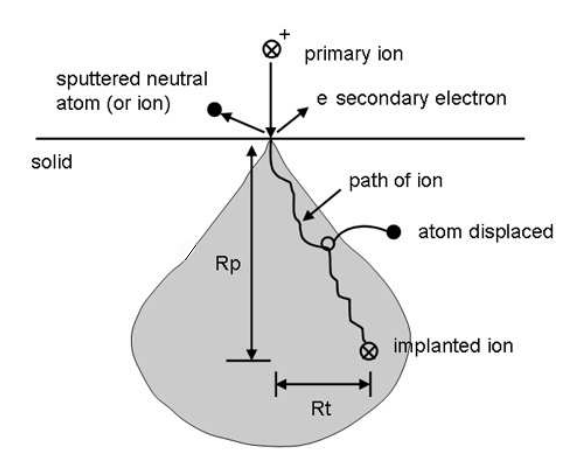


Figure 1.8: Schematic of the ion-solid interaction showing the geometric relationship between the projected range R_p and the transverse straggling distance R_t . The shading area indicates the interaction volume of ion in the solid.

yield depends on the energy and angle of the primary ion, the masses of the ion and the target atom [135, 159, 162–168]. The sputtering yield, defined as the number of sputtered atoms per primary ion, has a typical value for Ga⁺ FIB between 0.1-100 while for He⁺ it is several hundreds of times less. The linear collision cascade model gives this quantitative dependence of the sputtering yield [169]. Since sputtering is a surface phenomenon, the sputtering yield increases if the collision cascade happens closer to the surface. Within the typical energy range of modern FIB (5-30 keV), the sputtering yield increases with increasing energy. This increase slows down until it reaches a stable level because the projected range becomes larger and the collision cascade is located deeper, which makes it more difficult for the atoms to escape from the surface. The angular dependence of the sputtering yield follows $1/\cos(\theta)^f$, where θ is the ion incident angle which is defined as the angle between the surface normal and the ion incident direction, f is a constant typically between 1 to 2 which is determined mainly by the mass ratio of the ion and the target material. The sputtering yield reaches a maximum at $\theta = 75^{\circ}-85^{\circ}$, then decreases rapidly because of the high reflection of the primary ion. In practice, however, it is still difficult to calculate the sputtering yield with these models. For this reason, a Monte Carlo computer simulation program called SRIM (stopping and range of ions in matter) and its subroutine TRIM (transport ions in matter) are very useful for quantitatively estimating the sputtering yield and 3D spatial distribution of the ion in the target material [160, 163].

Ion-induced secondary electron emission has been studied for many years. Extensive review papers on ion-induced secondary electron emissions have been published in [170–172]. Similar to sputtering, emission of secondary electrons is also a result of a scattering and energy-loss (inelastic) process. Electrons are excited through the collision cascade generated by the incident ion in the target material. These excited electrons continue to undergo collisions in the solid until most energy is lost as heat.

The average length (mean free path) between two collisions depends on the energy of the electrons. Some of these excited electrons are directed outwards and hence are able to reach the surface and escape. These escaped electrons (secondary electrons) typically have low energy (< 50 eV). As secondary electrons originate mostly from layers a few nanometers below the surface, the emission is very sensitive to the surface condition. Generally speaking, the electrons escape more easily from insulators than from metals or semiconductors, which can be attributed to the larger mean free path due to less electron scattering in insulators. However, the emission of secondary electrons from insulators is very complicated due to surface charging. The secondary electron yield, defined as the number of secondary electrons per primary ion, has a typical value of 0.1-10. The energy and angular dependence of the secondary electron yield is similar to the case of the sputtering yield [171, 173–179]. Moreover, the energy spectrum of the secondary electrons shifts slightly to higher energies with increasing ion energy [171, 180].

Precursor molecule-substrate interaction

Precursor molecules can be adsorbed on a substrate surface either physically or chemically. The adsorbed precursor molecules can then diffuse on the substrate surface. Chemical adsorption, which is strong and non-reversible, occurs due to the formation of a chemical bond between the molecule and the surface, whereas physical adsorption, which is weak and reversible, occurs due to a dipole-induced interaction. Here, I will only discuss physical adsorption, which is the situation applied to IBID, and discuss the diffusion later. As stated above, physical adsorption is reversible, which means that, on average, the adsorbed molecules desorb from the substrate surface after a residence time τ . The value of τ depends on the substrate temperature T as $\tau(T) = \frac{1}{\nu} \exp(E_{des}/kT)$, where ν is the vibrational frequency of a molecule adsorbed on the surface having a typical value between 10^{12} to 10^{13} s⁻¹, E_{des} is the desorption energy having a typical value of 0.1-0.5 eV [88, 181]. Correspondingly, the typical values of τ at room temperature are between 10^{-8} and 10^{-3} s, respectively. When a dynamic equilibrium between adsorption and desorption has been reached, a precursor monolayer with a constant density forms on the substrate surface. Multilayer adsorption (condensation) occurs only on a very cold substrate surface.

Diffusion can be considered as a random movement. For instance, for a large irradiated area, the contribution of diffusion to dissociation can be neglected because the displacement of the molecules occurs only from one irradiated spot to another inside the irradiated area. However, for a small irradiated area, diffusion plays a significant role in supplying the molecules [88, 182]. In that case, the dissociation of the precursor is so fast that a concentration gradient develops, causing diffusion of the neighboring adsorbates into the irradiation area (Fig. 1.9). Surface diffusion coefficient D depends on the substrate temperature T as $D(T)=D_0 \exp(-E_{diff}/kT)$, where E_{diff} is the activation energy for diffusion.

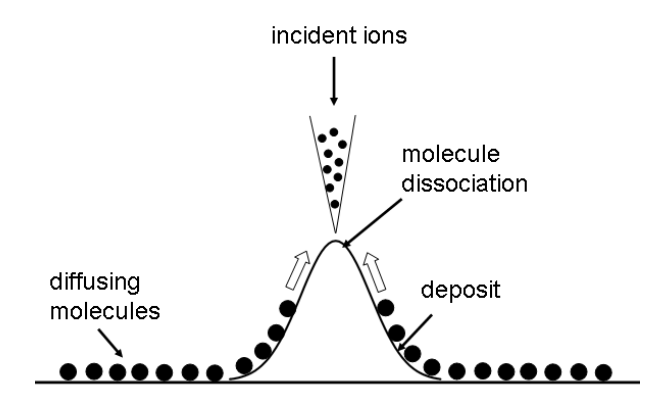


Figure 1.9: Schematic of the contribution of diffusion to the supply of molecules in IBID.

Ion-precursor molecule interaction

The incident ion can have several effects on the adsorbed precursor molecules on the substrate surface: desorption of the molecules, dissociation of the molecules, or stimulated chemical interaction between the molecules and the substrate. Here I will discuss only the dissociation of the molecules because it is the basis for IBID (and ion-beam-induced etching).

The total deposition rate of IBID R(r) [nm/s] can be expressed by [88, 183]

$$R(r) = Vn(r)\sigma f(r) \tag{1.2}$$

where V [nm³] is the volume of the decomposed molecule, n(r) [nm⁻²] is the number of adsorbed molecules per surface unit, σ [nm²] is the dissociation cross section, and f(r) [nm⁻² s⁻¹] describes the ion flux distribution. The probability for an ion to break the chemical bond of a molecule is the product of n(r) and σ . Knowledge of σ is crucial to understand the IBID mechanism, and to maintain full control over the resolution, the throughput and the purity of the deposits. However, σ is very difficult to determine because it depends on many parameters: the energy of the incident primary ions and the generated secondaries, the bonding of the molecule, and the property of the substrate, etc. Relevant studies of the dissociation cross section in IBID are rare and not yet fully developed, which is partly due to the different interpretations of the IBID mechanism. One group of authors believes that the energy transfer via a cascade of atom-atom collisions to the adsorbed molecules is responsible for the dissociation because they found that the experimental deposition yield is proportional to the theoretically calculated nuclear stopping power [184–186]. The second group of authors observed a linear relationship between the deposition yield and the secondary electron yield, therefore they support a secondary electron model [187]. Furthermore, it is even still unclear whether it is fair to rule out the role of the primary ion in IBID [188].

The model of Dubner describes the dissociation in terms of the kinetic energy transfer during the collision cascade from an excited surface atom to the atoms of the molecule [185]. Although good agreement between experimental and the theoretically calculated deposition yield was found, the weak point of this model is the over-simplification of the energy transfer process [88]. Some available data of the IBID deposition cross sections: $\sigma = 10 \text{ nm}^2 \text{ (W(CO)}_6, \text{ with } 42 \text{ keV Ga}^+\text{)} [189]$ and $\sigma = 52 \text{ nm}^2 \text{ (DMG (hfac), with } 40 \text{ keV Ga}^+\text{)} [190], were estimated by combining the experimental IBID deposition yield and assuming a Gaussian FIB distribution.$

As discussed above, ion-induced secondary electrons can also contribute to the dissociation [187]. Therefore, I will also briefly discuss several studies of the electron interaction with molecules, though they were aimed at studying the dissociation in EBID, not IBID. Owing to the difficulty of theoretically calculating the dissociation cross section, the deposition cross section was measured instead. The deposition cross sections were found to have a peak at around 100-200 eV for $W(CO)_6$ [191], SiO_x [191] and (CH₃)₃Pt(C_pCH₃) [192, 193] adsorbed on a substrate surface. In addition, a similarity between the W(CO)₆ deposition cross section and the secondary electron yield indicates that the low-energy electrons are responsible for the deposition [191]. Actually, energies as low as a few eV are sufficient to break the chemical bond in the molecule. For instance, a threshold energy of 4 eV was observed for Cu(I)(hfac)(vtms) molecules [194]. Despite the importance of the low-energy electrons, in practice it is extremely difficult to control a low-energy electron beam below 20 eV to perform reliable experiments. With $(CH_3)_3Pt(C_pCH_3)$, by varying the energy of the electron beam Botman et al. found that the deposition cross section has a peak at 140 eV [192]. With the same precursor, van Dorp et al. performed thermal programmed desorption experiments, in which a cooled substrate with adsorbed molecules was irradiated with a broad low-energy electron beam. A peak value of 140 eV was confirmed [193]. However, the same basic barrier occurred for both cases: the control of an electron beam below 20 eV [192, 193]. In addition, it is worth pointing out that secondary electrons can be generated by an electron beam above 100 eV. Therefore, unless a good low-energy electron beam can be obtained, one cannot distinguish the contributions of secondary electrons from those of primary electrons.

Regarding all the previous work, the dissociation cross section of the adsorbed molecules irradiated with ions in IBID is not yet fully understood. Furthermore, the ion-substrate and precursor-substrate interactions discussed in previous sections are still not yet fully understood. These factors make that the understanding of IBID mechanisms remains a complicated issue.

1.4 Outline of this dissertation

This dissertation reports on the fabrication of 3D nanostructures by using a direct writing technology IBID, and the investigation of IBID mechanisms. The outline of this dissertation is as follows.

Chapter 3 reports the exploration of the limits of IBID to fabricate nanopillars using a conventional Ga⁺ FIB and a novel He⁺ FIB. By varying the growth conditions, we investigated the influences of precursor surface density and the ion beam on pillar growth. To improve the quality of IBID pillars, we studied the formations of the irregular sidewall surface and the halo on the substrate of typical Ga⁺ IBID pillars. We also studied the proximity effects in Ga⁺ and He⁺ IBID pillar growth.

Chapter 4 describes a novel fabrication method for nanopores by IBID. We demonstrated that sub-10-nm-diameter nanopores in a $\mathrm{Si_3N_4}$ membrane can be fabricated by a single IBID step. This is accomplished by exploiting the competition between sputtering and deposition during IBID. We studied the chemical composition and the shape of the pore at various stages of pore formation using 3D electron tomography, energy dispersive x-ray (EDX) and electron energy loss spectroscopy (EELS) analysis. We also applied SRIM simulations to show how forward and backward sputtering depend on the membrane thickness.

Chapter 5 reports a series of experiments to distinguish the roles of different mechanisms involved in the IBID process. We observed a significant contribution of secondary particles to Ga⁺ IBID. We discussed two models which describe IBID mechanisms in terms of the impact of secondary electrons and of sputtered atoms, respectively. We also investigated the contribution of primary ions. Finally, we review studies on IBID mechanisms with Ga⁺ or He⁺ and on EBID mechanisms published in the open literature.

Finally, **Chapter 6** presents the conclusions.

Ouestion

Chapter 1: Introduction

•Why and how do we study the limits of IBID to prototype 3D nano-structures? •What are the limits?

Experimental

Chapter 2: Set-ups and methods

- Dual beam system
- He+ microscopy
- home-made accessories

Research

engineering study

Chapter 3: Nano-pillar growth by IBID

- Study the influences of some important factors on the vertical growth rate and the resolution.
- Study the formation of the roughness on the pillar sidewall and the surrounding halo at the base
- · Study the proximity effect

Chapter 4: Nano-pore fabrication by IBID

- Demonstrate a fast single-step method for nano-pore fabrication
- Characterize IBID nano-pores

fundamental study

Chapter 5: IBID mechanisms

- Study deposition outside the irradiated area induced by secondary particles
- Distinguish roles of secondary electrons and secondary atoms in IBID
- Study deposits in spot mode induced by primary ions

Answer

Chapter 6: Conclusions and Outlook

- Resolutions of IBID nano-pillar and nano-pore are limited by the interplay between the vertical and lateral growth and the competion between deposition and sputtering.
- Probably the IBID process cannot be explained by a sole mechanism. The contribution of secondary atoms dominate in Ga⁺ IBID while the contribution of secondary electrons dominate in He⁺ IBID.
- The future of IBID relies on the exploration of applications.

Figure 1.10: Outline of this dissertation

Chapter 2

Setups and methods

2.1 Abstract

This chapter describes the technical details of two commercial systems, namely the FIB-SEM DualBeam microscope, and the helium ion microscope and accessories which are used for tuning substrate bias and temperature.

2.2 FIB-SEM DualBeam system: FEI STRATA 235

The IBID experiments were performed mainly on a combined FIB plus SEM DualBeam system FEI Strata DB 235 installed in Nanofacility group, Nanoscience Department, TU Delft (Fig. 2.1). The FEI company is a leading supplier of charged particle beam systems, including FIB systems, DualBeam systems, scanning and transmission electron microscopes, and components. The FEI Strata DB 235 features FEI's high performance $Magnum^{TM}$ ion column as standard equipment. The SEM is a high-performance field-emission microscope, whereas the ion-beam system has a gallium liquid-metal ion source (LMIS) that yields a high-brightness Ga⁺ beam. In a Ga LMIS, liquid gallium metal is placed in contact with a tungsten needle and heated. Gallium wets the tungsten, and a huge electric field causes ionization and field emission of the gallium atoms. Source ions are then accelerated to an energy of 5-50 keV, and focused by electrostatic lenses. LMIS produce high-current-density ion beams with very little energy spread. A modern FIB can deliver tens of nanoamperes of current to a sample, or it can image the sample with a spot size on the order of a few nanometers. Strata DB 235 is the industry's first full-featured versatile Dual-Beam system with a wide variety of functionality for nanofabrication and additional materials characterization capability. A nano-manipulator is installed in our system for in-situ TEM sample preparation. Strata DB 235 offers energy dispersive X-ray spectroscopy (EDX) capability. EDX provides elemental site-specific information of samples operated in spot, line-scan or Z-contrast map mode. Therefore, this tool is ideally suited to failure analysis and cross sectioning of samples. There is also a gas injection system (GIS), which allows reactive ion etching or the deposition of metals such as platinum. $(CH_3)_3Pt(C_PCH_3)$ was used as the Pt precursor. The GIS bottle is connected to a nozzle of 400 μ m in diameter which is located 450 μ m above the substrate surface at an angle of 34° to the normal of the surface (Fig. 3.1 in Chapter 3).

During IBID work, samples were put on a fully motorized stage and mounted with carbon glue onto an aluminum sample holder measuring 3 cm in diameter. The range of acceleration voltage of the $\mathrm{Ga^+}$ was 5 to 30 kV and the currents were from 1 pA upto 20 nA. A picoampere-meter connected to the sample stage was used to measure the ion-beam current absorbed in a Faraday cup and the sample current. The full width half maximum (FWHM) of the Gaussian beam profile of 1 pA is about 10 nm. The beam movement was controlled by a script that enables the writing of complex patterns and provides the exposure dwell time ($\geq 0.1~\mu\mathrm{s}$), the step size of the beam, and the number of dots.

2.3 Helium Ion Microscopy: Carl Zeiss Orion TM plus SHIM

In 2006, helium ion microscopy (HIM) with a subnanometer probe size became commercially available [41, 148]. The ion source developed at Carl Zeiss SMT (formerly

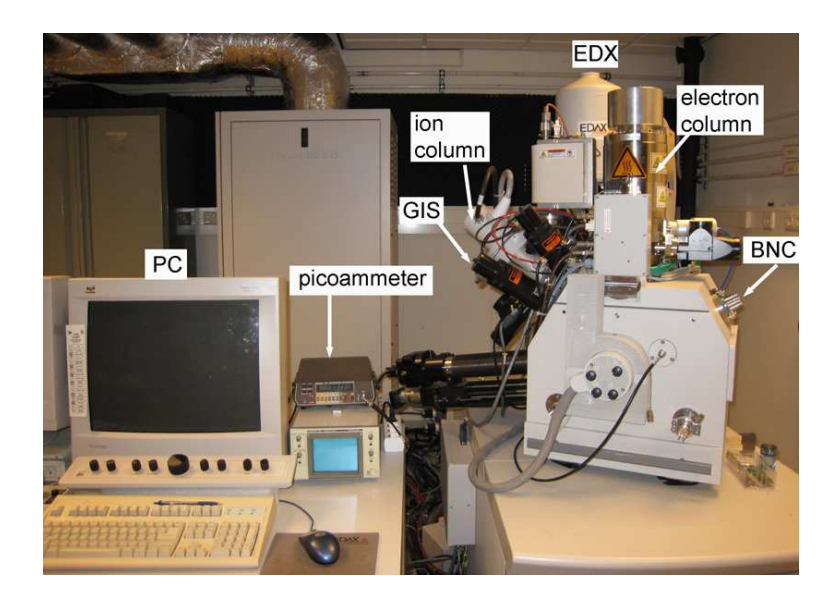


Figure 2.1: Photo of the FEI Strata DB 235 system installed at Delft University of Technology.

the ALIS Corporation) is introduced by comparison with the related technology known as field ion microscopy (FIM), which was developed over 50 years ago and provided the first direct observation of the arrangement of atoms in matter. FIM has a cryogenically cooled metal tip (100 nm in diameter). When the tip is positively biased, the nearby neutral gas atoms will be ionized by electron tunneling. Then these positive ions will be accelerated away from the tip. The ALIS helium ion source is built upon FIM technology. The most significant feature of the ALIS helium ion source is its very sharp tungsten tip, which is manipulated until it assumes the shape of a three-sided pyramid. With this shape, the electric field is concentrated at the apex of the pyramid, so field ionization takes place predominantly at the topmost few atoms. One of the first HIM systems in the world was installed by the NanoNed consortium and located at an independent research organization in the Nederlands, namely TNO Science and Industry. The HIM experiments presented in this thesis were performed on the HIM system installed at TNO. The acceleration voltage of He⁺ ranged from 5 to 30 kV. The beam currents of HIM range from 1 fA upto 100 pA and the typical working current is 1-5 pA. The beam movement was controlled by a pattern-generation system, which enables the writing of complex patterns and provides exposure dwell time and beam step size. HIM affords the highest resolution surface imaging of bulk materials with a scanning manner, and bridges the gap in imaging resolution traditionally left between SEM and TEM. HIM has a wide field of view, enhanced depth of focus, and excellent surface sensitivity. Owing to its small probe size, the small interaction volume in the substrate, the physics of secondary electron generation and the Rutherford backscattered ions HIM has advantages over SEM. However, HIM has some drawbacks as well. For instance, the available beam currents of HIM are rather low compared to SEM. Furthermore, sample damage can

be induced by sputtering in HIM. Overall, there is still a long way to go before HIM becomes as widespread as SEM.

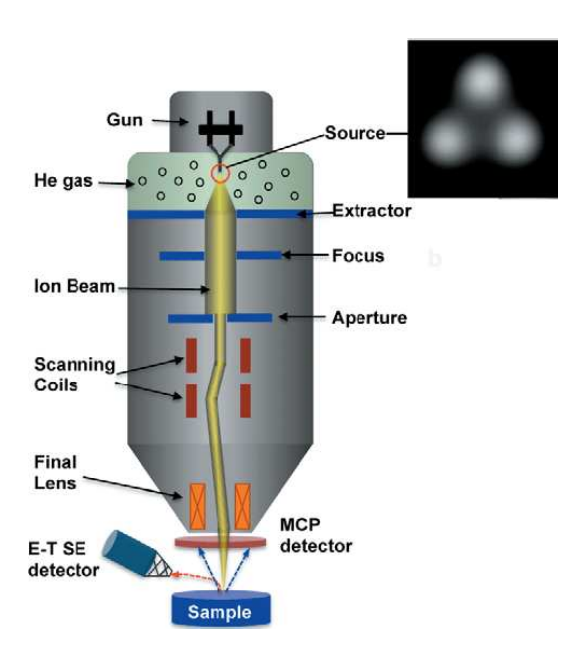


Figure 2.2: Schematic of the Orion-type HIM column that indicates the ion source, apertures, and detectors configuration. Inset image of atomic trimer on tungsten showing He⁺ emission from three atoms; one atom is selected by means of aperture placement to produce the beam [195].

2.4 Additional accessories for tuning the substrate bias and temperature

Through a flange on the side door of the chamber, a power supply connected to a conductive copper wire inside the vacuum chamber was used to adjust the bias on the substrate surface. The sample was mounted on a chip carrier. A cascade of Peltier elements with an aluminum heat absorber mounted on the stage was used to control the substrate temperature between -20 and 90 °C. The temperature was measured with a chromel-alumel thermocouple (Fig. 3.3).

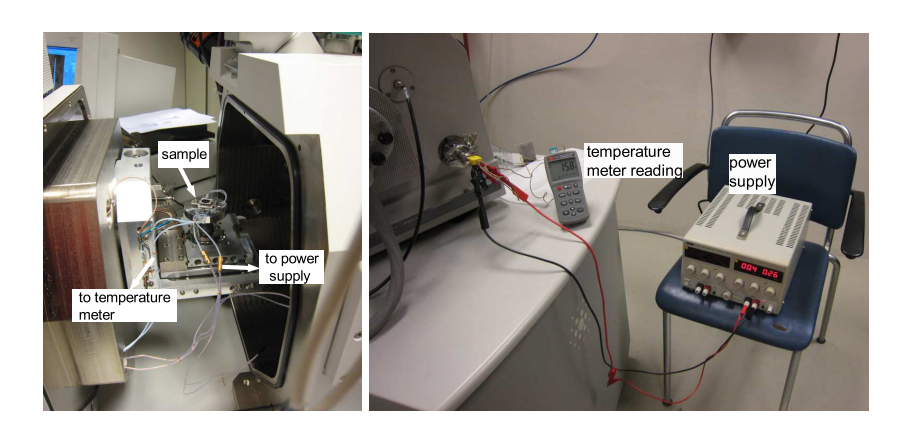


Figure 2.3: Photo of the substrate temperature tuning accessory installed in the Strata DB 235 system.

Chapter 3

Nanopillar growth by IBID

3.1 Abstract

A nanopillar can be regarded as a simple example of a three-dimensional (3D) nanostructure. Nanofabrication aims to fabricate nanopillars with nanometer precision in height and width. As this dissertation deals with nanometer-scale ion-based fabrication, nanopillar growth by ion-beam-induced deposition (IBID) was selected as a main research topic. This chapter discusses the relevant parameters and processes of IBID pillar growth.

Section 3.2 introduces the research topics and explains the key parameters such as halos etc. Section 3.3 gives the experimental procedure for the experiments described in Sections 3.4-3.6.

Section 3.4 summarizes the growth conditions required to fabricate nanopillars in a controllable and reproducible manner. Two types of ion techniques were used: (1) conventional Ga⁺ beam, which has a typical beam diameter of 10 nm, and (2) novel He⁺ beam, which has a typical beam diameter in the sub-nanometer regime. With the conventional Ga⁺ beam, the influence of precursor surface density on pillar growth was investigated by changing the deposition site on the substrate with respect to the nozzle, the substrate temperature, and the ion beam dwell time or refreshment time. With the novel He⁺ beam, the influence of the ion beam was investigated by changing the current of the ion beam. Based on these results, Ga⁺ and He⁺ IBID pillar growth is compared. Furthermore, a model is presented to explain the interplay between vertical and lateral growth during IBID pillar growth.

The work presented in this chapter has been published as (1) P. F. A. Alkemade, P. Chen, E. van Veldhoven, and Diederik Maas, Analytical Model for Nanopillar Growth by Focused Helium Ion-Beam-Induced Deposition, submitted to *J. Vac. Sci. Technol. B* (2010). (2) P. Chen, H. W. M. Salemink, and P. F. A. Alkemade, *J. Vac. Sci. Technol. B* 27, 1838 (2009). (3) P. Chen, H. W. M. Salemink, and P. F. A. Alkemade, *Jpn. J. Appl. Phys.* 47, 8120 (2008).

Section 3.5 presents the formations of the irregular sidewall surface and the halo on the substrate of a typical Ga⁺ IBID pillar. The influence of substrate (surface) conductivity is studied by comparing pillars grown on different substrates, either on a conducting bulk Si or an insulating Si₃N₄ membrane. It shows that the pillars grown on an insulating-surface are higher and thinner than those grown on a conducting surface although they have the same volume. The insulating-grown pillars are smoother with smaller halos. These differences suggest a charging effect of nanopillar growth, which can be attributed to the secondary electron emission and possibly to the aggregation of precursor gas molecules during IBID.

Section 3.6 discusses the proximity effect of pillar growth, which should be avoided for the fabrication of dense pillar arrays by IBID. The proximity effect is caused by the scattering of incident ions and secondary particles, the non-homogeneous precursor coverage, and the conductivity of the substrate. We studied the proximity effect in terms of these three factors with a Ga⁺ beam. With a He⁺ beam, though the proximity effect of pillars grown on the conducting bulk Si is weaker than that with the Ga⁺ beam, the proximity effect can be explained by the same mechanisms.

In the conclusion, the different factors influencing IBID pillar growth will be described, as well as their interplay. This interrelation is important to fabricate pillar (arrays) as an engineering technology with maximum flexibility.

3.2 Introduction

In the direct writing technology, IBID, precursor molecules adsorbed on a substrate surface are decomposed by an ion-beam-induced reaction, resulting in localized material deposition. Owing to its high flexibility with respect to the shape and location of the deposits, IBID is becoming increasingly interesting as a powerful tool for prototyping 3D nanostructures for various applications [108, 113]. A pillar can be regarded as a simple example of a 3D nanostructure. This chapter discusses several topics related to IBID pillar growth: process dependences of the pillar width and height; formation of the rough sidewall and the halos; and the proximity effect. Relevant studies of these three topics will be introduced below.

3.2.1 Process dependences of IBID pillar growth

Though IBID has an advantage over EBID with regards to growth rate, an even higher growth rate is still desirable. The growth rate of IBID (also of EBID) is proportional to the surface density of the precursor molecules, which depends on adsorption, diffusion, desorption and decomposition of the precursor molecules on the substrate surface [88]. These are (some of) the parameters we look for. A relationship among (all) key parameters involved is given in Equation 3.1, which will be discussed in detail in Section 3.4.4. The growth rate can be enhanced by changing the parameters that can influence the balance of precursor molecule depletion (desorption and decomposition) and replenishment (adsorption and diffusion) within the deposition region, such as increasing the precursor pressure [97, 196–199], decreasing the substrate temperature [90, 181, 198, 200-202], decreasing the beam dwell time or increasing the precursor refreshment time [203–205], or defocusing the beam [204]. However, these studies mostly discuss the growth of a box or a dot, not a high-aspect-ratio structure like a pillar. Simulation works show that both the growth rate and the resolution of EBID pillars can be enhanced by increasing the precursor surface density within the deposition region [88, 182, 183, 206–208]. Experiments of increasing the precursor pressure during EBID demonstrated that both the growth rate and the resolution of pillars are enhanced [196]. However, the effects of precursor surface density on the growth rate and the resolution of IBID pillars have not yet been thoroughly discussed in literature. In this chapter, we investigate this aspect by changing the deposition site on the substrate with respect to the nozzle, the substrate temperature, the ion beam dwell time, and the precursor refreshment time.

So far, most IBID work has been performed with Ga⁺ FIB, which typically has a beam size of 10 nm. Only a few studies deal with broad (~mm) ion beams, such as H⁺, He⁺, Li⁺, Ne⁺, and Xe⁺ [86, 185, 186]. Despite of the different conditions applied, Ga⁺ IBID pillars are always more than 100 nm in diameter [108, 112, 128, 209]. The pillar broadening is attributed to the scattering of primary ions and secondary particles [105, 206, 210, 211]. In addition, Ga⁺ IBID pillars always have rough sidewalls and relatively flat tops [209]. Recently, helium ion microscopy (HIM) with a sub-nanometer probe size became commercially available [41, 148]. Owing to its small probe size, the small interaction volume in the substrate close to the surface, the

physics of secondary electron generation and the Rutherford backscattered ions, HIM has advantages over scanning electron microscopy (SEM) [41, 149, 150, 195, 212, 213]. In addition, HIM is becoming increasingly interesting as a tool for nanofabrication. A very recent work demonstrates that a higher resolution and a lower proximity effect can be achieved with He⁺ lithography than with electron beam lithography (EBL) and Ga⁺ FIB lithography [214]. For He⁺ IBID, due to the smaller probe size and the nature of noble ions, a better resolution and less contamination than with Ga⁺ IBID are expected. Sanford et al. reported that with a (CH₃)₃Pt(C_PCH₃) precursor, the deposition yield of He⁺ IBID is similar to that of Ga⁺ IBID, whereas the Pt atomic composition of the deposits is similar to that of EBID but lower than that of Ga⁺ IBID [89]. Here, we report the first successful growth of pillars by He⁺ IBID and the dependence of pillar growth on He⁺ beam current.

3.2.2 Formation of rough sidewalls and halos by Ga⁺ IBID

Though IBID and EBID are powerful for prototyping nanopillars, we note that IBID and EBID pillars are not always as regular as intended. For instance, they frequently exhibit irregular extensions on their sidewalls and micrometer-sized halos, viz., the deposits around their bases. Generally, IBID pillars are less smooth than EBID pillars, although EBID pillars also become rough when a high electron-beamcurrent is being used [215–218] or when they are grown on top of a perpendicular rod [219]. Despite the fundamental drive to improve the quality of IBID pillars, the understanding of the sidewall roughness and halo formation is still limited. Halos have been reported for EBID [216, 220], but not for IBID. Some authors attribute the halo in EBID to the secondary electrons emitted from the substrate within the backscattering radius around the pillar base [216] and the primary electrons scattered from the pillars [216, 220]. Ishida et al. [221] and Igaki et al. [110] suggested that the origin of sidewall extensions of IBID pillars is atom relocation, either via sputtering and redeposition, via mixing in the collision cascade, or via surface diffusion. They attributed the outgrowth of these initial extensions to the decomposition induced by captured dispersed ions or electrons. Those authors demonstrated that the sidewall extensions can be removed by a subsequent FIB milling after IBID [221].

To understand the formation of rough sidewall surfaces and halos, we have to gain a better understanding of IBID mechanisms. A number of causes have been postulated to be operative in IBID [222], such as depositions by primary ions, sputtered atoms or ions, emitted secondary electrons and ion beam heating. Dubner et al. explained IBID in terms of ion-solid interaction (sputtering) because they found that the deposition yield was proportional to the calculated nuclear stopping power [184–186]. Shuman et al. reported a significant contribution of secondary electrons to IBID [223]. Fujita et al. observed a Ga-rich core and a carbon outer shell in IBID pillars by transmission electron microscopy (TEM) and they suggested that secondary electrons are responsible for the formation of the outer shell [105, 210, 211]. In Section 3.5, we report a new method of distinguishing the deposition induced by secondary electrons from the other processes in IBID pillar growth. This distinction is achieved by changing the surface charging conditions. The formation of the irregular

3.2.3 Proximity effect in IBID of pillars

The rough sidewall surface and the halo formed on the pillar base are issues in connection with a single pillar growth. For pillar array growth, we have frequently observed changes in shape and dimension of the existing pillars as well as changes in the newly grown pillar when a second pillar grows near an existing pillar. Despite the fundamental drive to explore the capabilities and limitations of IBID to fabricate complex 3D nanostructures and improve the quality of IBID 3D nanostructures, the knowledge of this proximity effect is still limited, though these effects are commonly encountered in IBID repair of photolithography masks and integrated circuit modification. So far, the proximity effect of pillar growth has only been reported for EBID [216, 224, 225], but not for IBID. Kislov et al. observed that an existing tungsten pillar becomes broader and bends toward a neighboring new pillar [224]. The same effect was observed by Mitsuishi et al. for carbon pillars [225]. Both sets of authors considered the broadening to be the result of additional deposition induced by secondary electrons emitted from the newly growing pillar [224, 225]. They attributed the bending to an electrostatic force between the two neighboring pillars [224, 225]. Lau et al. [216] observed that an existing cobalt-containing pillar was broadened and had a lower metal content than the nearby newly grown pillar. They explained this effect as the result of additional deposition on the first pillar during the growth of the second pillar. In Section 3.6, we report our investigation on the proximity effect of Ga⁺ and He⁺ IBID pillar growth. Effects of the scattering of particles (primary ions, secondary electrons and atoms), the precursor coverage, and the substrate charging are discussed.

3.3 Experimental

Ga⁺ IBID experiments were performed in a combined Ga⁺ FIB and SEM system (FEI STRATA DualBeam DB235). A metal-organic gas (CH₃)₃Pt(C_PCH₃) was used as Pt precursor. A nozzle measuring 400 μ m in diameter was located 450 μ m above the substrate surface at an angle of 34° to the normal of the surface, and at the left side in all images taken. The gas injection system (GIS) setup is shown in Fig. 3.1a. The background chamber pressure was 5.5×10^{-7} mbar and during growth it was 3.3×10^{-6} mbar. To ensure a constant precursor gas supply, the gas was introduced into the chamber 60 s before the ion beam. Pillars were grown by a 1 pA 30 keV Ga⁺ FIB (the estimated diameter was 10 nm [107]) at an incident angle 0° (perpendicular to the substrate surface), either in spot mode (the beam stays at the same spot during the growth) or in a raster scanning manner.

The Ga⁺ IBID process and fabrication procedure are described as below. The deposition sites on conducting Si substrate were addressed by positioning the Ga⁺ at selected sites, which was realized by adjusting the ion beam shift values. Pillars were

grown within a range of 100 μ m surrounding the zero beam shift point. Three pillars were grown at the zero beam shift point (x = 0, y = 0, green spot) and two sites with beam shifts (x = -70 μ m, y = -30 μ m, red spot) and (x = 100 μ m, y = 100 μ m, blue spot) (Fig. 3.1b). The impinging precursor flux distribution on the substrate surface, which depends on the precursor flow rate and nozzle setup, was simulated by a GIS simulator program (Fig. 3.1c) [158]. The substrate temperature between 10 and 36 °C was controlled by a cascade of Peltier elements with an aluminum heat absorber mounted on the stage. The temperature was measured with a chromel-alumel thermocouple. For pillar growth, the Ga⁺ beam is raster scanned with a pixel dwell time of τ_d , and returns to the same pixel after its refreshment time of τ_r . In this work, τ_d and τ_r were chosen between 0.1 and 4.0 ms and between 0.4 and 32 ms, respectively. Pillars were grown in spot mode with a beam shift (-50 μ m, 0 μ m) in the experiments of the substrate temperature dependence, of the ion beam dwell time dependence, and of the precursor refreshment time dependence. Grown pillars were imaged by SEM inspection.

For the experiments of fabricating smooth and narrow pillars, the substrate was a double-polished Si wafer with 45-nm-thick $\mathrm{Si_3N_4}$ top and bottom layers and a $400\times400~\mu m^2$ window at one side (Fig. 3.2a). Series of pillars were grown at different locations on the conducting bulk Si surface (A in Fig. 3.2a) and on the insulating $\mathrm{Si_3N_4}$ membrane (B). To vary the charging conditions, some pillars (C) were grown near conductive Pt lines that connect the insulating $\mathrm{Si_3N_4}$ window to the conducting bulk Si surface. All pillars were grown at room temperature for 180 s, unless specified otherwise.

For the experiments of the proximity effect, the substrates used were a conducting Si wafer with or without a 30-nm-thick Cu coating layer, and a Si wafer with a 45-nm-thick Si_3N_4 top layer and a $400\times400~\mu\text{m}^2$ insulating Si_3N_4 membrane window. To vary the surface charging conditions on the insulating Si_3N_4 surface, some pillars were grown near a conductive Pt line, which connects the Si_3N_4 window to the conducting bulk Si surface. In some other cases, a similar Pt line was laid down near the pillars after their growth to enhance their visibility during SEM imaging. All pillars were grown in spot mode for 180 s at room temperature on the same sample. The pillar separation was selected by moving the sample stage instead of shifting the ion beam. Thus, the distance between the nozzle and the beam impact point was the same for every pillar. Tilted 59^o SEM images were taken for determining the diameter and height of the grown pillars. The measurement of the pillar diameter (FWHM) did not include the side-wall extensions (Fig. 3.22a).

These experiments of He⁺ IBID were performed in a Carl Zeiss OrionTM plus scanning helium ion microscope (HIM) with an OmniGIS unit. The substrate used was a conducting bulk Si. The same precursor $(CH_3)_3Pt(C_PCH_3)$ was used; its reservoir was heated to 30 °C during deposition. A carrier gas N₂ was added to the $(CH_3)_3Pt(C_PCH_3)$ precursor gas in pulses of 1 s per cycle of 10 s. The precursor continuously flows from the right sides in all the He⁺ IBID images taken. The background pressure in the chamber was 6.3×10^{-7} mbar and the pressure during growth was 4.5×10^{-6} mbar. Pillars were grown with a 25 keV He⁺ beam in spot mode.

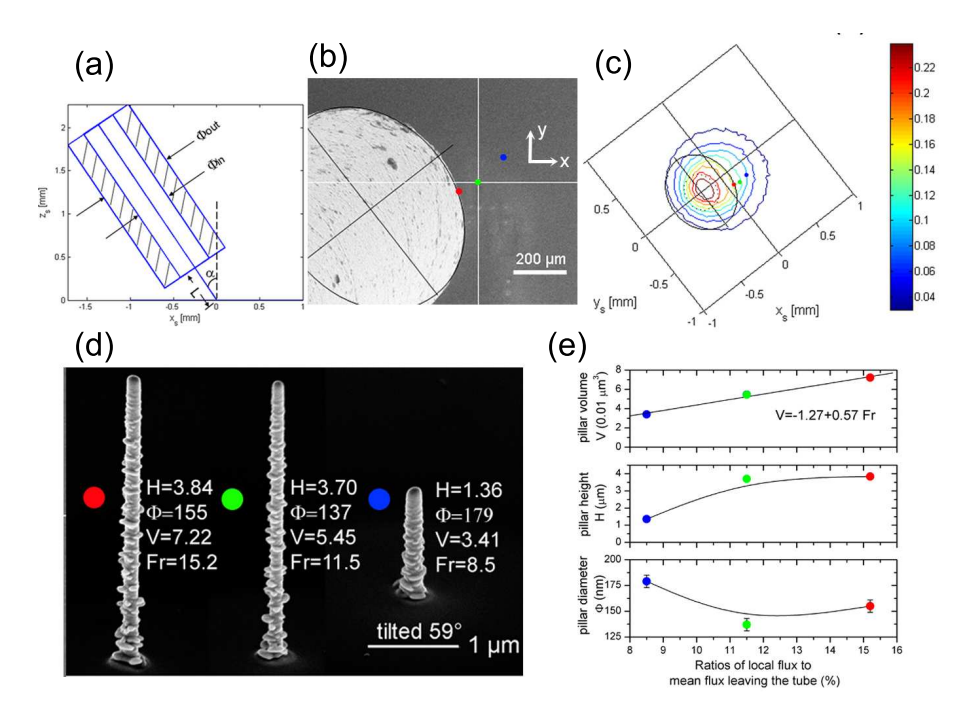


Figure 3.1: Dependence of pillar dimensions on local gas flux distribution. (a) GIS setup: the nozzle of 400 μ m diameter above substrate surface L = 450 μ m and at an angle of $\alpha = 34^{\circ}$. The outer and inner diameters are 0.85 and 0.4 mm, respectively. (b) SEM top view of the nozzle and three deposition sites (green, blue and red spots). (c) Calculated impinging precursor gas flux distribution expressed by the ratios of the local flux on the substrate surface to the mean flux at the exit of the nozzle. (d) SEM images of the pillars grown at three sites; (e) the heights H (μ m), diameters ϕ (nm) and volumes V (0.01 μ m³) of the pillars shown in (d), and the ratios of the local flux at the growth site to the mean flux leaving the tube Fr (%). Pillars were grown in spot mode at room temperature. The exposure time for each pillar was 180 s. The precursor nozzle is at the left side of the images.

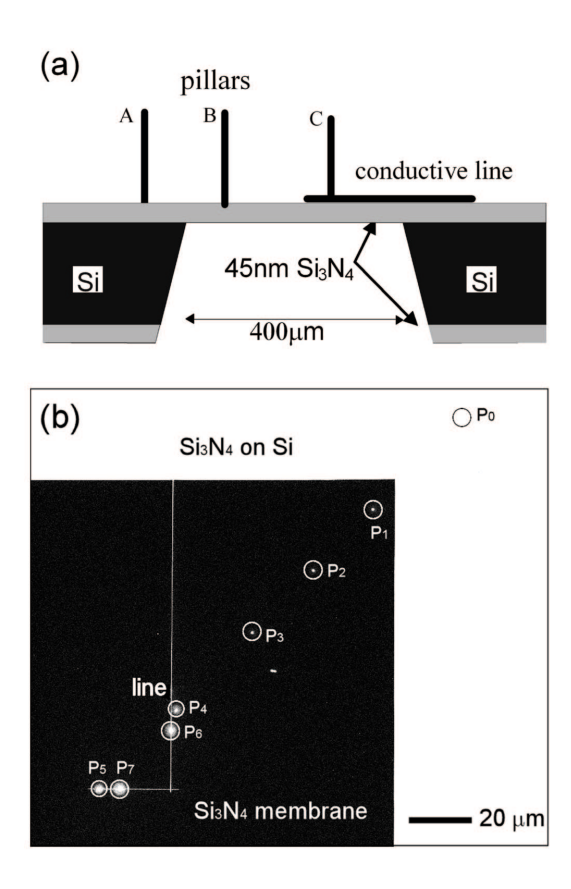


Figure 3.2: (a) Sketch of the Si sample plus a suspended insulating Si_3N_4 membrane with pillars grown on three locations. A: on the conducting bulk Si substrate; B: on the insulating membrane Si_3N_4 ; C: on the insulating Si_3N_4 membrane next to a conductive Pt line. (b) SEM top view of pillars (encircled in the figure) grown at different locations. P_0 on conducting bulk Si substrate; P_1 to P_5 on the insulating Si_3N_4 membrane; P_6 and P_7 grown after deposition of two conductive Pt lines. Pillars were grown in spot mode at room temperature for 180 s. The precursor nozzle is at the left side of the images.

The substrate material was conducting bulk Si with 1.0 nm native oxide. For the experiments of the process dependence, different currents from 0.6 to 5.5 pA were used for pillars grown in spot mode with a same dose of 6.0 pC. For the experiments of the proximity effect, arrays of deposits were grown in spot mode with exposure times between 1 and 9 s. The spatial separations between the deposits ranged from 50 to 1000 nm.

3.4 Process dependences of IBID pillar growth

3.4.1 Pillar growth by Ga⁺ IBID

Local gas flux distribution dependence

As shown in Figs. 3.1c and d, in close proximity, the pillar height increases while the diameter first decreases then increases slightly. The change of the pillar volume is proportional to the change of the local precursor flux at the deposition site.

Substrate temperature dependence

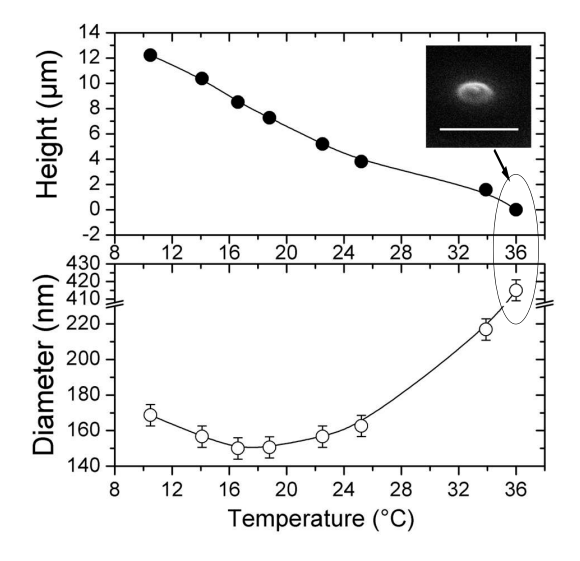


Figure 3.3: Dependences of pillar dimensions on substrate temperature. Heights and diameters of pillars grown in spot mode with different temperatures for 180 s, the insert is an SEM image of one pillar (scale bar 1 μ m, tilted 52°). The precursor nozzle is at the left side of the images.

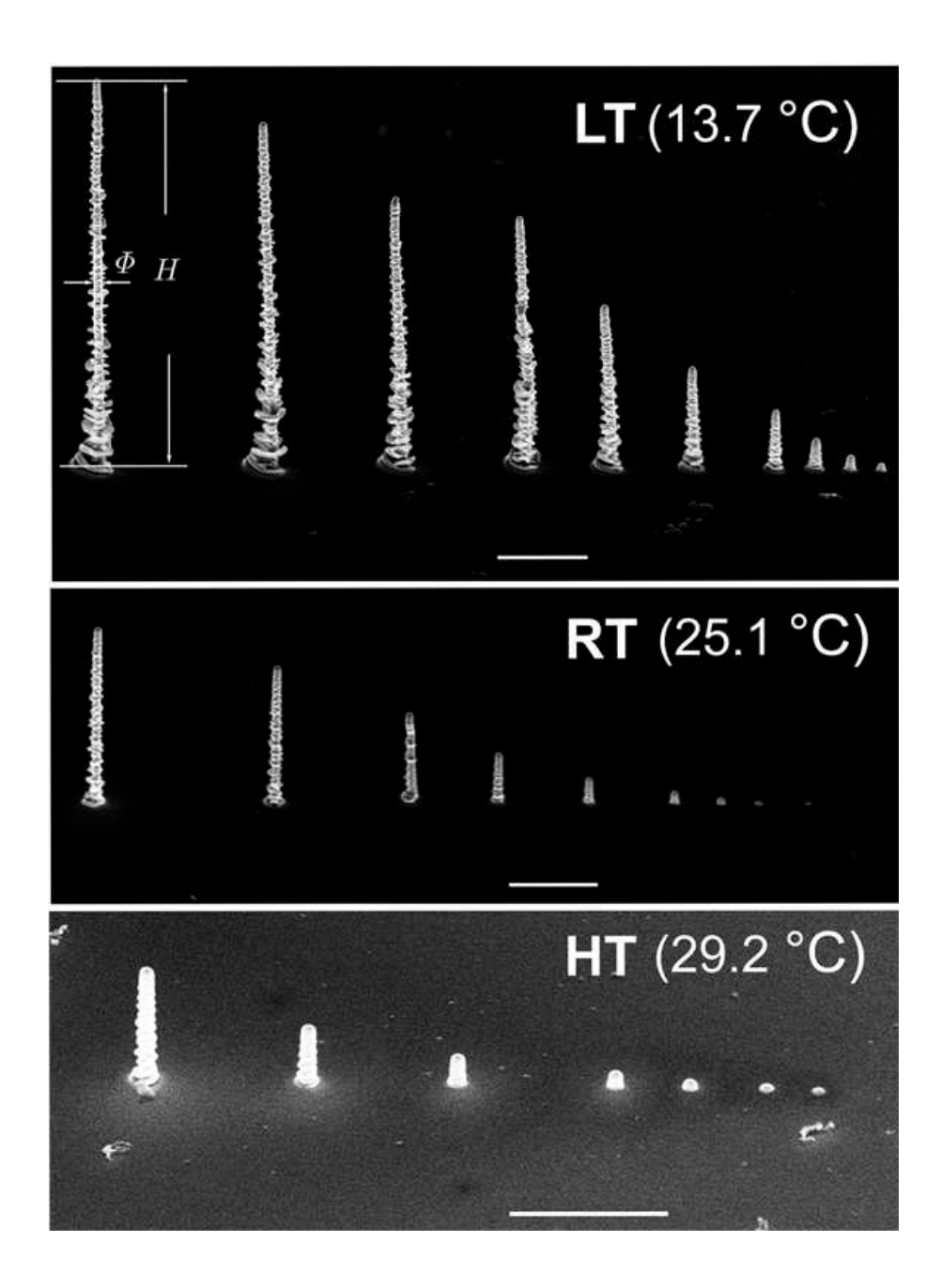


Figure 3.4: Dependences of pillar dimensions on substrate temperature and exposure time. SEM images of pillars grown in spot mode with different substrate temperatures and exposure times (2-264 s) (scale bar 2 μ m, tilted 52°). The precursor nozzle is at the left side of the images.

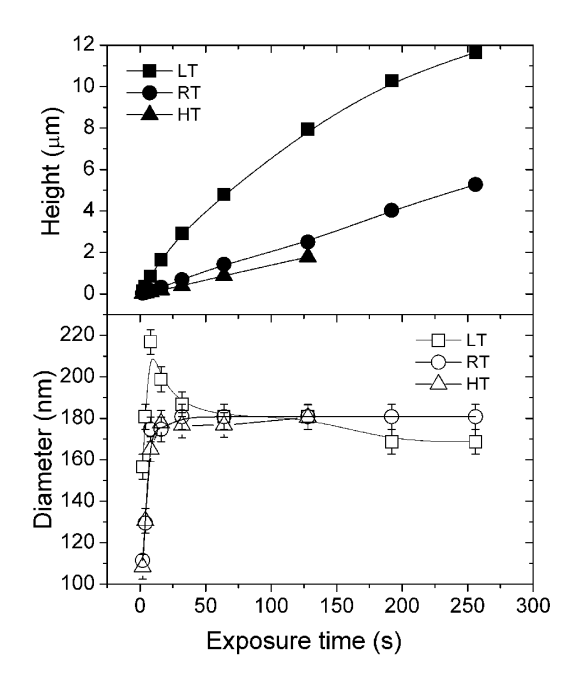


Figure 3.5: Dependences of pillar dimensions on substrate temperature and exposure time. Heights and diameters of three pillar groups (shown in Fig. 3.4).

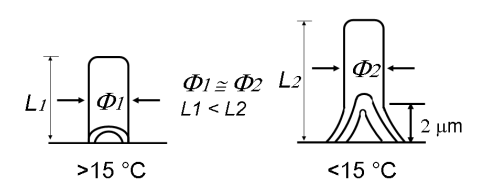


Figure 3.6: Sketches of pillar formation above and below 15 $^o\mathrm{C}.$

With increasing substrate temperature T, the pillar height decreases significantly. The diameter barely changes below 25 °C but increases above 25 °C (Fig. 3.3). Surprisingly, at 36 °C nearly nothing was grown vertically, but pancake-like deposits have appeared (insert in Fig. 3.3). Figure 3.4 shows the exposure time dependence for pillars grown at three different substrate temperatures 13.7 °C (LT), 25.1 °C (RT), and 29.2 °C (HT). At RT and HT, the growth rate remains more or less constant between 2 and 256 s, whereas at LT it starts high but decreases continuously. The stabilized diameter decreases slightly at LT, whereas it remains constant at RT and HT. Additionally, it is interesting to note that at LT, the pillars have an asymmetric skirt-shaped bottom (note that the nozzle is located at the left side of the image) and only becomes cylindrical above 2 μ m (Fig.s 3.4 and 3.6).

Ion beam dwell time and precursor refreshment time dependence

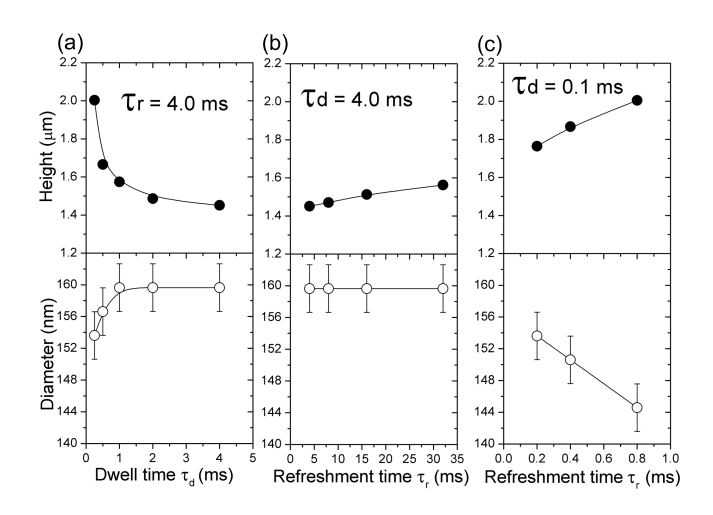


Figure 3.7: Dependences of pillar dimensions on the ion beam dwell time τ_d and the precursor refreshment time τ_r . Diameters and heights of pillars grown with (a) different τ_d and a long τ_r of 4.0 ms; (b) different τ_r and a long τ_d of 4.0 ms or (c) same, but a short τ_d of 0.1 ms. The exposure time for each pillar was 60 s.

Series of pillar arrays were grown with different beam dwell times τ_d and precursor refreshment times τ_r but with the same exposure time of 60 s for each pillar. In order to minimize the influence of insufficient precursor refreshment, a long refreshment time of 4.0 ms was chosen to investigate the dwell time dependence. With increasing dwell time, the pillar height decreases while the pillar diameter increases only slightly (Fig. 3.7a). With increasing refreshment time, the increase of the height is more pronounced for a short dwell time of 0.1 ms than for a long one of 4.0 ms. In both cases, the diameter changes only slightly (Fig. 3.7b,c). With an optimal combination of these parameters (a short dwell time and a reduced temperature) the growth rate is about 10 times higher than that in spot mode and at room temperature, whereas

the resolution is almost unaffected (Fig. 3.8).

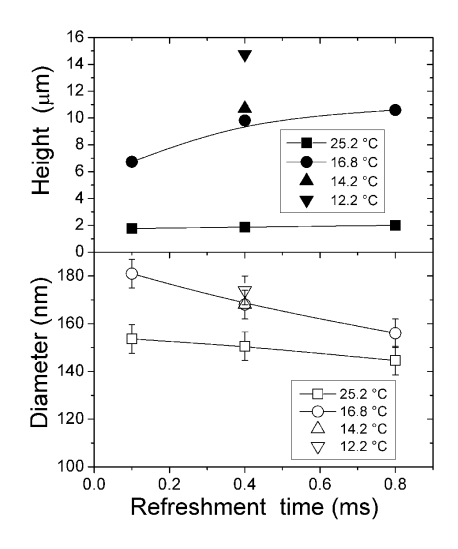


Figure 3.8: Effects of different variable parameters: temperature T, and the refreshment time τ_r . Diameters and heights of pillars grown with a short τ_d of 0.1 ms. The exposure time for each pillar was 60 s.

3.4.2 Pillar growth by He⁺ IBID

With HIM, we managed to grow pillars for the first time. HIM images of the deposits grown with different He⁺ currents are shown in Fig. 3.9. The diameter, the height and the deposition yield are shown in Fig. 3.10. The deposits are cones at low currents and cylinders with conical tops-pillars-at higher currents. The pillar height decreases continuously with increasing beam current, while its diameter increases. With increasing beam current from 0.6 to 5.5 pA, the deposition yield, which is expressed as volume per incident ion, decreases slightly.

3.4.3 Comparison of Ga⁺ and He⁺ IBID pillar growth

As we have conducted substantial IBID research using both Ga^+ and He^+ , it is interesting to compare Ga^+ and He^+ IBID pillar growth with the same precursor $(CH_3)_3Pt(C_PCH_3)$, as shown in Fig. 3.11 and Table 3.1. In the case of He^+ IBID the vertical growth rate is 10 times faster, whereas the pillars are 3 to 4 times narrower. In addition, He^+ IBID pillars always have a very smooth sidewall and a cone-shaped top, whereas Ga^+ IBID pillars have a rough sidewall and a relatively flat top [209]. These differences can be related to the different projected ranges (Fig. 1.8) and the different interaction volumes (Fig. 3.13) of ions in the deposit. According to SRIM simulation, in the typical He^+ IBID deposits $Pt_{0.15}C_{85}$, the projected range and

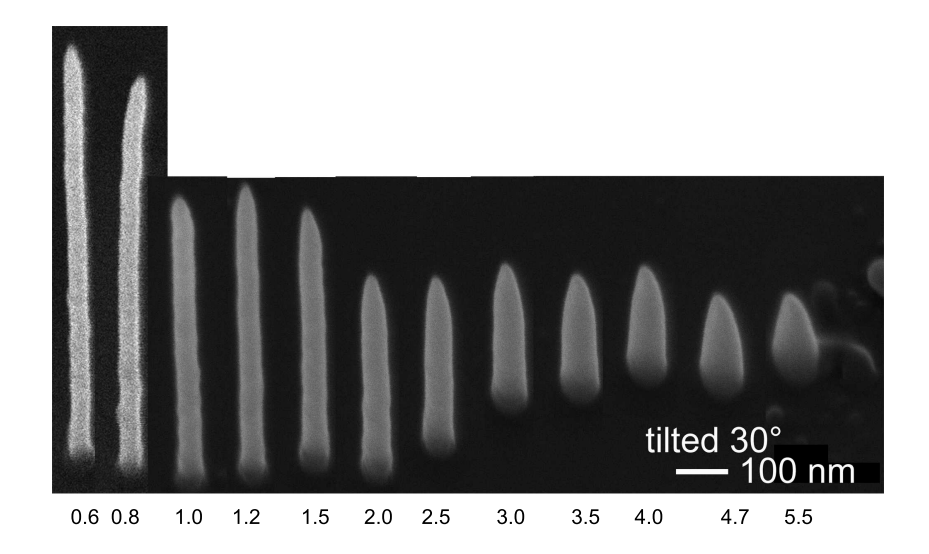


Figure 3.9: Beam current dependences of $\mathrm{He^{+}}$ IBID pillar growth. A compilation of several HIM tilted 30^{o} images of pillars grown in spot mode with different currents but the same doses of 6.0 pC. Beam currents (pA) are indicated under the corresponding pillars.

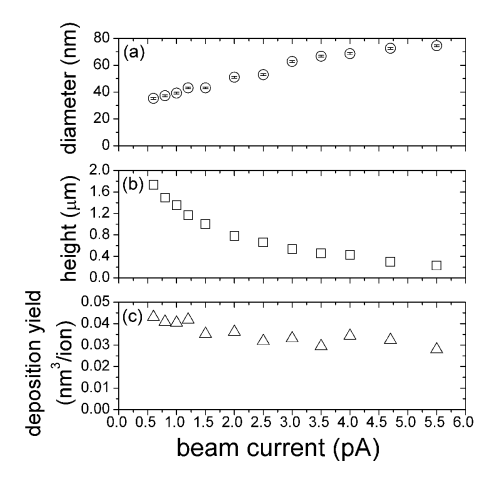


Figure 3.10: Dependences of He⁺ IBID pillar growth on beam current. (a) the pillar diameter at half height; (b) the pillar height and (c) the deposition yield of pillars shown in Figure 3.9.

straggling of He⁺ (25 keV) are 140 nm and 75 nm, whereas in the typical Ga⁺ IBID deposits Pt_{0.40}C₆₀, those of Ga⁺ (30 keV) are 13 nm and 8 nm. Therefore, precursor decomposition by scattered He⁺ ions takes places in a larger area than in the case of scattered Ga⁺ ions. Thus, under similar practical conditions there will be less depletion in He⁺ IBID than in Ga⁺ IBID, resulting in taller cone-like tops and faster vertical growth. Furthermore, compared to Ga⁺, He⁺ has lighter mass. Therefore, scattering is weaker and the interaction region close to the surface where the deposition happens is smaller [41]. As a consequence, a better resolution of IBID can be achieved by He⁺, especially when the sub-nm beam is being used. The different top shapes can also be caused by different sputtering yields of He⁺ and Ga⁺. It seems that the weak sputtering of He⁺ preserves the sharp pillar top, whereas the Ga⁺ IBID pillar flattens due to the strong sputtering. The deposition yield of the He⁺ IBID pillar is comparable to the box deposition yield of Sanford et al., which ranges from $3.8 \text{ to } 9.6 \times 10^{-2} \text{nm}^3/\text{ion } [89]$. We find that for pillar growth Ga^+ and He^+ IBID have very similar deposition yields (Table 3.1). We also note that the mechanism of Ga⁺ IBID is explained by sputtering (collision cascades) [88, 226]. Hence, the similar deposition yields but very different sputtering yields of Ga⁺ and He⁺ indicate that Ga⁺ IBID and He⁺ IBID have different mechanisms. We will discuss IBID mechanisms in detail in Chapter 4. The deposits of He⁺ IBID do not have Ga contamination, which is clearly an advantage over Ga⁺ IBID. According to the work of Sanford et al., the Pt atomic composition of the deposits of He⁺ IBID is only about 8-17 % measured by EDX analysis [89], which is much lower than the typical value 35-45% for Ga⁺ IBID. Overall, except for a lower Pt atomic composition, He⁺ IBID has advantages over Ga⁺ IBID with regard to the pillar growth.

Table 3.1: Comparison of IBID pillars grown in spot mode by 1.0 pA 25 keV He⁺ and 1 pA 30 keV Ga⁺. All data are from the current experiments, unless otherwise indicated.

	He ⁺	Ga^+
Ventical amounth note (non/g)	225	19
Vertical growth rate (nm/s)	420	19
Diameter(nm)	39	142
Deposition yield (nm ³ /ion)	4.05×10^{-2}	4.79×10^{-2}
Ga contamination	no	yes
(0.4)		
Pt atomic composition (%)	8-17 [89]	35-45

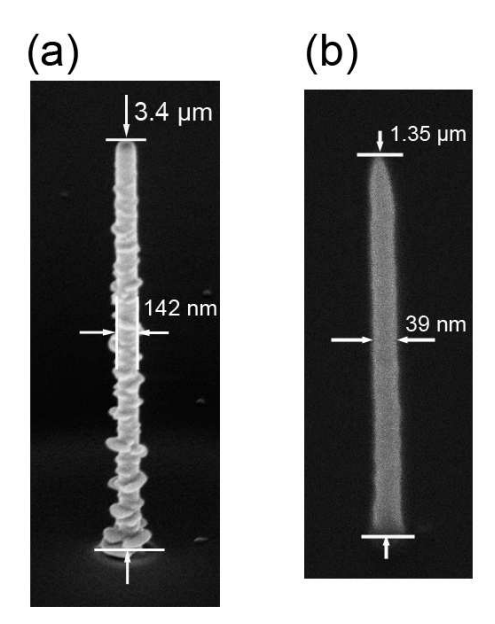


Figure 3.11: Comparison of typical Ga^+ and He^+ IBID pillar growth. (a) SEM tilted 59^o image of a pillar grown by 1 pA 30 keV Ga^+ in spot mode for 180 s; (b) HIM tilted 30^o image of a pillar grown by 1.0 pA 25 keV He^+ in spot mode for 6 s.

3.4.4 Discussion

To understand the process dependences of IBID, we summarize here the relevant models of IBID and EBID. So far, most models treat EBID, and IBID is similar to EBID except for the sputtering involved in IBID. The net deposition of IBID is the total deposition minus the sputtering. Thus, the deposition rate R [nm/s] at surface position r of EBID (or IBID) can be expressed by [88, 183]

$$R(r) = Vn(r) \int_0^{E_{PE}} \sigma(E) f(r, E) dE = Vn(r) \sigma f(r)$$
(3.1)

where V [nm³] is the volume of the decomposed molecule, n(r) [nm⁻²] is the number of adsorbed molecules per surface unit, $\sigma(E)$ [nm² eV⁻¹] is the energy-dependent electron (or ion) impact dissociation cross section, E_{PE} is the energy of the PEs (PIs), and f(E,r) [nm⁻² s⁻¹] describes the spatial flux distribution of the electron (or ion) with energy E generated by the PEs (PIs). As the $\sigma(E)$ data of adsorbed molecules is not available, we use the simplified expression in Eq. 3.1, where σ [nm²] represents an integrated value over the energy spectrum.

It is well known that the precursor adsorbs, desorbs, and diffuses on the substrate surface at a rate that is a function of the local gas pressure and the substrate temperature. To interpret the complex process of EBID and IBID, Utke presented a molecule adsorption rate (dn/dt) model [88, 183]

$$\frac{\partial n}{\partial t} = \underbrace{sJ(1 - \frac{n}{n_0})}_{adsorption} + \underbrace{D(\frac{\partial^2 n}{\partial r^2} + \frac{1}{r}\frac{\partial n}{\partial r})}_{diffusion} - \underbrace{\frac{n}{\tau}}_{desorption} - \underbrace{\frac{\sigma f n}{\sigma t}}_{decomposition}$$
(3.2)

where J [nm⁻² s⁻¹] is the impinging precursor flux, s is the sticking probability, n/n_0 is the relative coverage, n_0 is the maximum monolayer coverage (the number of available adsorption sites), which is usually taken as the inverse of the molecule size, D [nm² s⁻¹] is the diffusion coefficient, and τ [s] is the residence time of the precursor molecule. Here it is assumed that no multilayer adsorption can take place. All parameters other than n(r,t) and f(r,t) are considered constant. Note that, except s which is dependent on the properties of the precursor molecule and the substrate surface and hence not easily controlled, J and τ can be controlled by adjusting regular EBID or IBID parameters as the precursor pressure and the substrate temperature.

However, the parameters in Eq. 3.2 are rarely known, which makes a quantitative analysis still difficult. Despite these difficulties, some EBID simulations have been developed, although simulations dedicated to IBID are still not available. Here, we summarize the relevant models that deal with pillar growth. For a high kinetic energy electron beam (200 keV), Silvis-Cividjian et al. used a 2D dynamic profile Monte Carlo (MC) simulator to simulate pillar growth as a function of exposure time, based on the assumption that the irradiated area is permanently covered with a monolayer of precursor molecules [227]. The authors concluded that the ultimate resolution of the pillar depends on the spatial distribution (up to 20-30 nm in diameter) of the emitted secondary electrons.

Solving the steady state of the depletion and the replenishment of the precursor molecule during EBID, Utke introduced several fundamental dimensionless parameters and simulated the EBID process as functions of these parameters [88, 183]. The spatial distribution of the emitted secondary electrons is assumed to be equal to that of the incident primary electron beam, which is actually only applicable for the low-aspect ratio deposits when the incident beam size is large. Thus, the simulation results were correlated only to experimental results of a low kinetic energy (5 keV) and broad (beam size 110 nm) electron beam. In addition, the simulation is based on a planar surface, but not on a pillar.

One dimensionless parameter is the dimensionless deposition resolution, which is defined as the ratio of the full width at half maximum (FWHM) of the deposit and the incident beam:

$$\tilde{\varphi} = FWHM_D/FWHM_B \tag{3.3}$$

where $FWHM_D$ and $FWHM_B$ are full widths at half maximum of R(r) and f(r), respectively.

For steady-state $(\partial n/\partial t=0)$, solving Eq. 3.2 and neglecting the diffusion, one finds:

$$n(r) = \frac{sJ}{\frac{sJ}{n_0} + \frac{1}{\tau} + \sigma f(r)} \equiv sJ\tau_{eff}(r)$$
(3.4)

where $\tau_{eff}(r)$ is defined as the effective residence time. The effective residence times in the center of the beam and far away from the center are $\tau_{in} \equiv \tau_{eff}(0)$ and $\tau_{out} \equiv \tau_{eff}(r \rightarrow \infty)$. A dimensionless ratio

$$\tilde{\tau} \equiv \frac{\tau_{out}}{\tau_{in}} = 1 + \frac{\sigma f_0}{1/\tau + sJ/n_0} \tag{3.5}$$

represents a measure for depletion due to dissociation. The idealized case of zero depletion corresponds to $\tilde{\tau}$ =1.

With a Gaussian beam $f(r)=f_0\exp(-r^2/2a^2)$, a is the standard deviation which is related to FWHM_B as FWHM_B = $2\sqrt{2ln2}a$, $\tilde{\varphi}$ can be expressed as a function of irradiative depletion of the precursor molecules:

$$\tilde{\varphi} = (\log_2(1+\tilde{\tau}))^{1/2} \tag{3.6}$$

Numerically solving Eq. 3.2 for steady-state and the boundary conditions $n(r\to\infty)=n_{out}=s$ J τ_{out} and dn(r=0)/dr=0, $\tilde{\varphi}$ can also be expressed as a function of diffusive replenishment [88, 183]:

$$\tilde{\varphi} \approx (\log_2(2 + (\tilde{\rho})^{-2}))^{1/2} \tag{3.7}$$

where the diffusive replenishment is described by the dimensionless ratio $\tilde{\rho}=2\rho_{in}/\text{FWHM}_B$, and ρ_{in} is the molecule diffusion distance in the center of the beam: $\rho_{in}=(D \tau_{in})^{1/2}$.

As shown in Fig. 3.12, less depletion and better replenishment correspond to a higher deposition rate and higher resolution. The continuum model is helpful to predict qualitatively the trend of how the vertical growth rate and the resolution change with the experimental parameters. However, as discussed above, the assumption implies that this continuum model is only applicable to low-aspect-ratio structure deposition with a broad beam on a planar surface, not to high-aspect-ratio pillar growth. The continuum model describes the early stage of the pillar growth. To simulate the high-aspect-ratio structure growth, Smith et al. have developed a more advanced 3D Monte Carlo-based simulation with gas-handling algorithms [207]. One of the significant features of this simulation is that the morphology of the deposit is continuously updated as well as the precursor coverage on the deposit surface. The Monte Carlo subroutines record the electron trajectory and energy as well as the generated secondary electrons (SEs) and preserve the energy spatial distribution as a function of time. However, an unknown factor is how the energy-dependent dissociation cross section varies with the different electron types, which have different energy spatial distributions. Furthermore, these distributions change with the morphology of the deposit as a function of time.

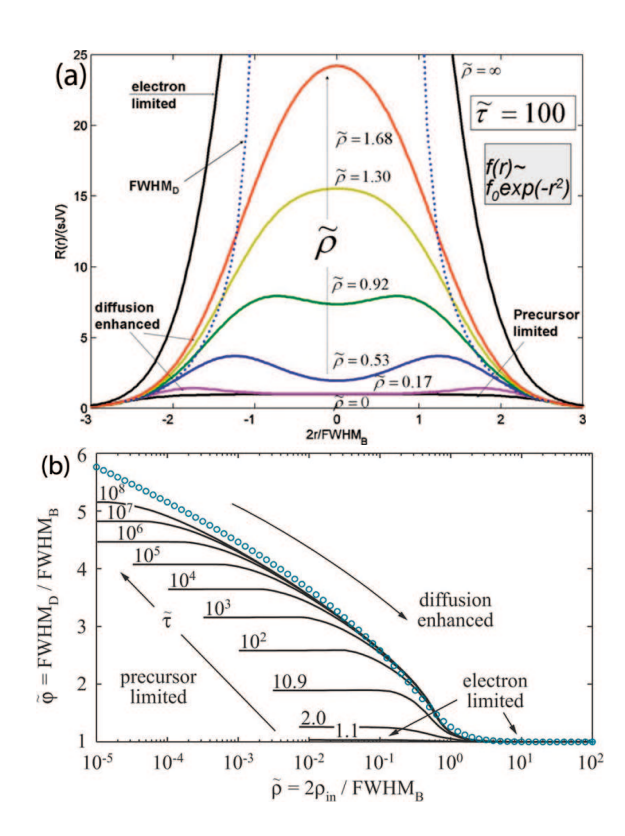


Figure 3.12: (a) Normalized steady-state deposition rate (R(r)/s J V)at indicated depletion representing the deposit shape. Note the shape transition from flat top $(\tilde{\rho}=0)$, indented $(\tilde{\rho}=0.17)$, round $(\tilde{\rho}=1.3)$, to Gaussian $(\tilde{\rho}=\infty)$ and the related decrease of the deposit FWHM (FWHM_D) with increasing diffusive replenishment $\tilde{\rho}$. (b) Normalized deposit size $(\tilde{\varphi})$ vs normalized diffusion path for varying depletion $(\tilde{\tau}$ as indicated). Circles represented the scaling law in Eq. 3.7. Adapted from Fig. 27 of [88].

Despite these difficulties, some important conclusions have been reached by Smith et al. The vertical growth is dominated by the primary electrons (PE) and secondary electrons type I (SE^I), which are generated by PE, whereas the lateral growth is dominated by forward-scattered electrons (FSE) and secondary electrons type II (SE^{II}), which are generated by back-scattered electrons [206] (Fig. 3.13). Consistent with the work of Utke [88, 183], as the growth regime changes from precursor-limited to electron-limited with increasing precursor supply, both the growth rate and the resolution increase [182, 207], whereas with decreasing the electron supply, only the resolution increases [207]. Furthermore, it is interesting to note that the relative contributions to the total deposition by these individual contributors (PE, SE^I, FSE, SE^{II}) change as the growth regime changes from precursor-limited to electron-limited: the relative contributions of PE and SE^I increase, whereas those of FSE and SE^{II} decrease, which correlates well with the variation of the vertical and the lateral growth rates [182, 207].

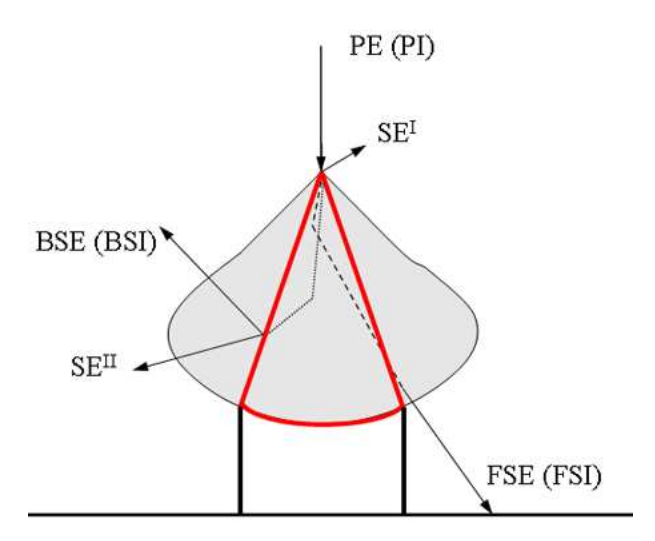


Figure 3.13: Schematic of the electron trajectory through an EBID pillar, where PE is the primary electron, FSE and BSE are forward and backscattered electron, SE^I and SE^{II} are the secondary electrons type I and II. The shaded area indicates the interaction volume of the electron. Note that the effective interaction volume is the part inside the pillar (marked by red line). The schematic is also applicable for the case of IBID.

Furthermore, Smith et al. also pointed out that the effective electron interaction volume (as shown in Fig. 3.13), which depends primarily on the energy of the electron beam and the species of the precursor materials, can also affect the vertical growth rate and the resolution of the pillar [182, 206, 207]. The effective interaction volume was not considered in the continuum model [88, 183]. The pillar width becomes saturated when the pillar height is longer than the vertical length of the interaction

volume (Fig. 3.13). The pillar width could also become saturated when the vertical growth is so slow that the pillar grows to a width where the interaction volume is fully encompassed within the pillar. The former case is applicable to most of EBID work in reality. Thus, the height of the cone-like top of EBID pillars depends mainly on the vertical length of the interaction volume. An example is that the SE yields are similar for electrons in SiO_2 and W, however, the interaction volume in SiO_2 is larger. Thus, the electrons in SiO_2 encounter more precursor molecules on average because of the larger surface area, which results in a broader pillar, a taller cone-like top and a higher deposition yield [196, 206].

There is a complex interplay between the vertical growth rate and the resolution [182, 207]. For instance, in the electron-limited regime, the vertical growth rate increases with decreasing beam energy, whereas the resolution remains almost the same, although it is expected to deteriorate due to the increased SE^{II} emission on the pillar sidewall with decreasing energy beam. This "contradiction" can be explained as follows: with decreasing energy beam, the electron interaction volume is reduced and the vertical growth rate is increased; hence the time for lateral growth is limited because the electron interaction volume "rises" faster through the pillar [207]. For a similar reason, the resolution actually improves with increasing vertical growth rate and surface diffusion efficiency, not as expected deteriorates due to the increased precursor coverage on the pillar sidewall [182].

With these models proposed by Utke [88, 183] and Smith [182, 206, 207], we try to understand the physical mechanisms behind our experiments. Qualitatively, the continuum model supports our experiments on pillar growth by Ga⁺ and He⁺ beams. We have observed that both the vertical growth rate and the resolution improve with increasing local precursor pressure, which results in a higher precursor adsorption (Fig. 3.1), and with decreasing substrate temperature, which results in a longer residence time (Figs. 3.3, 3.4, 3.5), and with increasing refreshment time or decreasing dwell time, which results in a better replenishment or less depletion (Fig. 3.7). We have also observed that the resolution improves with decreasing beam current, which results in less depletion (Figs. 3.9 and 3.10).

The very different pillars grown at different sites within a region of only 100 μ m region can be explained by the almost two fold difference of flux distribution in this region (Fig. 3.1). A higher precursor flux distribution results in taller and narrower pillars owing to better precursor replenishment. However, even with a higher flux distribution, the pillars became slightly thicker. We do not yet have good explanation for this thickness. However, we suspect that an optimized precursor flux is required to grow high-aspect-ratio pillars. Furthermore, it appears that the interplay between the vertical and lateral growth requires another model that considers the high-aspect-ratio structure growth. With decreasing substrate temperature, the residence time increases, which resulted in an increased precursor surface density, faster vertical growth rate and better resolution (Figs 3.3, 3.4 and 3.5). The diameter increases slightly for the temperature below 16 °C, which is caused perhaps by the external structures on the sidewall surface. The residence time is related to the substrate temperature as $\tau(T) = \tau_0 exp(E_{des}/(kT))$, where E_{des} is the activation energy for

desorption, and k is the Boltzmann constant. However, the quantitative description of the relationship between deposition and the substrate temperature is not as simple as that, due to remaining unknown factors such as E_{des} . As reported by Li et al. [181], E_{des} increases with decreasing electron beam current and decreasing beam energy in WF₆ deposition. This can partly explain the EBID experimental results which do not strictly follow a simple exponential relationship [90, 181, 198, 200-202]. With decreasing temperature, the diffusion coefficient decreases as $D(T) = D_0 exp(-E_{diff}/(kT))$, where E_{diff} is the activation energy for diffusion. However, the diffusion rate can also increase due to the reduced desorption, leading to an increased number of precursors on the substrate surface. Thus, the total effect of diffusion is still unknown. It is interesting to note that Li et al. reported that for medium or high beam currents the height of the EBID pillar first increases and then decreases with decreasing substrate temperature [181]. Li explained this, though the diffusion coefficient decreases with decreasing substrate temperature, the diffusion rate is still high enough to have an increasing number of molecules at the pillar top. Only at even lower temperatures, the diffusion coefficient decreases so much that most diffusing molecules decompose on the pillar sidewall surface and not many were able to reach the pillar top, meaning that the pillar height decreases. The decrease of the growth rate in our experiment with increasing exposure time at LT is unlikely due to beam-induced heating, which, as reported in the literature, causes higher desorption in the case of EBID (Figs. 3.4) and 3.5) [217, 218, 228]. For a 5- μ m-tall pillar with a diameter of 150 nm, the estimated heat increase is only 0.11 K assuming the thermal conductivity of pure platinum 71.6 $W/m \cdot K$ [218]. Possibly, the decrease of the growth rate is due to the lower diffusion to the pillar top with increasing pillar length. We suspect that the skirt-shaped bottom of the pillar grown at LT is caused by the accumulation of precursor molecules on the cooled substrate surface due to the lower desorption rate and to the decomposition by the scattered primary ions and secondary particles. Short dwell times reduce the precursor decomposition in each loop and long refreshment times increase the precursor adsorption and diffusion (Figs. 3.7a-c), which has also been demonstrated by Fowlkes [203]. The combined variation of the temperature, the dwell- and refreshment-times shown in Fig. 3.8 suggests that increasing the precursor surface density is indeed effective to enhance the pillar growth rate, without affecting the resolution. For He⁺ IBID, with constant precursor supply and increasing beam current, the deposition yield decreases continuously (Fig. 3.10). The precursor depletion increases with increasing beam current, resulting in a decrease of the vertical growth rate and the resolution (Figs. 3.9 and 3.10).

As discussed, the simplified continuum model should not be overinterpreted in terms of quantity, and it is especially not perfectly applicable for high-aspect-ratio structure growth. Nevertheless, to gain a quantitative understanding of the process of IBID pillar growth, we tried to calculate the relationship between the He⁺ beam current and the vertical growth rate and the resolution using Eqs. 3.1 and 3.2. The case of Ga⁺ IBID is supposed to be even more complicated because it also involves sputtering. Therefore, we do not include the calculation of Ga⁺ IBID in this dissertation. For steady state $(\partial n/\partial t = 0)$, solving Eq. 3.2 and neglecting the diffusion term, we have $n(r) = sJ\tau_{eff}(r)$ (Eq.3.4).

The growth rate R(r) is expressed as

$$R(r) = V s J \tau_{eff}(r) \sigma f(r) = \frac{(V s J) f(r)}{\left(\frac{sJ}{n_0 \sigma} + \frac{1}{\tau \sigma}\right) + f(r)}$$
(3.8)

For the vertical growth rate R_v , for simplicity, we assume r = 0.

$$R_v = R(0) = \frac{(VsJ)f_0}{(\frac{sJ}{n_0\sigma} + \frac{1}{\tau\sigma}) + f_0}$$
(3.9)

The beam current I is

$$I/e = 2a^2 f_0(\int_{-\infty}^{\infty} exp(-x^2)dx) \cdot (\int_{-\infty}^{\infty} exp(-y^2)dy) = 2a^2 \pi f_0$$
 (3.10)

where e is the elementary charge.

Thus, R_v can be expressed in the beam current I,

$$R_v = \frac{P_1 I}{P_2 + I} {(3.11)}$$

where two constants are $P_1 \equiv VsJ$; $P_2 \equiv 2a^2\pi \ e \ (\frac{sJ}{n_0\sigma} + \frac{1}{\tau\sigma})$.

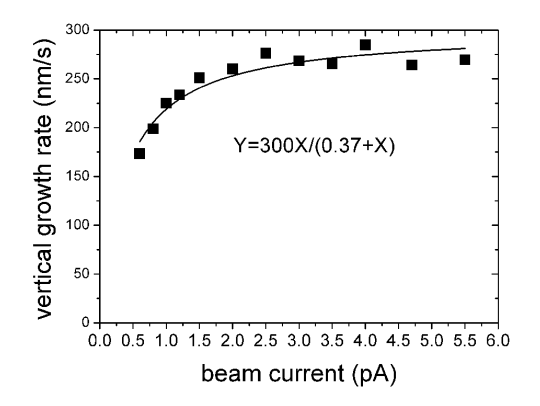


Figure 3.14: Experimental vertical growth rates of He⁺ IBID pillars grown with different beam currents and same doses, shown with the fitting curve neglecting diffusion.

As shown in Fig. 3.14, the experimental vertical growth rates agree quite well with the model, though diffusion was neglected in the calculation. For low beam currents (<1 pA), the vertical growth rate tends to be proportional to the beam current. This indicates an ion-limited (-like) regime, thus the replenishment of the precursor is sufficient to prevent the depletion. In addition, these results also illustrate that in practice most IBID experiments are conducted without sufficient replenishment of the precursor. For high beam currents (>2.5 pA), the vertical growth rate saturates at a level of VsJ [nm/s]. The vertical growth rate is then independent of the beam current,

which indicates that all precursor molecules are consumed rapidly by the dissociation. Clearly, the growth regime becomes precursor-limited. It is interesting to note that there is a transition between the ion-limited and precursor-limited regime.

The product of V s J is 300 nm s⁻¹. To determine the sticking probability s, the precursor flux J and the volume of the decomposed molecule V have to be known. The vapor pressure of the precursor $(CH_3)_3Pt(C_PCH_3)$ is 0.115 mbar [107] for a precursor reservoir temperature of 30 oC ; the background pressure is 6.3×10^{-7} mbar; the diameter of the nozzle d is 400 μ m, the length of the nozzle L is assumed to be 3 cm. The throughput of the precursor flux $J[m^{-2} s^{-1}]$ is

$$J = \frac{Q}{A} = \Delta PW \frac{1}{\sqrt{2\pi mkT}} \tag{3.12}$$

where A [m²] is the cross section of the nozzle, ΔP [Pa] is the pressure difference from the nozzle entry to the nozzle exit, W is the transmission probability of a molecule in a molecular flow going through the nozzle, which is approximately to 4d/3L [229], k is the Boltzmann constant (1.38 × 10⁻²³ J K⁻¹), T is the temperature (303 K), m is the molecular weight (1.66×10⁻²⁷× 319.30 kg for (CH₃)₃Pt(C_PCH₃)).

Hence J is 1.72×10^3 molecules nm⁻² s⁻¹. This value is comparable to the gas flux calculation for the same precursor as reported by Puretz [230]. However, J is the mean flux at the exit of the nozzle. The flux at the deposition site should be 5-10 times lower, as shown in Fig. 3.1. Taking the diameter of the decomposed molecule to be the same as the precursor molecule (CH₃)₃Pt(C_PCH₃) (0.78 nm [88, 231]), the volume V is 0.248 nm³ and n₀ = 1.9 molecules nm⁻². Therefore the sticking probability s is 3.5-7.0. However, from a physical point of view, it is impossible that the sticking probability greater than 1. This margin of error can be caused by the diffusion which is not included in this model.

We found that P_2 (\equiv e $2a^2\pi$ ($\frac{sJ}{n_0}+\frac{1}{\tau}$) $\frac{1}{\sigma}$) is 0.37 pA (see 3.14), and we know that $FWHM_B=2\sqrt{2ln2}\,a=1$ nm. Assuming τ to have a typical value of 1 ms [88], the decomposition cross section σ is 7.9×10^{-4} nm², which is much lower than for Ga⁺ IBID [88]. This seems unlikely considering the observed similar deposition yields of He⁺ IBID and Ga⁺ IBID (Table 3.1). However, this discrepancy can be explained by the exclusion of diffusion in this model.

The pillar width can be estimated from the FWHM of the growth rate profile $R(r_{1/2})$.

$$R(r_{1/2}) = \frac{P_1 f_0 exp(-r_{1/2}^2/2a^2)}{P_3 + f_0 exp(-r_{1/2}^2/2a^2)} = \frac{1}{2}R(0) = \frac{1}{2}\frac{P_1 f_0}{P_3 + f_0}$$
(3.13)

where $P_3 \equiv \frac{sJ}{n_0\sigma} + \frac{1}{\tau\sigma}$. Thus,

$$r_{1/2} = \sqrt{-\ln(\frac{P_3}{2P_3 + f_0})2a^2} = \sqrt{2}a\sqrt{\ln(2 + \frac{f_0}{P_3})}$$
 (3.14)

The pillar diameter d is $2r_{1/2}$, which can be expressed in the beam current I as

$$d = 2\sqrt{2}a\sqrt{\ln(2 + \frac{I}{P_2})} \tag{3.15}$$

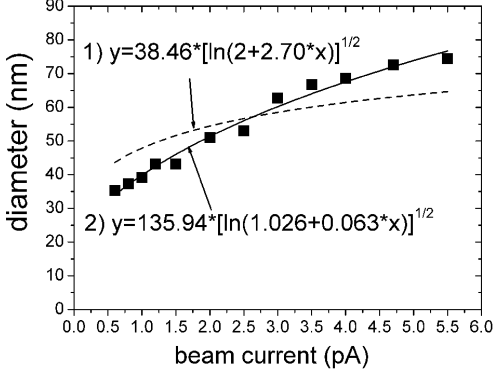


Figure 3.15: Experimental diameter of He⁺ IBID pillars grown with different beam currents and same doses, and the fitting curve neglecting diffusion. The error bar of the data is shown in Fig. 3.10.

However, it is not possible to fit the experimental data using Eq. 3.15 (see the dashed fitting curve 1 in Fig. 3.15). From the prefactor of curve 1 it follows that a should be about 15 nm, or FWHM_B is 35 nm, which is much larger than the subnanometer helium beam used in our experiments [41], as was checked independently by imaging. For a high-aspect-ratio pillar, the diffusion contribution to the vertical growth rate is inversely proportional to the pillar height. However, the diffusion from the substrate surface is expected to have a larger impact on the lateral growth. Therefore, we also performed the calculations for diffusion replenishment. According to Eq. 3.7, $\tilde{\varphi} \approx \log_2(2 + \tilde{\rho}^{-2})^{1/2}$, where the dimensionless ratio $\tilde{\rho}$ is $2\rho_{in}/\text{FWHM}_B$. Thus, ρ_{in} is the diffusion distance during the typical residence time of the molecules in the center of the beam $\rho_{in} = (D \tau_{in})^{1/2}$, $\tau_{in} = 1/(\text{sJ/n_0} + 1/\tau + \sigma f_0)$. In our case, FWHM_B=1 nm

$$\tilde{\varphi} = \frac{\sqrt{ln(2 + (\frac{2\sqrt{D\tau_{in}}}{FWHM_B})^{-2})}}{\sqrt{ln2}}$$
(3.16)

$$\tilde{\varphi} = \frac{\sqrt{\ln(2 + (\frac{1}{2\sqrt{D_{\frac{sJ}{n_0} + \frac{1}{\tau} + \sigma f_0}}})^2)}}{\sqrt{\ln 2}}$$
(3.17)

$$\tilde{\varphi} = \frac{\sqrt{\ln(2 + (\frac{\sigma}{4D})(P_3 + \frac{I}{2a^2\pi e}))}}{\sqrt{\ln 2}}$$
(3.18)

$$\tilde{\varphi} = \frac{\sqrt{\ln(2 + \frac{\sigma}{4D}P_3 + \frac{\sigma}{4D2a^2\pi e}I)}}{\sqrt{\ln 2}}$$
(3.19)

If we define constants $P_4=(2+P_3\frac{\sigma}{4D}),\ P_5=\frac{\sigma}{4D2a^2\pi e}$ we have

$$\tilde{\varphi} = \frac{\sqrt{\ln(P_4 + P_5 I)}}{\sqrt{\ln 2}} \tag{3.20}$$

the pillar diameter is proportional to $\tilde{\varphi}$, we define another constant P₆

$$D = P_6 \sqrt{ln(P_4 + P_5 I)} \tag{3.21}$$

It seems that the experimental measured pillar diameter can be fitted well with Eq.3.21 as shown by curve (2) in Fig. 3.15. However, it is not correct because the constant P_4 must be ≥ 2 . Therefore, this fitting does not work either. The failure can be caused by the assumption of the model: the distribution of secondary particles is the same as that of the primary beam which is only the case for a very broad beam (see Fig. 3.13). It is not applicable for sub-nanometer He⁺ beam. As discussed, the contribution of secondary particles dominates in the lateral growth, whereas the vertical growth depends mainly on the primary beam. Therefore the assumption might not be justified for calculating the lateral growth, but it is useful for calculating the vertical growth. Nevertheless, this continuum model based on precursor depletion and replenishment can qualitatively predict EBID and IBID growth with a clear message: the vertical growth rate and the resolution both increase with reduced depletion and / or enhanced replenishment. This is helpful to optimize the conditions for 3D structure growth. To expand this continuum model to narrow beams and high-aspect-ratio structures, simulation of the spatial distribution of the emitted secondary electrons from a non-flat surface is required. However, this remains a difficult task.

In summary, the study of process dependences not only gives us a better view of how to optimize the IBID conditions to grow high-aspect-ratio pillars, but also allows us to gain deeper understanding of the physical mechanisms of IBID pillar growth.

3.5 Formation of rough sidewalls and halos by Ga⁺ IBID

This section will describe how irregular sidewall surfaces and halos form on substrates of a typical Ga^+ IBID pillar. The influence of substrate (surface) conductivity is studied by comparing pillars grown on different substrates, either a conducting bulk Si or an insulating Si_3N_4 membrane.

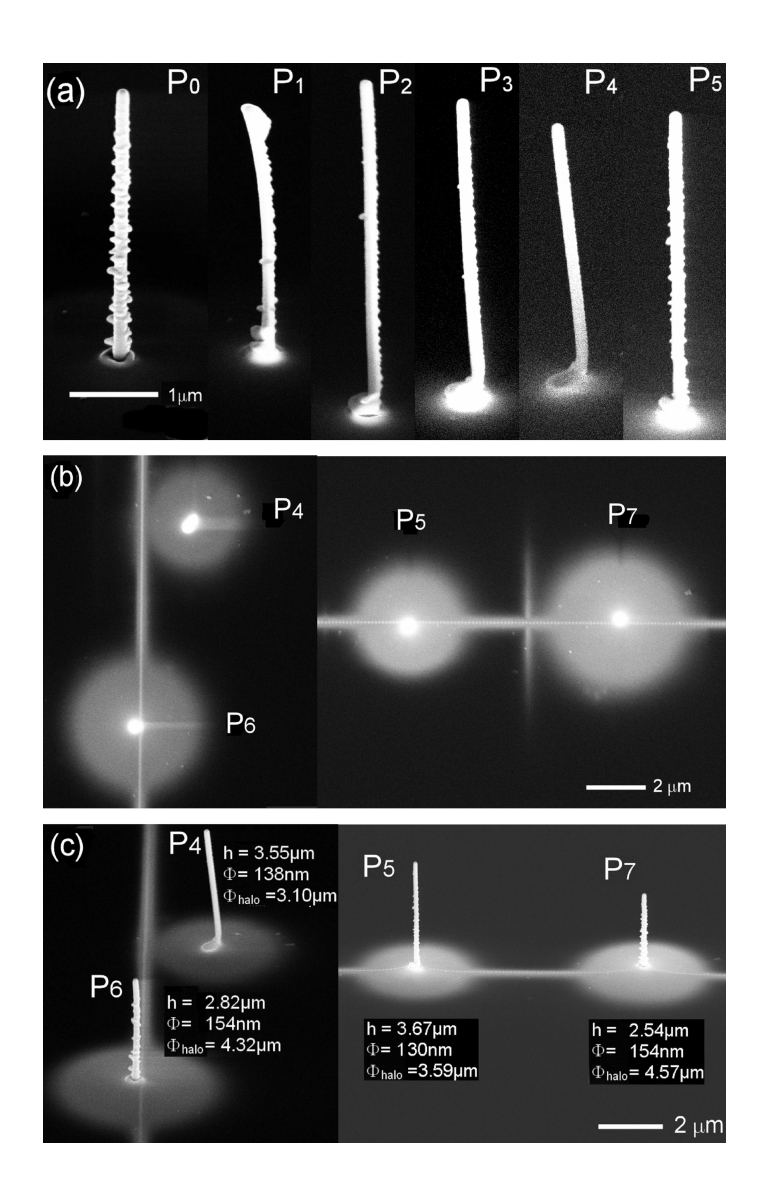


Figure 3.16: (a) Tilted (59°) SEM views of $\mathrm{Ga^+}$ IBID pillars $\mathrm{P_0}$ (on the conducting bulk Si) and $\mathrm{P_1}$ to $\mathrm{P_5}$ (on the insulating $\mathrm{Si_3N_4}$ membrane); (b) SEM top views of pillars $\mathrm{P_4}$ to $\mathrm{P_7}$; (c) tilted SEM views of pillars $\mathrm{P_4}$ to $\mathrm{P_7}$.

3.5.1 Pillars grown on Si and Si_3N_4

Figure 3.2b shows an overview of a number of grown pillars. Pillar P_0 was grown on the bulk surface and pillars P_1 to P_5 at different locations on the Si_3N_4 membrane. To study the effect of conductivity at the growth site, two conductive Pt lines were laid down (Fig. 3.16), and subsequently, pillars P_6 and P_7 were grown. A similar series of pillars was grown near the lower left corner of the membrane.

The Pt pillars are about 0.13 μm wide and 3 μm high. Figure 3.16a shows irregular structures (protrusions) on the pillar sidewalls. These irregularities are most prominent in the pillar grown on the bulk (P₀) and weaker in the pillars farther away from the window edge. Pillars P₆ and P₇, grown next to the conductive Pt line have rougher sidewalls than P₄ and P₅ (Figs. 3.16b,c). Moreover, they are lower and wider, and have larger halos, but have approximately the same volume.

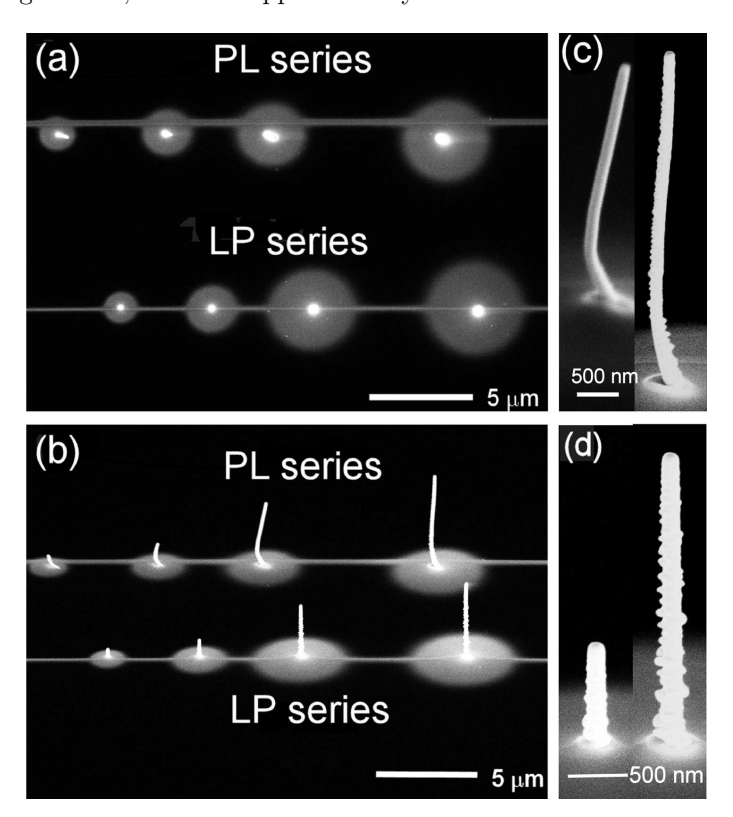


Figure 3.17: SEM images of the PL series (the Ga⁺ IBID pillars were deposited first, then the conductive Pt line) and the LP series (first the conductive Pt line, then the pillars): (a) top view; (b) tilted (59^o) view; details of (c) the PL series (180 s, 270 s) and (d) the LP series (60 s, 180 s). (The insulating Si₃N₄ membrane edge is $20 \mu m$ to the left.)

To investigate the processes of halo formation and sidewall roughening, four pillars (PL series) were grown at the left side of the insulating Si_3N_4 membrane for differ-

ent exposure times: 30, 60, 180 and 270 s. Subsequently, a conductive Pt line was grown nearby. Then, a second line followed by a similar set of pillars (LP series) was grown. One sees that the pillars grown on the isolated base (PL series) are smoother, thinner, and higher, and have smaller halos than those grown after the accompanying conductive Pt line (LP series) (Figs. 3.17a,b). By comparing the short pillars to the corresponding lower part of the longer pillars in Figs 3.17c and d, one sees that the surface irregularities grow with deposition time. There is a linear relationship between the pillar height and the halo area (Fig. 3.18). Moreover, the growth rate is almost constant, although the PL series grew 25% faster than the LP series.

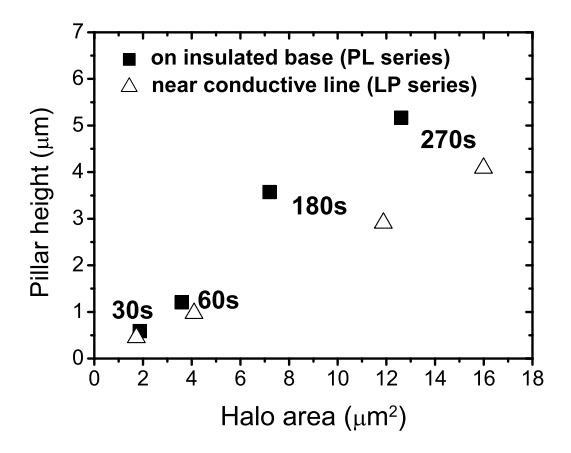


Figure 3.18: Relationship between Ga⁺ IBID pillar height and halo area for LP and PL series which have different exposure times and sites.

The shown pillars are always rougher at the side that faces the insulating Si_3N_4 membrane edge (P_1 to P_5 in Fig. 3.16 and PL in Fig. 3.17). This was also observed for many other pillars grown at many other locations on the membrane. Moreover, the pillars always bend towards the center of the membrane. Furthermore, all halos, including those of the bent pillars, are circles with their centers at the starting point of the vertical growth.

3.5.2 Discussion

As discussed in Chapter 1, possible operative mechanisms in IBID [222] are depositions by (1) primary ions (2) sputtered atoms or ions and (3) secondary electrons. One or more of these mechanisms can cause the formation of the halos and irregular sidewalls. We think that the charging effects observed in this study provide a clue. For IBID pillar growth, the primary ion reflection is mainly due to atomic collisions at the top of the pillar. Considering the energy and mass of Ga⁺ primary ions, it is unlikely that they can be affected markedly by charging. Furthermore, if deflected

primary ions formed the halo, simple geometric considerations suggest that the halo diameter is proportional to the pillar height, not its area (as observed in Fig. 3.18). As discussed in Chapter 1, according to the kinetic gas theory, the scattering mean free path (MFP) of (CH₃)₃Pt(C_PCH₃) precursor molecules at room temperature is roughly 1-10 mm. For such a large MFP, one does not expect a large scattering of primary ions when they pass through precursor molecules in the gas phase. Moreover, the scattering of primary ions can be ruled out in any case because it is not affected by charging. Also, the sputtered particles can be ruled out because most are neutral [135, 167, 232] and therefore not affected by charging. The typical energy range of ion-induced secondary electrons is from 0 to 20 eV, and the typical yield ranges from around 1 to 10 electrons per ion [135, 167, 170, 171, 233]. Moreover, secondary electron emission is very sensitive to surface charging [234–236].

We propose the following mechanism. The pillar becomes positively charged by the incident positive primary ions and the emission of secondary electrons. Owing to the capture of some secondary electrons, the surrounding insulating membrane becomes negatively charged with respect to the pillar. As only a portion of the secondary electrons arrive at the substrate, the charge on the pillar is greater than that on the substrate. Therefore, the entire system of pillar plus substrate is positively charged. Because the pillar is conductive and the current is small, the electrical potential is uniform over the pillar. Owing to the attraction by the negatively charged substrate, the positive charge on the pillar surface is concentrated at the bottom. Furthermore, one expects charge accumulation at the sharp corners of the pillar.

Calculations using the finite element analysis software COMSOL Multiphysics give more insight into the details of pillar charging. The calculated charge density for a pillar potential of 1 kV is shown in Fig. 3.19a. The charge density is relatively high at the bottom of the pillar and decreases rapidly with height. Moreover, the charge density at the corner of the top of the pillar is higher than that at the central area of the top. The total charge on the pillar is +0.077 pC and that on the membrane is -0.04 pC. We observed that the measured sample current stabilized a few seconds after the start of the pillar growth, corresponding to a few pC of ion charge. Thus, either there is a significant leakage current or the pillar potential is considerably greater than 1 kV. The actual potential of the pillar is unknown, but we consider that a much higher potential is not reached during growth. A high electric potential on the pillar would strongly affect the focus and direction of the primary beam. Okada and coworkers reported that with ion beam energy decreasing from 30 to 5 keV, the growth rate of IBID pillars increases by as much as 30 times, whereas the diameter increases by a factor of 3 [112]. Furthermore, the sidewall becomes more irregular. We did not observe any of these effects in the present experiments, which indicates that the incident energy of the primary ions is not far below 30 kV. Therefore, we conclude that the effect of charging on the pillar potential is limited to one or a few kV at most.

We hypothesize that the accumulated negative charge on the substrate repels newly arrived secondary electrons (see the sketch in Fig. 3.20a). In contrast, if the surface is conductive, the captured secondary electrons flow away to the ground (Fig. 3.20b). Therefore, more secondary electrons can arrive at the substrate surface,

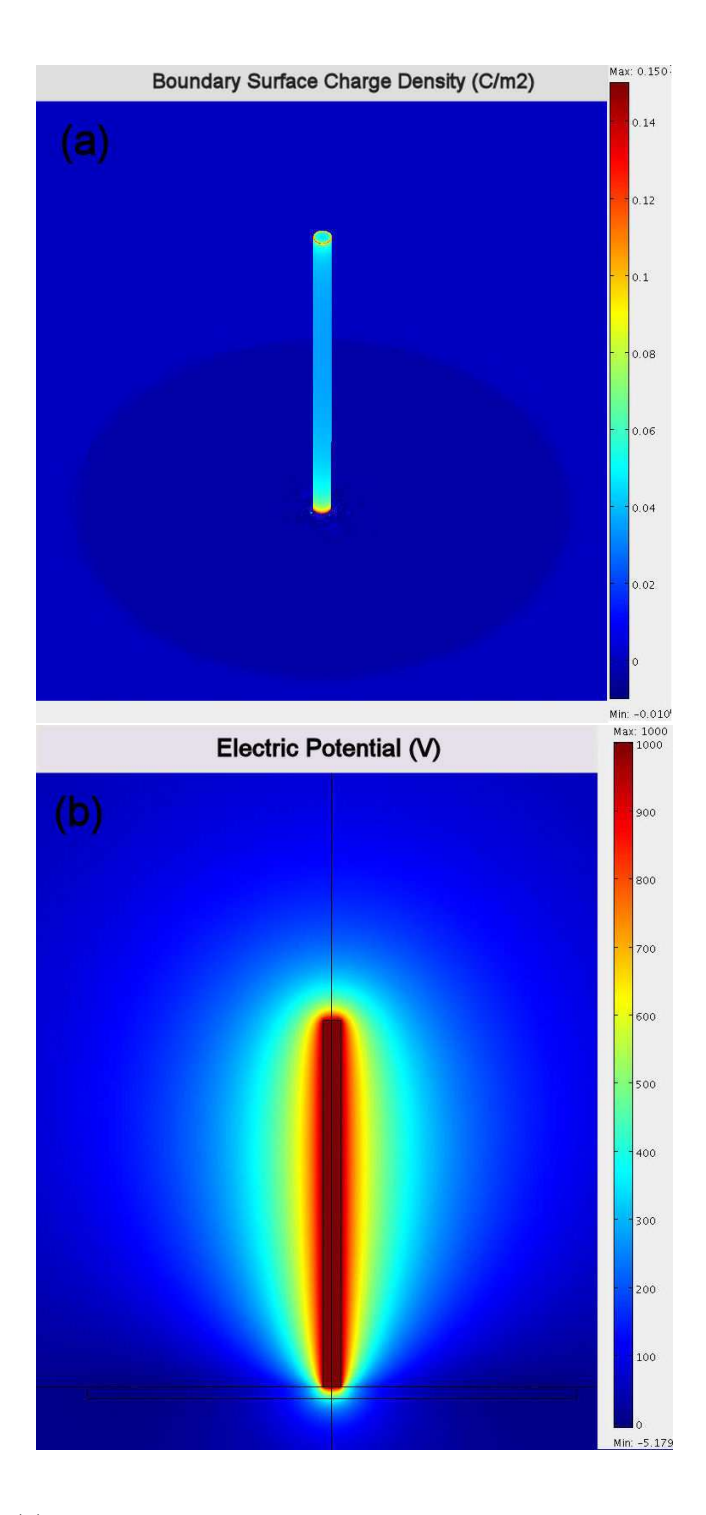


Figure 3.19: (a) Calculated surface charge density for a pillar grown on an insulating $\mathrm{Si_3N_4}$ membrane with a potential of 1 kV. The height and the diameter of the pillar are 3 $\mu\mathrm{m}$ and 150 nm, respectively. The diameter of the halo region is 2 $\mu\mathrm{m}$. (b) Calculated electric potentials on the pillar and surrounding area.

leading to a more intense halo. The unequal charge density on the equipotential surface of the pillars on the insulating membrane affects the electron emission characteristics. Secondary electrons are preferably emitted from the central area of the top of the pillar, where the positive charge density is lowest and thus the surface energy barrier is lowest. Simultaneously, fewer electrons are emitted from the corner of the top of the pillar and its sidewall. Thus, the pillars on an insulating substrate grow faster in height and slower in width. Moreover, these pillars remain smoother because fewer secondary electrons are emitted from the sidewalls, let alone from any hypothetically charged sidewall protrusions.

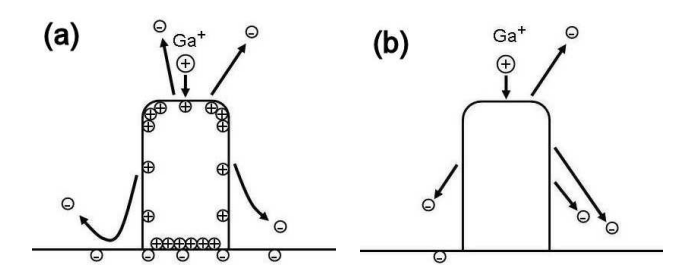


Figure 3.20: Sketches of secondary electron emissions during IBID pillar growth on (a) insulating (b) conducting substrates.

However, we cannot rule out the effect of the charged surface on the movement of the polarized or charged precursor gas molecules or their fragments. It is worth noting that carbon dendrite-like or filament-like structures were formed on insulators by electron irradiation under relatively poor vacuum conditions [237–239]. Similarly, tungsten dendrite-like structures were fabricated on insulators with tungsten hexacarbonyl W(CO)₆ as a precursor [240, 241]. On a charged surface, the diffusive random movement of molecules does not occur [237]. The formation of these dendrite-like structures is attributed instead to the oriented aggregation of ionized or polarized molecules in a local electrical field, caused by the charging of the insulator surface [237–241]. One might also attribute the observed differences in pillar shape in our work to the differences in the aggregation of the precursor gas molecules. Polarized gas molecules aggregate at locations where the field strength is highest, for instance at the top of the pillar (Fig. 3.19b), instead on the sidewall and the substrate surface. Hence the pillar sidewall becomes smooth and the halo becomes smaller. Owing to the complexity of the process involved, further study is required to confirm or reject this possible mechanism.

Furthermore, we consider that the irregularity of the sidewall cannot be explained by heating [217, 218, 221] because the heat is more slowly dispersed in the isolated membrane than in the bulk Si. The asymmetric sidewall roughness and pillar bending we observed are probably related to the nonhomogeneous charge distribution on the membrane. Note that the circular shape of the halos of the bent pillars rules out FIB drift and sample sliding as causes for the bending. Instead we suggest that the bending is caused by the attraction between the positively charged pillar and the neg-

atively charged membrane. The bending of EBID pillars was observed previously by Mitsuishi and coworkers and also explained in terms of electrostatic attraction [225]. The initial deposition at the pillar base is possibly caused by a temporary FIB drift during the initial charge buildup (see P_2 to P_5 in Fig. 3.16a and PL in Fig. 3.17).

3.6 Proximity effect in IBID of pillars

This section will present the proximity effect of pillar growth by Ga⁺ or He⁺ on different substrates having different conductivity.

3.6.1 Proximity effect in Ga⁺ IBID of pillars

Influence of the direction of the precursor gas flow

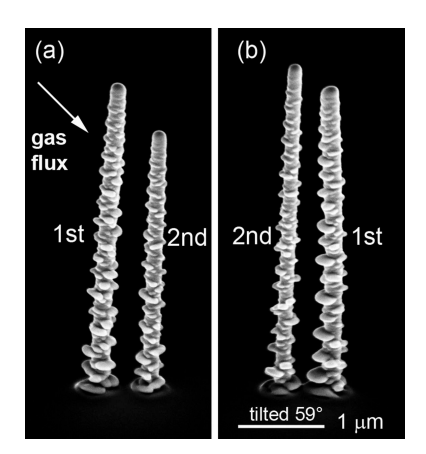


Figure 3.21: Shadowing effect in Ga⁺ IBID pillar growth. Tilted (59°) SEM images of two pairs of pillars which are grown in different orders (nozzle is located at the left side) on conducting bulk Si: the second pillar is grown (a) at the left side of the first pillar; (b) at the right side of the first pillar.

To investigate the influence of the direction of precursor gas flow, we compared two pairs of pillars grown on a conducting bulk Si. One pair was grown from left to right, the other from right to left (Fig. 3.21a,b). The second pillar in Fig. 3.21a is shorter. It was probably shadowed from the precursor gas flow by the existing pillar. To avoid this known shadowing effect [88], the order of growth is always from right to left in the images of Figs 3.22, 3.24, and 3.25.

Pairs of pillars grown on Si at different separations

Figure 3.22a shows pairs of pillars which were grown on conducting bulk Si with different separations. A single pillar is shown for comparison. As a consequence of the growth of the second pillar, the first pillar becomes broader and rougher, and bends slightly toward the second one for separations less than 1.4 μ m. Moreover, the second pillar is taller than the first one. Not surprisingly, the additional length varies with the separation (Fig. 3.23). However, the height of the first pillar and the diameter of the second pillar are unaffected as compared to a single pillar. No proximity effect has been observed when pillars are 3.0 μ m apart. The halo regions of the pillars are visible in the corresponding top views (Fig. 3.22b). Note that if the halo of the second pillar does not extend to the irradiation point of the first pillar, no proximity effect is visible.

Pairs of pillars grown on Si₃N₄ at different separations

Figure 3.24a shows pairs of pillars grown on the insulating $\mathrm{Si}_3\mathrm{N}_4$ membrane. In contrast to the pillars on conducting bulk Si , the first pillar broadens only slightly and does not bend towards, but away from the second pillar. Surprisingly, the second pillar is shorter and rougher. Furthermore, its shape is twisted: first, it bends away from the first pillar, and then towards it. In addition, as can been seen in Figure 3.24b, the bases of the neighboring pillars are very different: the first pillar has a twisted base whereas the second one does not. Finally, this proximity effect is still visible at 7.0 μ m separation. Even when the halo regions of two neighboring pillars do not overlap, the proximity effect is still pronounced.

Role of substrate conductivity in the proximity effect

The proximity effect on a Si wafer coated with 30 nm Cu is very similar to that on a bare Si wafer (Fig. 3.25a). Contrary to Mitsuishi's observation for EBID pillars [225], the bending of the first pillar remains unaffected with increasing substrate conductivity. On the same Si_3N_4 membrane of Figure 3.24, two pillars were deposited 7.0 μ m apart near a Pt line, which connects the Si_3N_4 window to the conducting bulk Si surface. In contrast to the pillars grown on the bare Si_3N_4 surface, no proximity effect is visible (Fig. 3.25b). Figure 3.25c compares a pillar on Si, a pillar pair on Si, a pair on bare Si_3N_4 and a single pillar on Si_3N_4 with a conductive Pt line. The heights of the pillars are similar, apart from the second pillar on Si and the first pillar on bare Si_3N_4 .

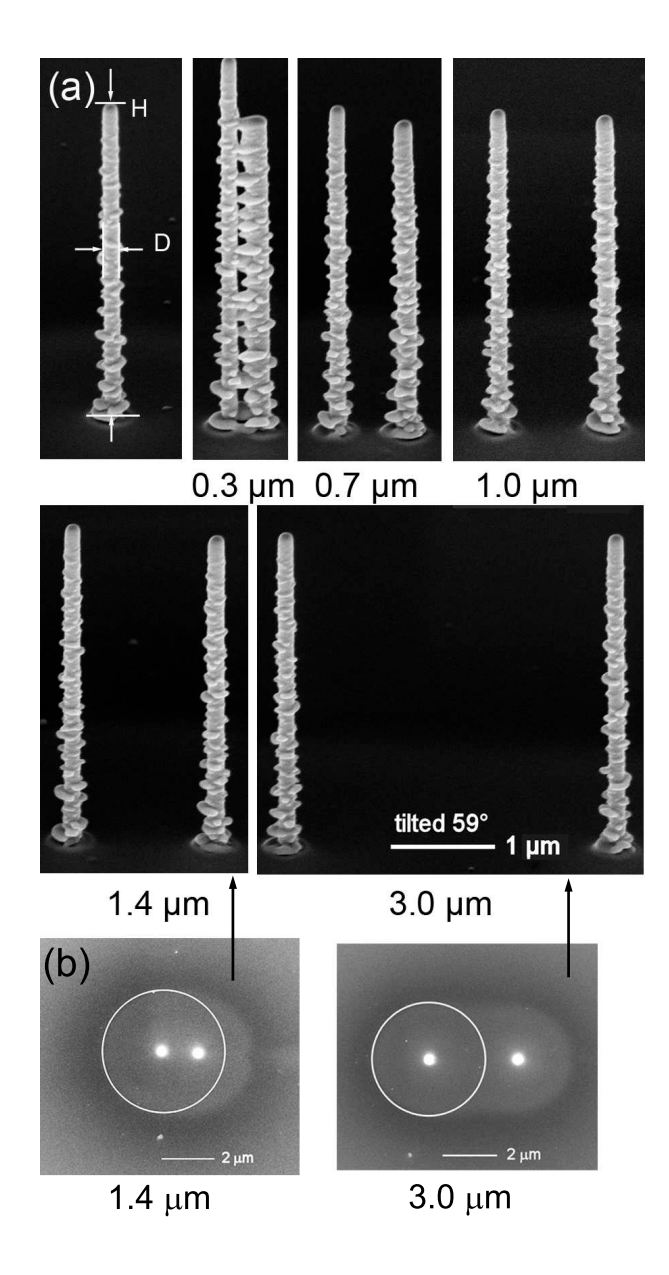


Figure 3.22: Proximity effect of Ga⁺ IBID pillars grown on conducting bulk Si. (a) Tilted (59°)SEM images of a single pillar and of five pairs of pillars with different separations from 0.3 μ m to 3.0 μ m; (b) top views of two pairs of pillars with separations 1.4 μ m and 3.0 μ m

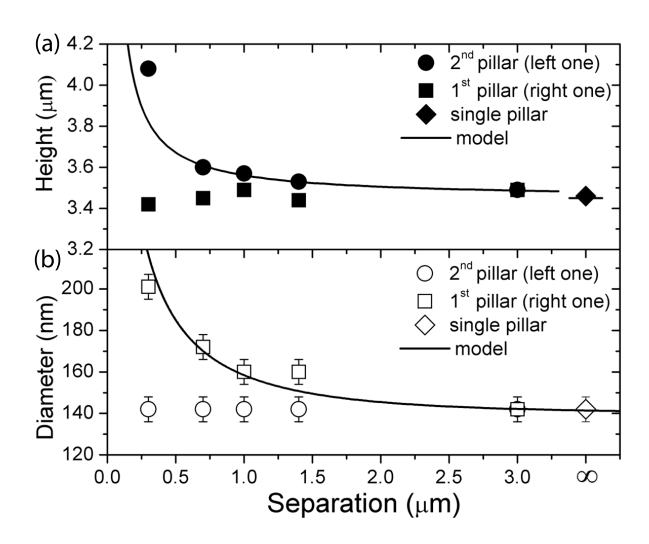


Figure 3.23: Proximity effect of Ga⁺ IBID pillars grown on conducting bulk Si. Relationship between diameter, height and separation of pillars shown in Fig. 3.22; the points are experimental data and the curves are the values calculated by using the models discussed in the text of Section 3.6.3.

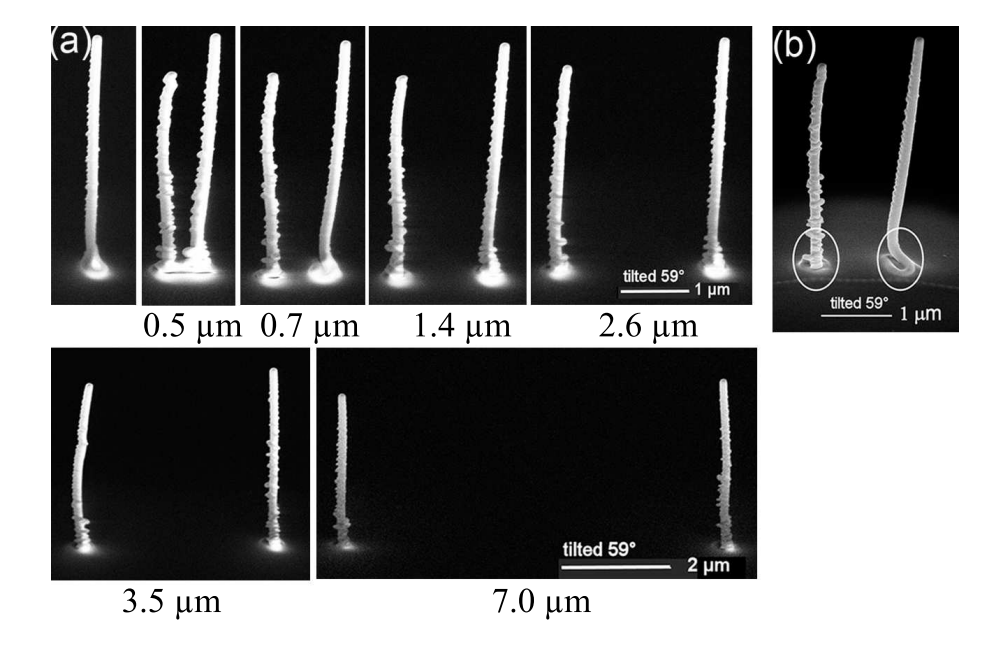


Figure 3.24: Proximity effect of Ga⁺ IBID pillars grown on a 45-nm-thick insulating Si₃N₄ membrane. Tilted (59°) SEM images of (a) six pairs of pillars with different separations from 0.5 μ m up to 7.0 μ m; (b) different pillar bases.

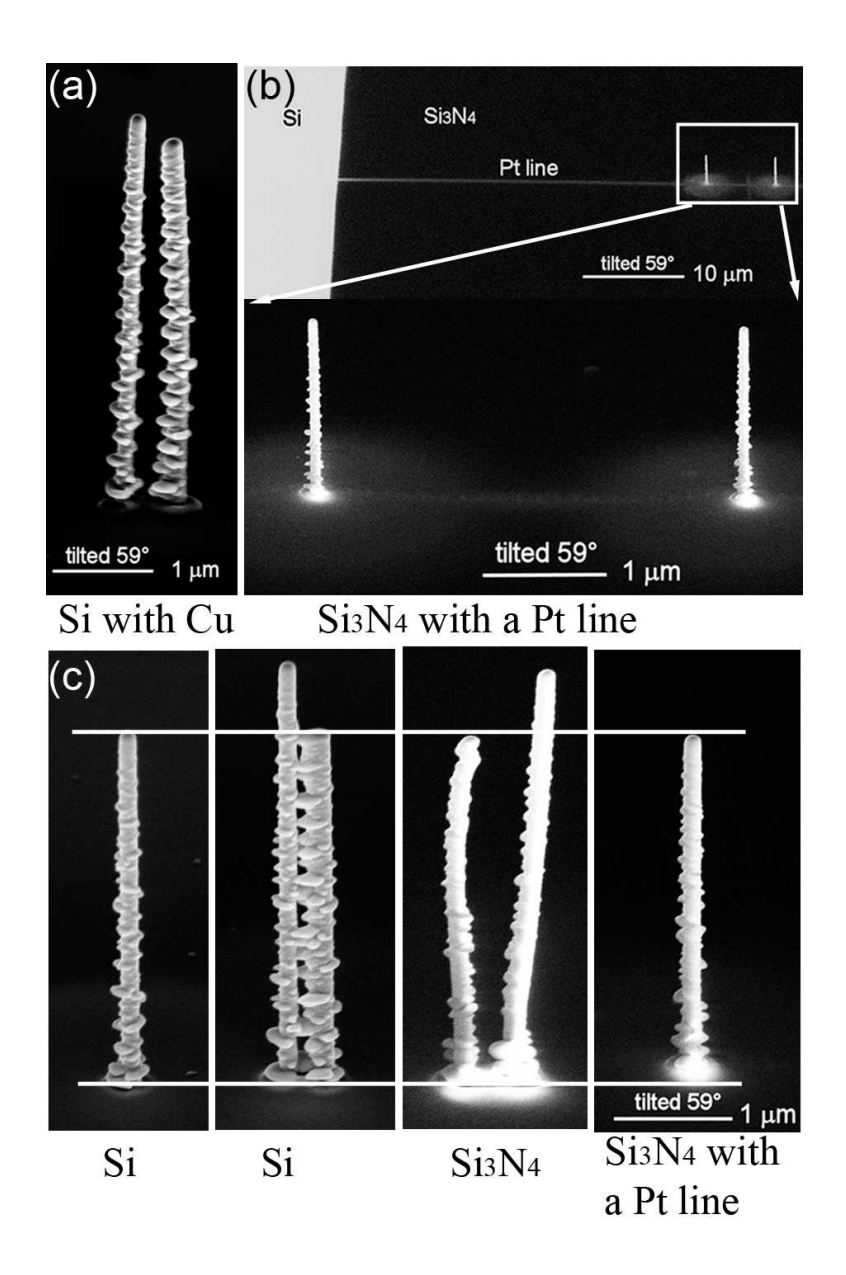


Figure 3.25: Role of substrate conductivity in the proximity effect of Ga^+ IBID pillar growth. Tilted $(59^o)SEM$ images of (a) one pair of pillars grown on Cu-coated conductive bulk Si; (b) one pair of pillars grown on insulating Si_3N_4 membrane with a conductive Pt line; (c) pillars grown on Si without or with a neighboring pillar, and on Si_3N_4 membrane with a neighboring pillar or a conductive Pt line.

3.6.2 Proximity effect in He⁺ IBID of pillars

Nanopillars with different exposure times grown on Si at different separations

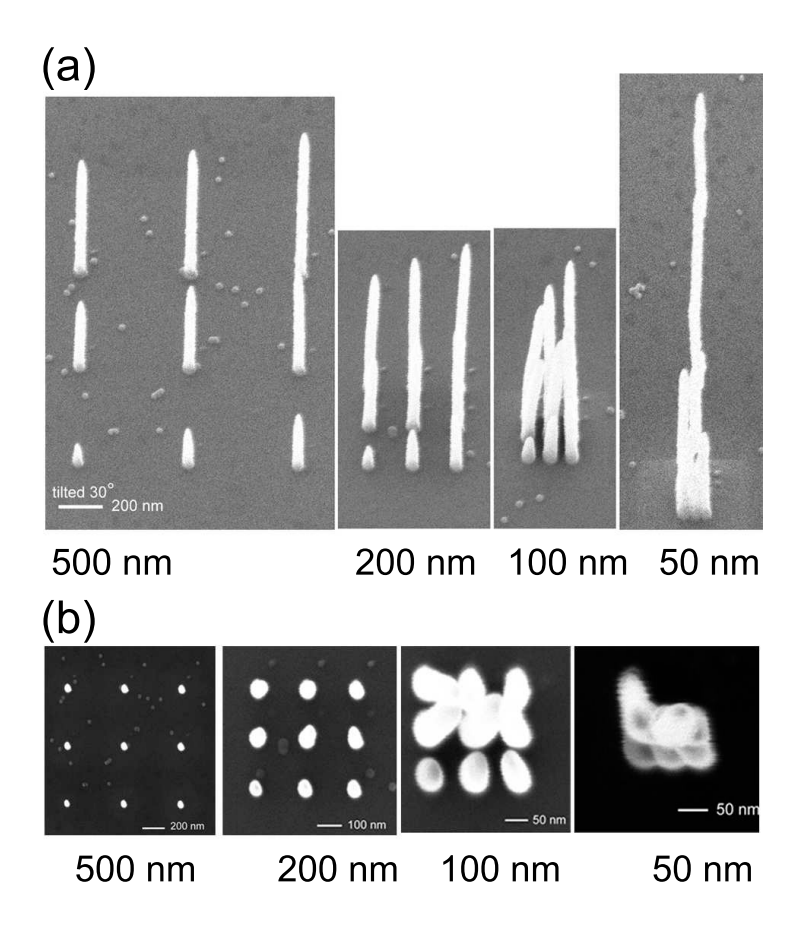


Figure 3.26: Proximity effect of $\mathrm{He^+}$ IBID pillars. a) Tilted (30°) helium ion microscopy (HIM) views and (b) top views of pillars grown on conducting bulk Si in spot mode, with exposure time from 1 s to 9 s, and different separations from 500 nm to 50 nm.

Helium ion microscopy (HIM) images of the deposits by He⁺ IBID with different exposure times and different separations are shown in Fig. 3.26. The diameters and the heights are shown in Fig. 3.27. Only cones are grown for 1 s exposure time. For exposure times of 2 s and longer, pillars are formed. These are cylinders with conical tops, all of which are 240 nm tall. For pillar separations above 100 nm, the height increases almost linearly with exposure time. In contrast, the diameter increases until it stabilizes at about 50 nm. No proximity effect is observable for separations larger than or equal to 500 nm. (The pillars at 1000 nm separation are not shown.) Also, for pillars separated by 200 nm, one sees no differences in the diameter and

height, although some pillars bend slightly towards to the pillar that was grown next. For a separation of 100 nm, a proximity effect is clearly visible: pillars are thicker, slightly taller, and bent. The pillars at 50 nm separation have merged. The last two pillars were actually grown on top of the pillar grown for an exposure time 7 s.

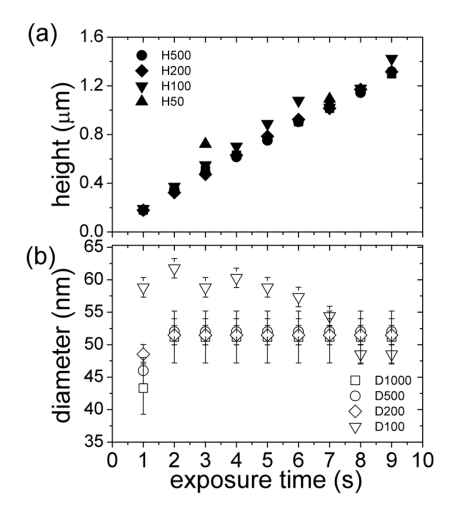


Figure 3.27: Exposure time dependence and proximity effect of He⁺ IBID pillar growth. (a) Diameter (b) height of pillars shown in Fig. 3.26.

3.6.3 Discussion

IBID results from the interaction of ions with precursor gas molecules adsorbed on a substrate surface. The shape and dimension of IBID structures are determined by (a) scattering of primary and secondary particles, (b) precursor coverage and (c) substrate surface conditions. We discuss the proximity effect in IBID pillar growth in terms of these factors.

Effect of scattered particles

Possible operative mechanisms in IBID are decompositions of adsorbed molecules by (1) primary ions (2) sputtered atoms or ions and (3) secondary electrons [222]. One or more types of particles can contribute to IBID. In previous work, we have observed significant deposition outside the irradiated area during IBID [188].

During the growth of the second pillar, some scattered primary ions as well as emitted secondary electrons and atoms can arrive at the neighboring, previously grown pillar. These particles induce additional deposition on the first pillar, resulting in a broadening (Fig. 3.22a and 3.24a). A similar broadening of the first pillar was

observed in EBID pillar growth [216, 224, 225]. For a smaller pillar separation, a larger fraction of the scattered particles can arrive at the first pillar. Therefore, broadening scales roughly inversely with separation (Fig. 3.22a).

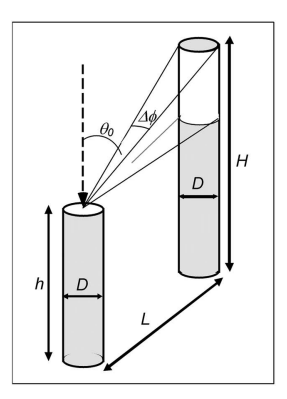


Figure 3.28: Proximity effect. Secondary particles are emitted from the growing second pillar (left). If the polar emission angle is between θ_0 and $\pi/2$ and if the azimuthal angle is within the shown range of $\Delta\phi(=D/L)$, the emitted particles arrive at the first pillar (right), causing additional growth in the white colored region.

The angular distribution of emitted secondary particles has an overcosine shape: $\frac{n+1}{2\pi}\cos^n\theta$, where θ is the emission angle as shown in Fig. 3.28, n = 1 for secondary electrons [178, 179] and 1 < n < 2 for sputtered atoms [242]. From this distribution plus geometric factors one can write the fraction of the secondary particles f_s emitted from the top of the growing pillar that arrives at the first pillar (Fig. 3.28) as

$$f_s = \int_{-D/2L}^{D/2L} \int_{\theta_0}^{\pi/2} \frac{n+1}{2\pi} \cos^n \theta \sin\theta d\theta d\varphi = \frac{D}{2\pi L} \cos^{n+1} \theta_0$$
 (3.22)

where $\theta_0 = \arctan(\frac{L}{H-h})$. The top of the pillar is dome-shaped. As the diameter of the emitting area is much smaller than the pillar diameter, convolution of Eq. 3.22 with the actual orientations of the emitting surface has only a marginal effect and, thus, can be disregarded. Hence, the number ΔN_s of secondary particles that arrive at the first pillar in a time interval Δt is:

$$\Delta N_s = Y \frac{i_P \Delta t}{e} \frac{D}{2\pi L} \cos^{n+1} \theta_0 \tag{3.23}$$

where Y is the total number of emitted secondary particles per incident ion, i_P is the primary ion current and e the elemental charge. We will denote by α the volume growth of the first pillar when it is hit by a secondary particle. The additional volume gain V_s of the first pillar during growth of the second pillar is then

$$V_s = \alpha Y \frac{i_P}{e} \frac{D}{2\pi L} \int \cos^{n+1}\theta_0 dt = \alpha Y \frac{i_P}{e} \frac{D}{2\pi L} \frac{1}{v} \int_0^H \cos^{n+1}\theta_0 dh$$
 (3.24)

where v is the vertical growth rate of the second pillar. The growth rate of the pillar volume is $\frac{1}{4}\pi D^2 v$. If we denote the volume change of the second pillar per incident ion by β , we have $\frac{i_P\beta}{e} = \frac{\pi D^2 v}{4}$. Hence, by substituting $\frac{i_P\beta}{ev}$ by $\frac{\pi D^2}{4\beta}$ Eq. 3.24 can be written as:

$$V_{s} = \frac{\alpha Y}{\beta} \frac{\pi D^{2}}{4} \frac{D}{2\pi} \frac{1}{L} \int_{0}^{H} \cos^{n+1} \theta_{0} dh \equiv \frac{\alpha Y}{\beta} \frac{D^{3}}{8} X(L/H)$$
 (3.25)

The dimensionless function X depends only on the ratio L/H and can be numerically evaluated. The curve in Fig. 3.23b shows the calculated width of the first pillar after growth of the second pillar according to Eq. 3.25 with n=1.5. We have used $\alpha Y/\beta$ as fitting parameter. The agreement between the experimental data and the calculation shows that the extra growth of the first pillar can be qualitatively described by a geometric model that is based on a $\cos^n \theta$ -like emission distribution. The ratio obtained between αY and β is 22 ± 3 . Calculations in the range 1 < n < 2 yield within 1% the same curve shown in Fig. 3.23b. Thus, when an ion hits a substrate covered by precursor molecules, the emitted secondary particles can in principle deposit 22 times more material in the proximity of the impact site than at the impact site itself. Of course, this can only happen when the nearby surfaces are properly oriented and fully covered by precursor molecules. This high number can be explained partly by suttering at impact site, which is absent in the proximity. Moreover, redeposition of sputtered atoms and of emitted precursor fragments probably contribute to this high number. Obviously, also precursor decomposition induced by these impinging particles and by secondary electrons is responsible for the large proximity effect. Assuming that the atomic density of the deposit is 100 atoms/nm³, β is 4.5 atoms/ion (Table 3.1). Secondary electron yield and secondary atom yield are 1.2 and 6, respectively (Fig. 5.5). If the secondary electron dominates in IBID, α is 82.5 or 16.5 for the cases that the secondary electron or the secondary atom dominates in IBID, respectively. They are surprisingly high numbers.

Precursor decomposition by heating first pillar during growth of the second one might also explain the broadening. As heating of the growing pillar itself is small -at most a few degrees- heating by conduction or radiation over a typical pillar separation 1 μ m or more should have no observable effect. Also the primary beam can induce additional growth of the first pillar. However, ions in the tail of the primary beam are expected to increase the first pillar height, not its diameter. Scattering of primary ions is mostly forward and therefore one would expect mainly broadening of the pillar base, not the entire pillar. We conclude that the proximity effect is largely caused by secondary particles.

Bending of our IBID pillars is not as great as that of EBID pillars [224, 225]. This difference is not surprising because both the Young's modulus and the width of IBID pillars are much higher than those of EBID pillars [111, 112]. The cause of the bending is still under debate. Unlike Kislov [224] and Mitsuishi [225], we did not observe a clear relationship between pillar bending and substrate conductivity. However, both in our work and in [224] and [225], pillar broadening is always accompanied by bending. An explanation of the bending is the deformation caused by the

uneven stress on the first pillar surface due to the additional deposition at one side of the pillar. Considering its unaffected width, it is unlikely that the increased height of the second pillar on Si or Cu-coated Si is caused by scattered particles. There must be a different mechanism at work.

Similarly, the effect of scattered particles also causes the existing He⁺ IBID pillars to broaden and to bend towards to the newly grown pillars, as can be seen in Figs. 3.26 and 3.27. Besides this similarity, the broadening of He⁺ IBID pillars is less than Ga⁺ IBID pillars, whereas the bending is more pronounced. This can be explained by the scattering of 25 keV He⁺ beam, which is much smaller than that of 30 keV Ga⁺, and by the fact that the He⁺ IBID pillar is 4 times narrower, respectively.

Effect of precursor coverage

The deposition rate of IBID depends strongly on the precursor gas coverage of the substrate surface. As observed, the deposition rate is high when a scanning ion [243] or electron [244] beam is moved towards the nozzle. Obviously, the precursor coverage depends on the orientation of the surface with respect to the precursor gas flow. If the surface of a growing structure is not fully exposed to the precursor flux, shadowing occurs: the deposited volume under shadowing is smaller. For high deposits, such as pillars, shadowing is almost inevitable (Fig. 3.21a). It is important to note that the proximity effect still exists when shadowing is absent (Fig. 3.21b and Fig. 3.22a). This proximity effect will be explained below.

From the ratio between the diameter of the nozzle and of the pump inlet, we estimate that the local pressure at the outlet of the nozzle is in the range of 10^{-2} 10⁻³ mbar. According to the kinetic gas theory, the corresponding mean free path of (CH₃)₃Pt(C_PCH₃) precursor molecules at room temperature is roughly 1-10 mm (see Section 1.3.2). The deposition site was 450 μ m from the outlet. Therefore, most molecules do not encounter a gas phase collision before impinging the surface. Some molecules that imping the existing first pillar are reflected. Others are adsorbed first and then desorbed. These re-entering molecules contribute to the local pressure of the precursor gas near the growing pillar. Assuming uniform reflection and desorption intensities and neglecting dependencies on the polar angle θ , the fraction of molecules that leave the first pillar and reach the growing one is approximately $\Delta\Phi/2\pi$ $D/2\pi L$. The extra flux of these molecules can enhance the precursor coverage on the growing pillar, thus increasing the growth speed. The curve in Fig. 3.23a is a fit of $\gamma D/2\pi L$, where γ being a fitting parameter. Agreement is found for $\gamma =$ 1.45. Because this value is relatively large -even larger than unity- we conclude that reflection or desorption of precursor molecules constitute a secondary flux that can have a substantial influence on the growth rate of the growing pillar.

The surface diffusion is short-ranged (<100 nm) [244]. Therefore, we conclude that molecules diffusing between the pillars across the substrate surface play a minor role in the precursor coverage enhancement of the growing second pillar. Neverthe-

less, an accurate estimation of the contributions of all these effects -molecule direct impingement and reflection, adsorption, desorption, and diffusion- requires further study [244].

The effect of the precursor coverage can also explain why the second He⁺ IBID pillars become slightly taller.

Effect of charging

The similarity between pillars grown on bare Si and on Cu-coated Si indicates that the conductivity of Si is sufficient to carry away the surface charges during IBID. However, the charging situation on Si₃N₄ is very different. During IBID pillar growth, the growing pillar is positively charged due to the impingement of positive ions and the emission of secondary electrons [209]. The insulating substrate, however, captures electrons that are emitted from the pillar or released in the inevitable ion-gas phase collisions. Therefore, the substrate is negatively charged with respect to the pillar. The unequal charge distribution on the equipotential surface of the conductive pillars affects the secondary electron emission [209]. Secondary electrons are preferably emitted from the central area of the top of the pillar, where the positive charge density and, thus, the surface energy barrier are lowest. As fewer electrons are emitted from the sidewall, the pillars on an insulating substrate grow faster in height and slower in width [209]. Moreover, the base of a pillar grown under charging conditions has a complex shape, which is possibly caused by a temporary FIB drift during the initial charge buildup [209]. As the growing pillar on Si₃N₄ is positively charged, some emitted secondary electrons are attracted back to the pillar and fewer arrive at the nearby first pillar. This sensitivity to charging suggests that the secondary electrons play an important role in the additional growth nearby. It explains why the broadening of the first pillar is much less on Si₃N₄ than on Si. Moreover, the charging effect can also explain the twisted shape of neighboring pillars on Si₃N₄. At the beginning of growth, both pillars have the same charge but repulsion force bends them apart. In the upper half of the pillar, the bending direction is reversed, possibly because the initial bending of the pillar resulted in the end of the pillar shifting under the fixed ion beam, so the deposition shifted to the side closest to the first pillar.

The clearly different base shapes, heights and surface roughness of two neighboring pillars indicate that the surface charging was reduced due to the presence of the first pillar (Fig. 3.24b). We conclude that the second pillar becomes shorter and rougher because there was less charging (Fig. 3.24a). The effect of charging on IBID pillar growth can also be seen in Fig. 3.25c: not only another pillar but also a nearby Pt line can reduce charging during growth considerably.

The reduced charging suggests that transport of electrons between two neighboring pillars takes place. The chance that electrons flow through the insulating Si_3N_4 membrane is very small. However, they can travel through the vacuum from the first pillar to the growing one. We note that IBID pillars can work as field emitters [123,

128]. Alternatively, for insulators with secondary electron emission coefficients greater than unity, a succession of electron collisions can result, in effect, in electrons skipping across the surface [245].

3.7 Conclusions

This chapter discusses the study of a detailed optimization of growth conditions of Ga⁺ and He⁺ IBID, which are required to fabricate nanopillars in a controllable and reproducible manner. Deposition depends on the densities of the precursor molecule and the ions in the irradiated area. The situation of the depletion and replenishment of the precursor molecule in the irradiated area determines the morphology of the IBID pillar. According to the continuum model proposed by Utke [88, 183] and a 3D Monte Carlo simulation work by Smith et al. [207], the general conclusion is that a higher vertical growth rate and better resolution of the IBID pillar can be achieved with better replenishment or less depletion of the precursor. Our experimental results provide the evidence that the vertical growth rate and the resolution indeed increase with better replenishment by increasing local precursor pressure, decreasing substrate temperature, or increasing ion beam refreshment time. Alternatively, the vertical growth rate and the resolution increase due to less depletion by decreasing the ion beam dwell time or decreasing the ion beam current. In the case of Ga⁺ IBID pillars, the smallest width of about 140 nm has been achieved and a vertical growth speed of about 20 nm/s. Compared to Ga⁺ IBID pillars, He⁺ IBID pillars have similar deposition yields, but a vertical growth rate that is 10 times higher. Furthermore, the He⁺ IBID pillars are about 3 to 4 times narrower. In conclusion, helium ion microscopy (HIM) offers a more promising alternative technology for direct fabrication of 3D nanostructures.

Furthermore, the formation of irregular sidewalls and halos in Ga⁺ IBID has been investigated by comparing pillars grown on conductive and insulating substrates. Less irregular sidewalls and smaller halos have been observed on the insulating substrates where charging is supposed to happen. The analysis of the observed sensitivity to local charging shows that there are two factors involved in IBID that can be influenced by the surface charging: secondary electron emission and aggregation of polarized or charged precursor molecules. It leads to two explanations for the formation of the irregular sidewalls: either it is caused by the deposition induced by secondary electrons emitted from the growing structures or by the non-perfect smooth surface due to the sputtering process. The latter one seems more likely considering He⁺ IBID and EBID pillars are smooth where the sputtering is negligible. The halos are caused by the scattering secondary particles from the growing pillar. Nevertheless, this study suggests a new method to prevent the irregular sidewalls of Ga⁺ IBID structures via the application of a local electric field near the irradiation point.

Finally, the proximity effects in Ga⁺ IBID of nanopillars grown on conducting bulk Si and on an insulating Si₃N₄ membrane have been discussed. When two pillars are grown next to each other with a separation of hundreds of nanometers or a few micrometers, the diameter, height, and shape of the first grown pillar are affected as well as these properties of the second pillar. I conclude that the changes of the first grown pillar are caused by the additional deposition induced by the scattering of secondary particles from the growing second pillar. Deposition by secondary particles in the proximity of the ion beam impact site can significantly exceed the deposition at the impact site itself. The changes of the second pillar on Si result from the enhancement of its precursor gas coverage, whereas on $\mathrm{Si_3N_4}$ they result from variations in substrate charging. The observed similar proximity effects in He⁺ IBID on bulk Si can also be explained by the scattering of particles and the enhanced precursor gas coverage. The only difference lies in the extent of the change of the pillar dimension. The smallest separation to avoid the proximity effect for He⁺ IBID is 500 nm which is much smaller than the 3 μ m for Ga⁺ IBID. This difference is mainly due to the different scattering of He⁺ beam and Ga⁺ beams.

The above three paragraphs summarize the conclusions of three different aspects of IBID pillar growth discussed in this chapter: process dependences, formation of rough sidewall and halo, and the proximity effect. In fact, these three aspects are all about the interplay among the factors involved in IBID (the primary ions and secondary atoms and electrons, precursor gas coverage, and the substrate condition) under different conditions. Our work shows that a better understanding of this interplay is helpful to fabricate an IBID pillar in a desirable way.

Chapter 4

Fabrication and characterization of IBID nanopores

4.1 Abstract

The previous chapter discussed nanopillar growth by ion-beam-induced deposition (IBID). It would be very interesting if IBID could also fabricate negative patterns such as nanopores, especially considering the wide applications of nanopores in nanoscience.

Section 4.2 introduces the research topics. Section 4.3 presents the experimental procedure for the experiments described in Sections 4.4-4.5.

Section 4.4 explains how to fabricate sub-10-nm-diameter nanopores in a Si_3N_4 membrane by a deposition technology: IBID. Two typical precursor gases representing conductive $(CH_3)_3Pt(C_pCH_3)$ - CPC for short and insulating Tetra Ethyl Oxysilane - TEOS for short are used. Pores are formed by exploiting the competition between sputtering and deposition during Ga^+ IBID. The pore diameter can be controlled by carefully adjusting the ion beam and gas exposure conditions. As observed, at the beginning a relatively large pore is formed then shrinked. The final pore diameter 5.5 nm is well below the limit that can be achieved by Ga^+ focused ion beam (FIB) milling alone. As demonstrated, one does not need any special preparations and successive treatments to fabricate sub-10 nm nanopores by IBID. Apart from the simplicity and the speed-a few seconds per pore-, another advantage of this method is a broad choice of material of the deposit and the membrane.

The work presented in this chapter has been published as (1) P. Chen, M-Y. Wu, H. W. M. Salemink, and P. F. A. Alkemade, *Nanotechnology* 20, 015302 (2009). (2) M-Y. Wu, P. Chen, P. F. A. Alkemade, H. W. M. Salemink, and H. W. Zandbergen, accepted by *Micro*.

Section 4.5 discusses the characterization of IBID nanopores, which is required for functionalization of these nanopores. For this purpose, three-dimensional (3D) electron tomography, EDX and EELS analysis are used to measure the changes in chemical composition and shape of the pores after their formation and at various stages of pore shrinkage. Pore formation and shrinkage are shown to be due to a shifting competition between IBID and material sputtering during ion-beam exposure. The chemical distribution at the rim of the nanopore is dependent on the precursor gases used: CPC forms a thin carbon layer with small embedded Pt particles at the top and inner surfaces of the nanopore, whereas TEOS forms SiO_xC_y with Ga particles dispersed at the rim of the nanopore. Furthermore, SRIM simulation shows that forward and backward sputtering depend differently on membrane thickness, which can also play a role in pore formation and shrinkage.

This chapter concludes by demonstrating that sub-10-nm-diameter nanopores can be fabricated by a single IBID step and that we have learned the chemical composition and geometric shapes at various stages of the growth in detail. Nevertheless, more efforts will still be required to functionalize IBID nanopores in the future.

4.2 Introduction

Nanopores have important applications in many fields of nanoscience, e.g. for sensing a single DNA molecule [246, 247], for localizing molecular-scale electrical junctions and switches [248, 249], for fabricating point contacts [250, 251] and nanoelectrodes in electrochemistry [252] or for measuring 3D intensity profiles of laser focuses [253].

For simple pore fabrication, direct FIB milling of a thin membrane is commonly used. With a 5-nm-diameter (FWHM) ion beam, Gierak et al. fabricated sub-5nm-diameter pores in a 20-nm-thick ultrathin SiC membrane [36]. Using a signal feedback from an ion detector below the membrane, Patterson et al. fabricated 18nm-diameter pores in a thick Si₃N₄ membrane [254]. However, it is generally believed that fine-tuning of the pore size by FIB milling is difficult, and the resolution that can be achieved is limited by the beam diameter, beam shape and re-deposition, especially for thick membranes [36, 255]. Pores in Si₃N₄ or SiO₂, which were initially fabricated by FIB milling or electron beam lithography, shrunk or grew upon exposure with a low-energy ion beam [256] or a high-energy electron beam [257]. The assumed mechanism is mass flow driven by surface tension. Feedback from an ion detector below the membrane [256] or visual feedback in a transmission electron microscope (TEM) [257] allows fine-tuning of the pore diameter with sub-nanometer resolution. Lo and Biance shrunk FIB-milled pores in SiN by subsequent FIB scanning [258, 259]. Chang used scanning electron microscopy (SEM) scanning to shrink pores in Si and SiO₂, which were fabricated by micromachining [260]. Wu used laser heating to shrink mechanically punctured holes in thermal plastics [261]. Despite the extensive use, the mechanism of surface-tension-driven mass flow in pore shrinkage during broad-area beam scanning is still not yet fully understood [260, 262]. FIB-milled pores can also be shrunk by thin-film deposition on prefabricated pores, either by IBID [263–265], electron-beam-induced deposition (EBID) [266], low-pressure chemical vapor deposition (LPCVD) [255], or atomic layer deposition (ALD) [267, 268]. However, the control of the final pore size is not straightforward. For instance, Schenkel et al. observed that the larger one of two initial pores became into the smaller one during thin-film deposition [263]. They attributed this effect to differences in the local supply of the precursor molecules.

Despite the large variety of pore fabrication techniques, it is still very desirable to develop simpler and faster methods. In this chapter, we report a new method for the fabrication of sub-10-nm-diameter nanopores in a fast, single IBID step. We employed two very different precursor gases, $(CH_3)_3Pt(C_pCH_3)$ for metal (Pt) deposition and TEOS for insulator (SiO₂) deposition. The essence of our method is to control the dynamic balance between sputtering and deposition involved in IBID. This can be achieved by adjusting the standard IBID parameters.

Furthermore, using TEM we measured the 3D structure and composition of the IBID nanopores, which must be known in order to functionalize nanopores. Our TEM results support the pore formation mechanism as proposed above and outlined for the first time the 3D chemical distribution of nanopores fabricated by FIB milling

4.3 Experimental

 $(CH_3)_3Pt(C_nCH_3)$ was used as precursor for Pt deposition and TEOS for SiO₂ deposition. The Ga⁺ IBID experiments were performed in two FEI dual beam systems, a STRATA DB235 for Pt deposition and a NOVA 600 for SiO₂ deposition. The substrate was a double-polished Si wafer with 45-nm-thick Si_3N_4 top and bottom layers and a $400\times400~\mu m^2~{\rm Si_3N_4}$ window at one side. The ${\rm Si_3N_4}$ membrane was deposited by LPCVD at °C. A 30 keV focused Ga⁺ beam at normal incidence was used. The beam currents were 1, 8, 10 and 13 pA. The FWHM of the incident beam is 10 nm (1 pA) and 12 nm (8, 10 and 13 pA). In the STRATA DB235, the chamber pressure was 2.3×10^{-6} mbar during IBID and the background pressure was $<1 \times 10^{-7}$ mbar. In the NOVA 600, the pressures were 1.1×10^{-5} mbar and 4.3×10^{-6} mbar, respectively. The nominal pumping speed is 250 l s⁻¹ for nitrogen (as provided by FEI). Assuming that this value can be used for the precursor gas as well, the flow rate is thus about 1×10^{-3} scc s⁻¹. To ensure a constant precursor supply, the precursor was always introduced into the chamber at least 60 s before the ion beam. To reduce sample charging effects, first a few conductive Pt lines were deposited by IBID on the Si₃N₄ membrane. These lines connect the insulating Si₃N₄ membrane window to the bulk Si. Arrays of 16 pores were fabricated between these Pt lines. The ion beam was cycled continuously between these 16 spots. This procedure ensured sufficient precursor refreshment time, i.e. 15 times the beam dwell time (0.1 ms to 2.0 ms for Pt deposition; 0.1 ms to 5.0 ms for SiO₂ deposition) on each single spot. The total exposure time equaled the dwell time multiplied by the number of executed cycles. On the same sample, a series of pore arrays was fabricated with either different dwell times or different exposure times. We studied the pore formation as a function of ion beam current, dwell time and exposure time. After fabrication, the sample was transferred to a TEM for imaging. Imaging of the Pt deposits was performed in a field emission Philips CM200 TEM and of the SiO₂ deposits in a FEI Tecnai (S)TEM. Both TEMs operated at an accelerating voltage of 200 kV.

Nanopores were characterized a FEI Tecnai (S)TEM for electron beam tomography, energy filtered transmission electron microscopy (EFTEM), and EDX analysis. EFTEM images were recorded using a 5-mm-high resolution Gatan image filter (HRGIF) entrance aperture, a 10 eV window for carbon K-edge acquisition, and a 2 eV window for Ga plasmon peak acquisition. EDX analysis was performed in STEM mode with a spot size of about 0.5 nm. Single-axis tilt series of 141 images were acquired from -70° to 70° with a tilt increment of 1°. A software, namely IMOD [269] was used to make 3D reconstructions of these tilt series. A pixel size of 0.5 nm was obtained for the final images. Nanopores were put into TEM directly without any treatment for normal imaging and pore size checking. A 40-s oxygen plasma cleaning (25% oxygen and 75% argon) was performed before placing the samples into TEM for 3D electron tomography and EDX analysis to avoid contamination. No change in specimen was observed by TEM after the oxygen plasma cleaning.

4.4 Fast single-step fabrication of nanopores by IBID

4.4.1 Beam current dependence of nanodot or nanopore fabrication on a Si_3N_4 membrane

With a low current of 1pA, only Pt dots were obtained (Fig. 4.1a). With 8 pA, pores formed in the center of the dots (Fig. 4.1b). With 24 pA, the pore diameter was considerably larger (not shown). In the results of Figs. 4.2 to 4.4, an ion beam current of 8 pA was chosen for Pt deposition and 13 pA for SiO₂ deposition.

4.4.2 Dwell time dependence of nanopore fabrication with CPC and TEOS precursors

To investigate the dwell time dependence of the pore diameter, a constant exposure time of 4 s per pore for Pt deposition and 2 s per pore for SiO_2 deposition was chosen (Fig. 4.2). In both cases, the pore diameter increases with increasing dwell time. This trend decelerates for long dwell times. With short dwell times (< 0.3 ms), no pores formed. With medium dwell times (0.3 - 1.0 ms), the pore diameter increases rapidly, whereas with long dwell times (> 1.6 ms for Pt and > 3.0 ms for SiO_2 deposition), the pore diameter stabilizes.

4.4.3 Exposure time dependence of nanopore fabrication with CPC and TEOS precursors

To investigate the exposure time dependence of the pore diameter, a medium dwell time of 0.5 ms was chosen for Pt deposition and 1.0 ms for SiO_2 deposition. The results are shown in Fig. 4.3. At the early stage of exposure, the membrane was opened very rapidly (< 0.5 s for Pt and < 1.0 s for SiO_2 deposition). Then the pores closed slowly with increasing exposure time until they became fully closed (at 18 s for Pt deposition). The closing slows down with decreasing pore diameter. The smallest pore diameter was 11 nm for Pt deposition and 5.5 nm for SiO_2 deposition. For comparison, the diameter of several FIB milled pores is also shown in Fig. 4.3a. Initially (≤ 1 s), these FIB pores grew very rapidly until the pore diameter exceeded 100 nm.

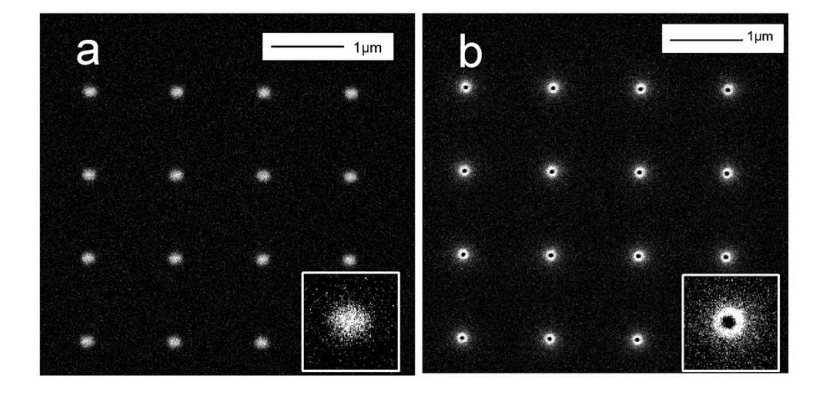


Figure 4.1: Ion beam current dependence of pore formation. SEM top views of Pt deposits on a 45-nm-thick Si₃N₄ membrane, fabricated (a) with 1-pA 30-keV Ga⁺, only dots have formed; (b) with 8-pA 30-keV Ga⁺, a pore has formed in the center of the dot. (Dwell time is 1 ms and total exposure time is 1 s per dot.

4.4.4 Investigation of the geometry of IBID nanopores

An investigation of the geometry of the nanopores is helpful both to understand the pore formation and to explore their possible applications. Assuming a cylinder shape and using geometric formulas, we measured the pore length of the pores fabricated by Pt deposition by comparing 30° tilted TEM views with top views (Fig. 4.4b and c). We observed that the pore length increases with decreasing pore diameter. This trend accelerates when the pore diameter falls below 20 nm (Fig. 4.4a).

4.4.5 Discussion

We have observed that nanopores as small as 5.5 nm in diameter can be fabricated in a single-step IBID process. We found that the pore diameter can be controlled by adjusting the beam current, dwell time, or exposure time. It is well known that sputtering and deposition occur simultaneously in IBID. Sputtering is usually regarded as a negative factor that reduces the deposition rate and, therefore, most attention so far has been paid to suppressing sputtering during IBID. This work shows that sputtering can also be useful in IBID. However, exploration of new applications requires a better understanding of the relationship between sputtering and deposition. Mechanisms involved in IBID are depositions by (I) primary ions, (II) sputtered atoms, and secondary electrons [188, 222], see Fig. 4.5. Each mechanism has its own specific reaction zone around the impact site (Fig. 4.5a). The reaction zone of incoming primary ions (I) is comparable to the beam size. Secondary (sputtered) atoms and secondary electrons can travel a long distance in the solid before emission (II). In this work we exploited the competitions between sputtering and deposition in the various reaction zones to control the shape of the deposits. Control was achieved by adjusting one of the following three standard IBID parameters: beam current,

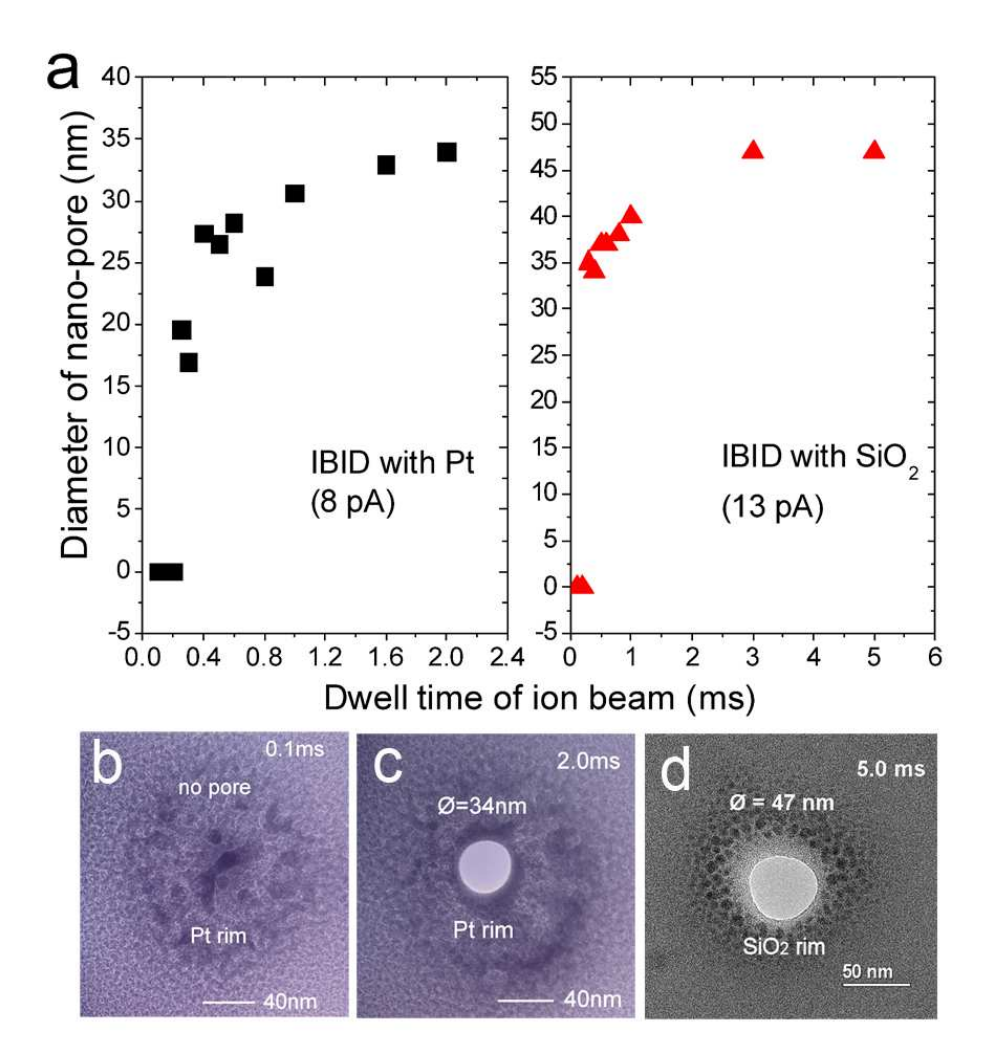
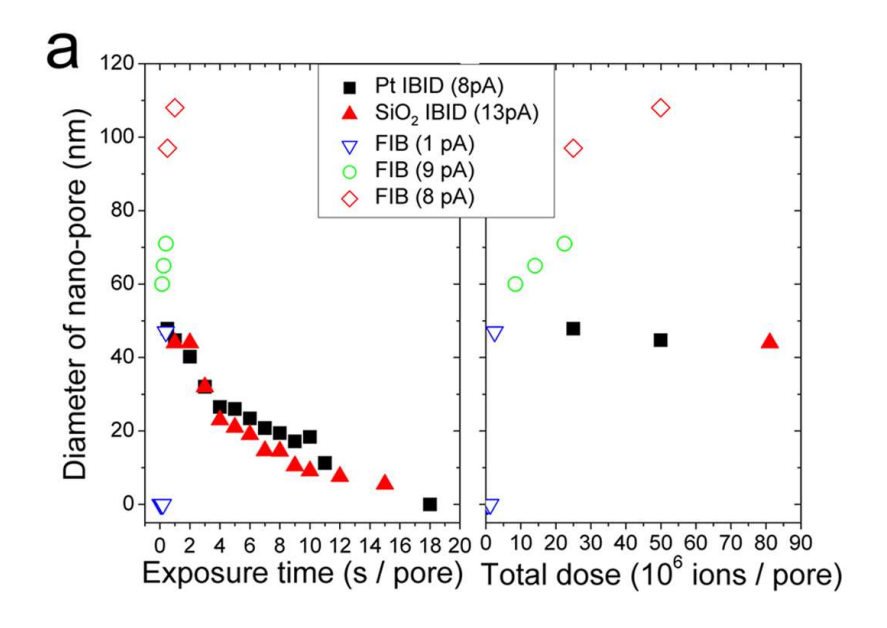


Figure 4.2: Dwell time dependence of pore formation. (a) Pore diameter versus dwell time for Pt or SiO_2 depositions, with 8-pA or 13-pA 30-keV Ga^+ and exposure time of 4 s or 2 s per pore, respectively. TEM top views of Pt deposit with dwell times of (b) 0.1 ms (no pores formed), (c) 2.0 ms (a central pore formed); (d) SiO_2 deposit with a dwell time of 5.0 ms.



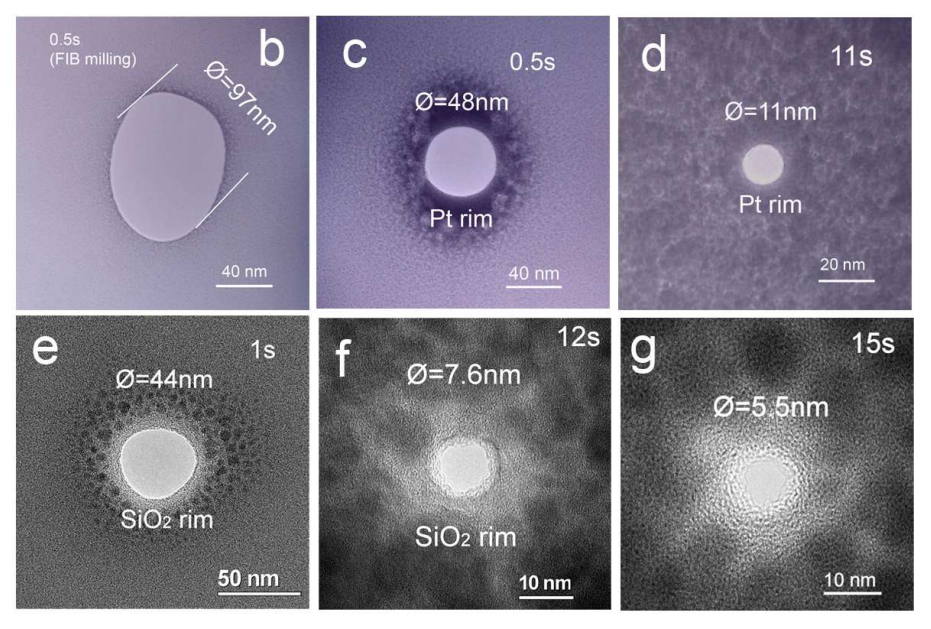


Figure 4.3: Exposure time dependence of pore formation. (a) Pore diameter versus exposure time. Pt or SiO_2 depositions with 8-pA or 13-pA 30-keV Ga^+ and dwell times of 0.5 ms or 1.0 ms, respectively; TEM top views of (b) a FIB milled pore with an exposure time of 0.5 s per pore; pores fabricated by Pt deposition with exposure times of (c) 0.5 s, (d) 11 s per pore; by SiO_2 deposition with exposure times of (e) 1.0 s, (f) 12 s, and (g) 15 s per pore.

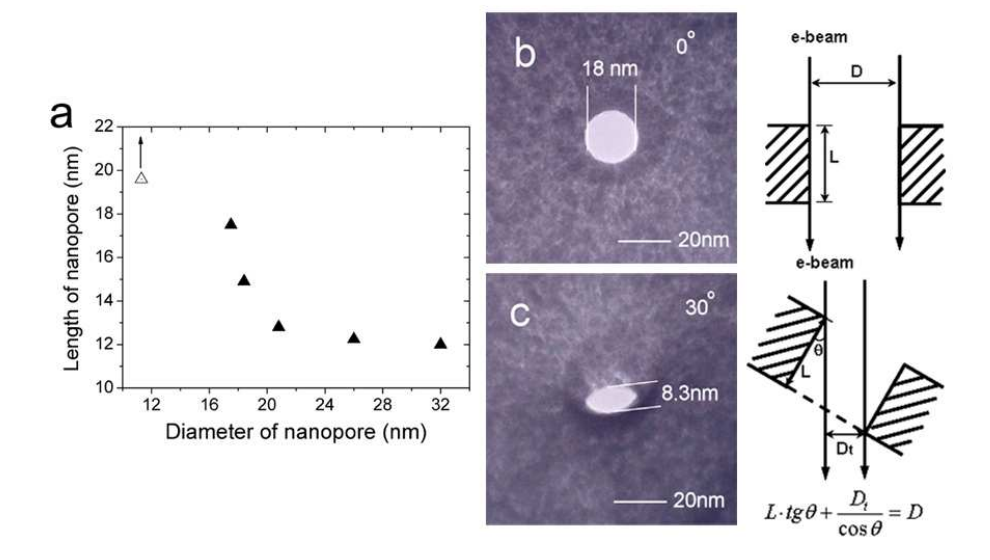


Figure 4.4: Pore shape.(a) Measured pore length versus pore diameter. Pt deposits with 0.5 ms dwell time and various exposure times. The 11-nm-diameter pore must be at least 20 nm long because it was invisible in the 30° tilted TEM image; TEM (b) top view of an 18-nm-diameter pore; (c) tilted view of the pore in (b).

dwell time or exposure time. Indeed, complex structures such as doughnut-like deposits with a central tip (Fig. 4.5b) or with a central hole (Fig. 4.5c) have been obtained in a single IBID step in spot mode by adjusting the dwell time [188]. Below we propose a model that explains how these parameters affect the pore formation.

The sputtering yield Y_s , expressed as the number of sputtered atoms per incident ion, is independent of the ion beam density. On the other hand, the deposition yield Y_d , expressed as the number of deposited atoms per incident ion, depends on the ratio between the ion beam density j and the precursor flux ϕ [184, 188, 198, 270]. For a fixed precursor flux, the deposition yield is independent of the ion beam density for low values of j, but decreases above a critical ratio between j and ϕ . Hence, for a low beam current in spot mode and a sufficient precursor flux, deposition dominates over sputtering and only dot-like deposits form (Fig. 4.1a). In contrast, for a sufficiently high beam current with the same gas flux and beam diameter, sputtering dominates in the center of the deposit where the ion beam density is highest. Hence, a central pore forms (Fig. 4.1b). Nevertheless, deposition by secondary electrons and atoms [188, 222] dominates in the rim area, where sputtering by primary ions is low or absent.

With shorter dwell times, smaller pores form (Fig. 4.2). We will discuss the dwell time and ion-beam-density dependencies of the pore formation in terms of the sketch in Fig. 4.6. In each cycle, adsorbed precursor molecules are consumed at the beam

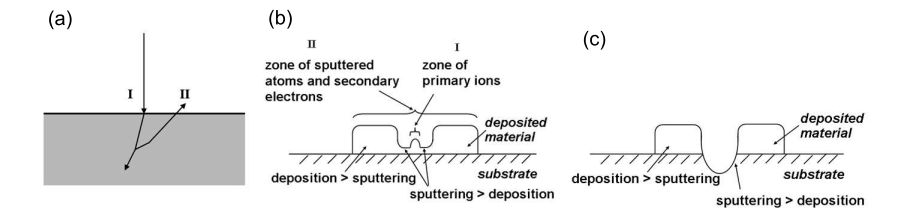


Figure 4.5: Balance between deposition and sputtering in IBID. Sketches of (a) activity regions of different particles contributing to IBID: I incident primary ions, II sputtered atoms and secondary electrons. Reaction zones of I, II and doughnut-like structures with (b) a central tip, fabricated with a short dwell time (c) a central hole, with a long dwell time.

spot during the beam-on step A. The adsorbed precursor layer is then refreshed during the beam-off step B. In our experiment the refreshment time is chosen to be long enough so that the precursor surface coverage θ_p saturates again before the next cycle starts. The deposition yield Y_d strongly depends on the precursor surface coverage θ_p . In particular, it decreases during step A. Sputtering is caused by ion-solid interactions. Therefore, the sputtering yield Y_s is independent of the precursor coverage; it remains constant during step A. For short dwell times (short dashed lines in Fig. 4.6) the deposition yield exceeds the sputtering yield for most of duration of step A. Nevertheless, averaged over the entire step A, Y_d - Y_s is positive and, thus, a deposit forms. On average, sputtering dominates over deposition for long dwell times (thick solid lines). The balance between deposition and sputtering is delicate at medium dwell times. For the usual Gaussian-like beam profile, sputtering can dominate in the center of the beam spot (thin solid line), whereas deposition dominates in the rim (long dashed line). A small change in beam density or dwell time can flip the balance. Indeed, Fig. 4.2a shows that the pore diameter varies rapidly with dwell time just above a certain threshold.

For a dwell time just above the threshold, the membrane opens rapidly at the early stage of beam exposure (see Fig. 4.3). The pores close again with increasing exposure time. We discuss the opening and closing process as sketched in Fig. 4.7. Initially (Fig. 4.7a) all ions interact with the membrane and therefore sputtering is strong. There is some deposition in the rim area. After the membrane has been opened, most ions pass through the pores without any interaction (Fig. 4.7b). However, the deposit in the rim continues to grow. When the thickness L of the deposit increases, more precursor molecules adsorb on the pore's sidewall and more secondary electrons and atoms are emitted. Both effects enhance the deposition yield at the pore's sidewall. Therefore, the pore closes after Fig. 4.7c. Note that the pore in Fig. 4.7d closes, although it has the same diameter D as the pore in Fig. 4.7b. We presume that deposition on the sidewall is caused mainly by secondary atoms and electrons; thus processes II and III in Fig. 4.5. The closing slows down with decreasing pore diameter until the pores are fully closed (Fig. 4.3a). Owing to the high beam current density in the pore's center, the net deposition rate at the sidewall decreases with decreasing

pore diameter. Moreover, the increasing aspect ratio of the pore (Fig. 4.4) might slow down the precursor supply to the pore's sidewall, thus slowing down the closing process even further. Actually, the slow rate of pore closing allows fine-tuning of the pore diameter.

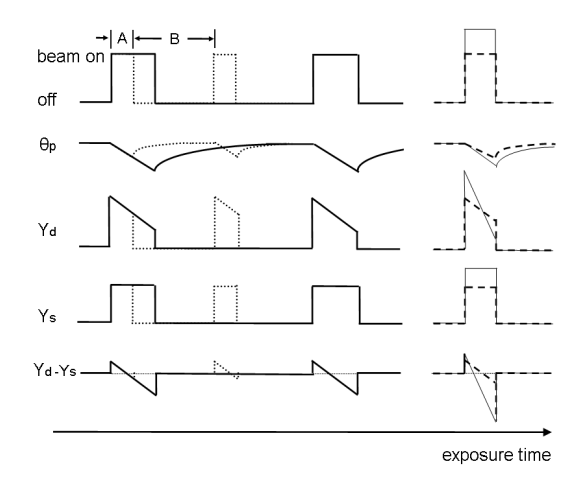


Figure 4.6: Sketch of dwell time dependence of pore formation. Step A: beam on. Step B: beam off. θ_p : precursor surface density. Y_d : deposition yield (which is proportional to θ_p). Y_s : sputtering yield (which is constant). Y_d - Y_s : net deposition. Short dashed lines: short dwell times. Thick solid lines: long dwell times. The net deposition Y_d - Y_s averaged over step A is positive for short dwell times (short dashed lines) and negative for long dwell times (thick solid lines). At right: medium dwell time. The beam current density affects the balance between deposition and sputtering: for a higher density (thin solid) the average net deposition is negative, for a lower density (long dashed) it is positive.

The smallest pore diameter achieved so far is 5.5 nm, which is less than 50% of FWHM of the beam profile. Although it was possible to close a pore completely, it is not certain that the diameter was well below 5 nm at any given moment. Further investigations with preferably even smaller ion beams might reveal whether the biologically important diameters below 2 nm are achievable.

The IBID method for nanopore fabrication has several advantages over current techniques. It surpasses the main limitation for direct FIB milling, which is a rapid widening of the pore diameter caused by the ion intensity in the tail of the beam profile. A small variation in the membrane thickness [259] or a small instability in the beam current can result in a pore that is either too shallow or too wide. Contrary to the methods in which a wide pore is shrunk by successive processing steps [255–268] our method is based upon a single processing step. Techniques that are based on surface-tension-driven mass flow, such as ion-beam sculpting [256] and electron-beam-induced drilling [257], have produced pores with diameters as small as 2 nm. However, it is unclear whether these techniques can be applied to thick

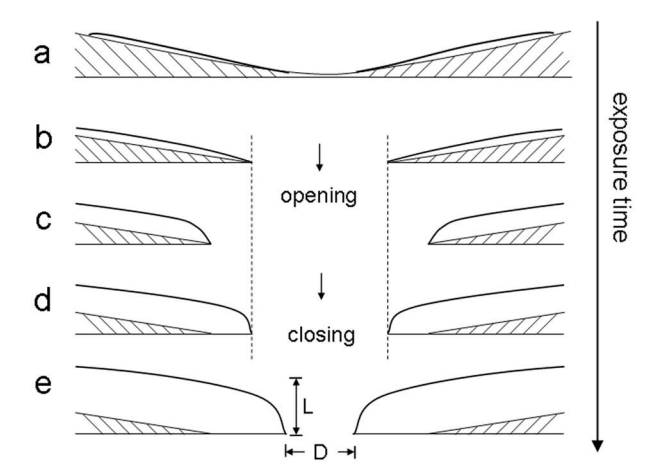


Figure 4.7: Sketch of the exposure time dependence of pore formation. (a)-(c): pores open; (c)-(e): pores close. D and L: pore diameter and length, respectively; white and shaded region: IBID deposits and membrane.

membranes and other materials as well. Our IBID method offers a broad choice of materials and thicknesses for both the membrane and the deposit.

In most FIB instruments there is a limited choice of beam currents. To fabricate small nanopores, the lowest current is preferred. The high sensitivity of the pore diameter for the dwell time (Fig. 4.2a) hinders fabrication of very small pores by optimizing the dwell time. Probably the best approach for fabrication of pores with a required diameter is to select a dwell time just above the steep rise in Fig. 4.2 and to optimize the exposure time. A valuable option is a feedback system -such as an ion detector or a Faraday cup below the membrane- to stop the fabrication process when the required diameter is reached. Interestingly, the diameter of the smallest pores achieved in this work is less than half the ion beam diameter. The use of an even smaller beam [36] might make fabrication of 1 nm pores feasible.

4.5 TEM study of nanopores fabricated by IBID

4.5.1 EDX & EFTEM analysis and 3D electron tomography of nanopores fabricated by FIB milling and by IBID with CPC precursor

Fig. 4.8 shows TEM images of nanopores fabricated with a 12-nm-diameter Ga⁺ FIB without gas and with CPC gas. Continued irradiation with the Ga⁺ FIB without precursor gas leads to a continuous increase of the pore size if no precursor gas is used (Fig. 4.8a; note that the image sequence is not shown). In contrast, it leads to a

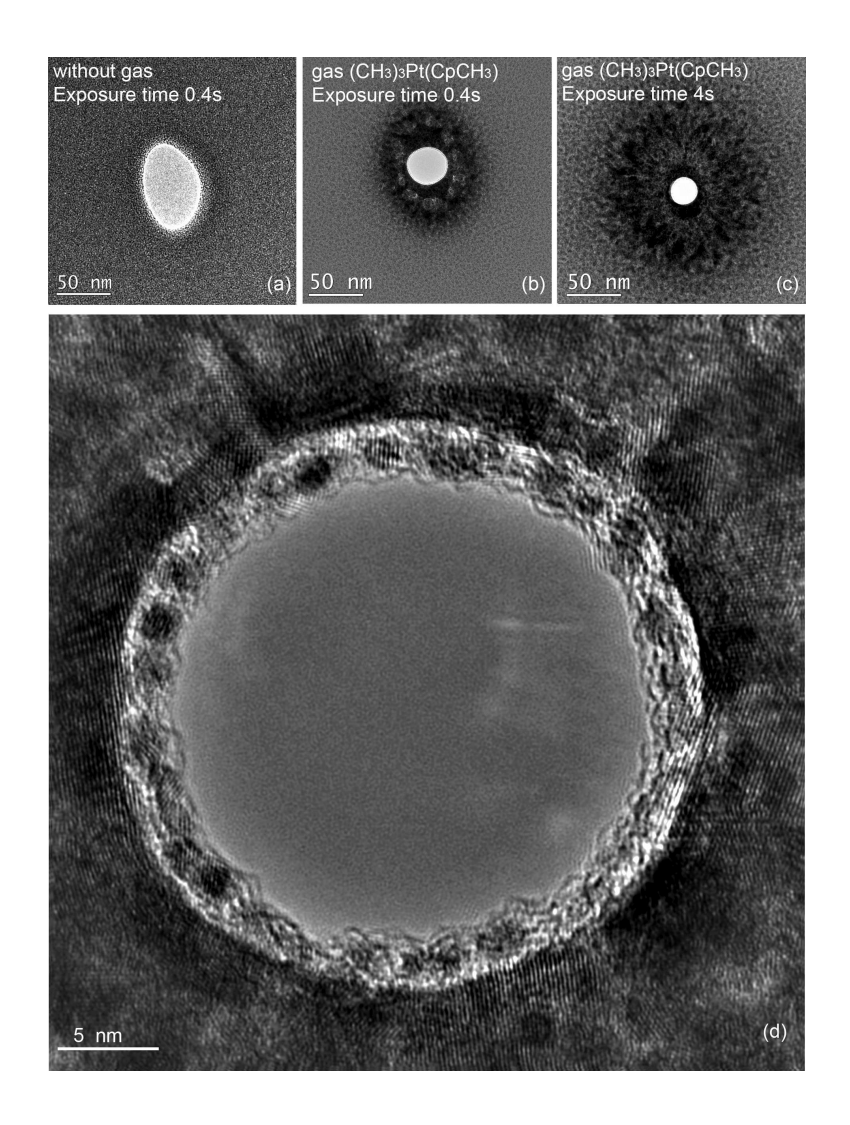


Figure 4.8: TEM images of nanopores fabricated by a 12-nm-diameter, 8-pA, 30-keV Ga^+ FIB with and without CPC gas for different exposure times in a 45-nm-thick Si_3N_4 membrane. (a) without precursor gas; exposure time: 0.4 s; pore diameter: 78×51 nm. (b) With CPC gas; exposure time 0.4 s; pore diameter: 33 nm. (c) With CPC gas; exposure time: 4 s; pore diameter: 21 nm. (d) High-resolution electron microscopy image of a pore made under the same experimental conditions as in (c).

pore size decrease if CPC is used (Fig. 4.8b-d). The nanopore fabricated without gas and at 0.4 s exposure time is 65 nm in diameter (Fig. 4.8a), whereas the one fabricated with CPC gas is 33 nm in diameter at the same exposure time (Fig. 4.8b). When the exposure time is increased to 4 s, the diameter of the latter nanopore decreases to 21 nm (Fig. 4.8c). The smallest pore size observed is 11 nm for an even longer exposure time. Concurrently with pore shrinkage, changes in the image contrast around the pore are observable. There is an increase in the width of the dark rim around the pore, indicating a continuous incorporation of a heavy element. In the high-resolution electron microscopy (HREM) image of a 20-nm-diameter nanopore (Fig. 4.8d), one can see that a thin layer with small crystallized particles formed at the edge of the pore. Furthermore, crystals formed next to this layer (see also the 3D electron tomograms in Fig. 4.10).

Fig. 4.9 shows the EDX line scans across three nanopores, fabricated without gas (Fig. 4.9a) and with CPC precursor gas (Figs. 4.9b,c). The elemental distributions of Si, N, Ga, Pt, and C near these pores as well as various element ratios are given. The N/Si ratio for the pore made without gas is constant up to the edge of the pore. This composition differs from pores made with an electron beam, where more N is Si is lost [262]. Note that the rim of the nanopore contains also Ga and traces of C. The two nanopores made with a gas exhibit the elements Ga, C, and Pt over a large areaup to more than 150 nm from the edge. Ga is found near all these three pores, but it has different densities depending on the exposure time and the material (note that the thickness and chemical composition of the film change during deposition). For the short exposure time (Fig. 4.9b), the N/Si ratio is nearly constant up to the edge of the nanopore, but it is substantially lower for the longer exposure time (Fig. 4.9c). This shows that Si as well as N diffuses to the area of the deposited material, causing the nanopore to shrink. In both nanopores fabricated with gas, there is a distinct gradient in the Pt/C ratio at the very edge of the nanopores. Additionally the Pt/C ratio in Fig. 4.9c is constant in a range of 20-60 nm from the edge of the nanopore.

To determine the 3D shapes of the nanopores, 3D reconstructions of single-axis tilt series of 141 TEM images were performed by IMOD software. Fig. 4.10a shows the results for the nanopore fabricated without gas, whereas Figs. 4.10b and c show those for the nanopore fabricated with CPC gas. For each nanopore, one X Z slice (Z is the ion beam direction) is shown in Figs. 4.10a-c and three X Y slices are shown in Figs. 4.10a-c.1-3 (positions of X Y slices are marked by the crosses in Figs. 4.10a, b, c). The ion beam current used for these nanopores is 10 pA, which is larger than that for the pores shown in Figs. 4.8 and 4.9. Therefore, the pores in Fig. 4.10 are larger. The differences in pore shape and in the distribution of the material and shape can be seen in the various slices. The main components are drawn schematically in Figs. 4.10a-c.4, respectively.

When a nanopore is fabricated without gas (Fig. 4.10a and Fig. 4.10a.1-3), the sidewall is rounded (like the inside of a donut), but not mirror-symmetric about the plane of the middle of the membrane (half plane). Small black dots are visible in all slices, indicating the presence of small particles dispersed over the inner surface of the nanopore (layer a1 in Fig. 4.10a.4). EDX analysis revealed that they are Pt-rich. This is remarkable because the pore was made without gas. Probably the

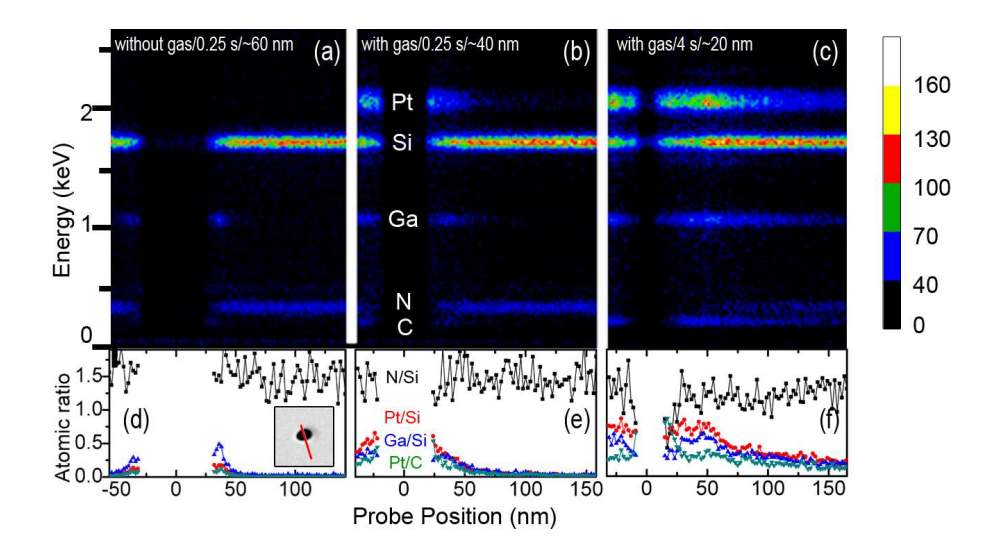


Figure 4.9: EDX analysis of nanopores of different sizes fabricated by a 12-nm, 8-pA, 30-keV Ga⁺ FIB with and without CPC gas in a 45-nm-thick $\rm Si_3N_4$ membrane. (a) \sim 60-nm-diameter nanopore fabricated without gas. (b) \sim 40-nm-diameter nanopore fabricated with CPC gas and exposure time 0.25 s (c) \sim 20-nm-diameter nanopore fabricated with CPC gas and exposure time 4 s (d-f) are atomic ratios of N/Si, Pt/Si, Ga/Si and Pt/C for (a-c), respectively.

unintentional Pt deposition is due to some gas residue after the Pt line deposition at the beginning of the experiment.

Nanopores fabricated with CPC gas using the same short exposure time of $0.4~\rm s$ show a similar asymmetry about the half plane, but the pore size is smaller and the composition is different (Figs. 4.10b and b.1-3). A \sim 5-nm-thick layer with embedded Pt particles is present over the top and inner surfaces of the nanopore (layer b1 in Fig. 4.10b.4). Beneath this layer, one can observe a region with large contrast variations laterally and vertically (Figs. 4.10b.1-4). In slice 1, small \sim 3-nm-diameter spherical particles with low scattering density can be seen in the dark rim. EFTEM analysis shows that they are highly C-rich. Some of these C-rich particles are not homogeneous; apparently they contain 1 to 2-nm-diameter Pt particles. In slices 2 and 3, the C-rich particles have merged and are located primarily 20-40 nm from the edge of the pore. The region of dark contrast near the edge of the pore (layer b3 in Fig. 4.10b.4) is Pt-rich, as confirmed by EDX. Additionally, a \sim 1-nm-thick, highly Pt-rich layer is present on the sub-inner surface (layer b2 in Fig. 4.10b.4).

For the longer exposure time, the deposited layer gets thicker, resulting in a smaller nanopore (Fig. 4.10c.1-4). Moreover, the shape of the nanopore changes. The membrane bends along the direction of the ion beam, whereby the deviation from the half plane starts at a distance of 50 nm from the edge of the nanopore. Similar to the 65-nm-diameter nanopore fabricated with the shorter exposure time, a thin

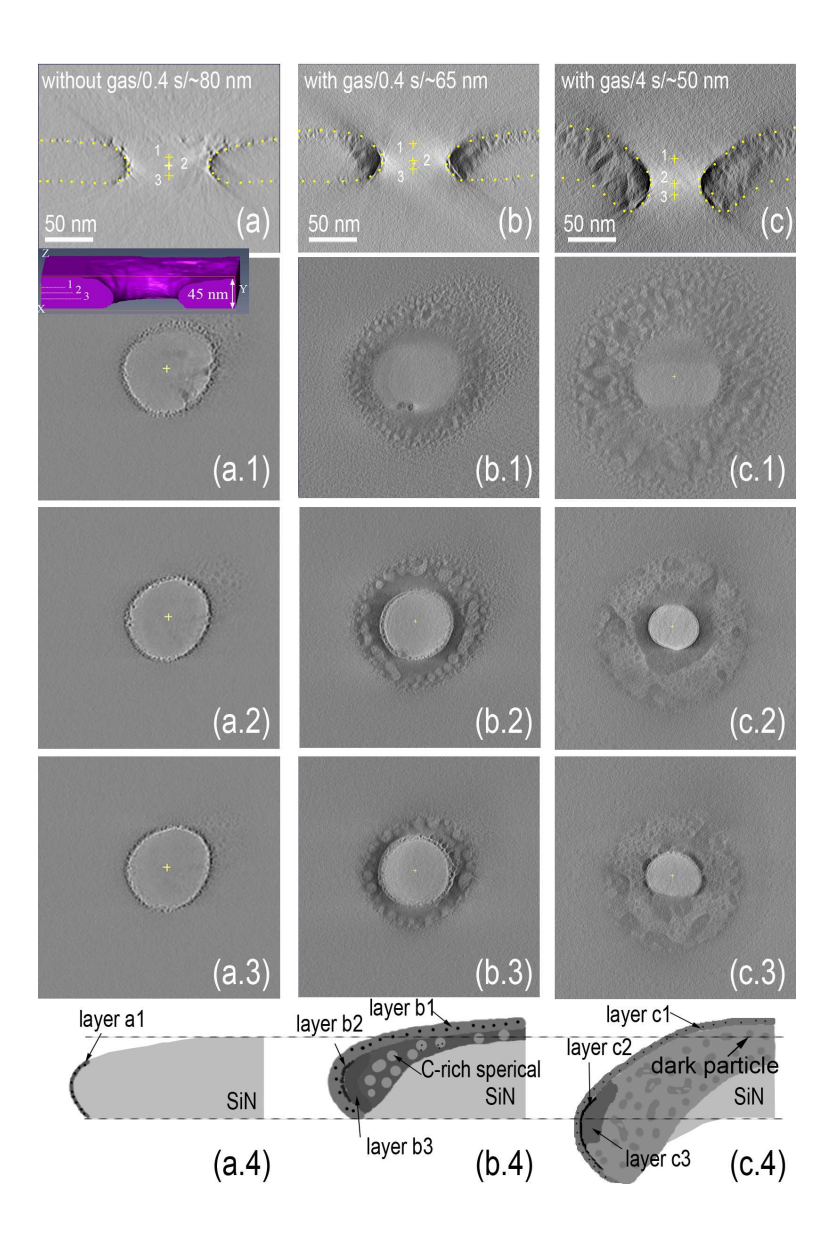


Figure 4.10: Slices from 3D reconstructions of three nanopores fabricated by a 12-nm-diameter, 10-pA, 30-keV Ga^+ FIB with and without CPC gas in a 45-nm-thick Si_3N_4 membrane. (a) \sim 80-nm-diameter nanopore fabricated without gas. (b) \sim 65-nm-diameter nanopore fabricated with CPC gas. (c) \sim 50-nm-diameter nanopore fabricated with CPC gas. The crosses in a, b and c mark the cutting heights for the slices in a.1 to c.3. The dots outline the surface of the nanopore. The inset shows the surface reconstruction image of the nanopore given in (a). The observed structure is explained in the lowest panel (a.4-c.4).

layer of C with embedded Pt particles is present at the top and inner surface, but in this case, it is ~2.5-nm-thick (layer c1 in Fig. 4.10c.4). Beneath this layer, there is also a region with large lateral and vertical contrast variations, similar to that of the 65-nm-diameter nanopore but of different sizes (Fig. 4.10c.1-3)). We assume that the small C-rich spheres have merged, resulting in a large C-rich annular ring as shown in slice c.2. The small dark particles are positioned in a shell shape, which could be due to the merging of the C-rich particles. Secondly, unlike for the 65-nm-diameter nanopore, the region with dark contrast (layer c3) exists only at the upper part of the nanopore. The sub-inner surface (layer c2 in Fig. 4.10c.4) of this nanopore is similar to that of the 65-nm-diameter nanopore.

4.5.2 EDX & EFTEM analysis of nanopores fabricated by IBID with TEOS precursor

Fig. 4.11 shows TEM images of the nanopores fabricated by 12-nm Ga⁺ FIB without gas (Fig. 4.11a) and with TEOS gas (Figs. 4.11b-c). Fig. 4.11b and 4c show 44 and 7.6-nm-diameter pores, obtained with 1 and 12 s exposure times, respectively. The smallest pore size observed is 5.5 nm in diameter for a longer exposure time. With TEOS, the rim of the pore shows a contrast similar to that without a gas (Fig. 4.11a), but with additional dark particles 2 to 7 nm in diameter. EFTEM analysis (Fig. 4.12) shows that they are highly Ga-rich. The size of these particles does not depend on the exposure time. Fig. 4.12 also gives EDX analysis results. As previously shown for CPC gas, the composition of the deposited material varies with the distance to the edge of the nanopore. The O/C ratio at the edge of the nanopore is higher than that farther away from the edge. However, unlike with CPC, Ga is incorporated in the film in the form of Ga-rich particles. The EFTEM image of Fig. 4.12b confirms this observation.

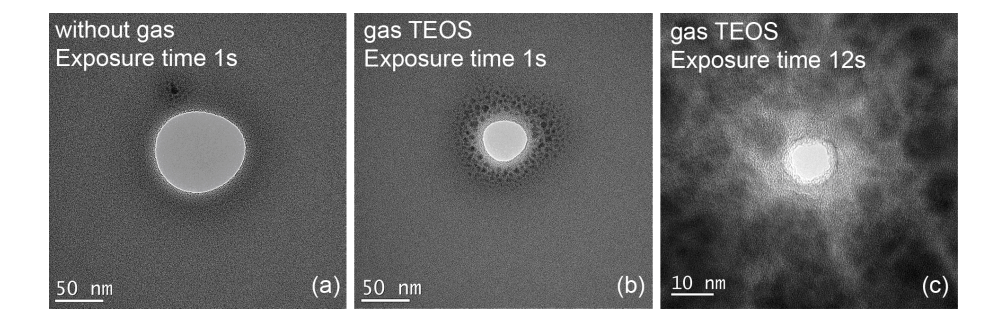
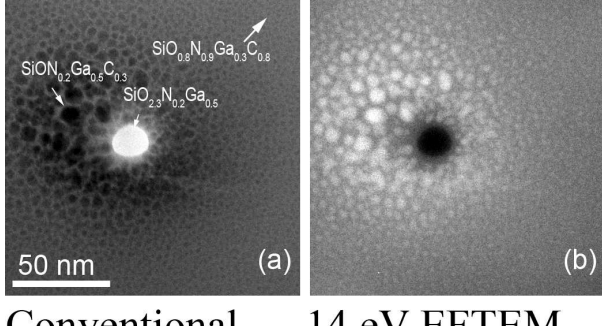


Figure 4.11: TEM images of nanopores fabricated by a 12-nm-diameter, 13-pA, 30-keV Ga^+ FIB with and without TEOS gas for different exposure times in a 45-nm-thick Si_3N_4 membrane. (a) Without precursor gas; exposure time: 1 s; pore diameter: 88 nm (b) With TEOS; exposure time: 1 s; pore diameter: 44 nm (c) With TEOS; exposure time: 12 s; pore diameter: 7.6 nm (note: the scale bar is 10 nm).



14 eV EFTEM Conventional

Figure 4.12: Conventional bright-field TEM image and the correspondent Ga energyfiltered TEM image of a 65-nm-diameter nanopore fabricated by a 12-nm-diameter, 10-pA, 30-keV Ga⁺ FIB with TEOS gas in a 45-nm-thick Si₃N₄ membrane. (a) Conventional bright-field TEM image. The white arrows indicate the positions where EDX were taken. The obtained O/Si, N/Si, Ga/Si and C/Si atomic ratios x, y, z, w at that position are given as $SiO_xN_yGa_zC_w$. (b) Ga energy-filtered TEM image.

4.5.3 SRIM simulation

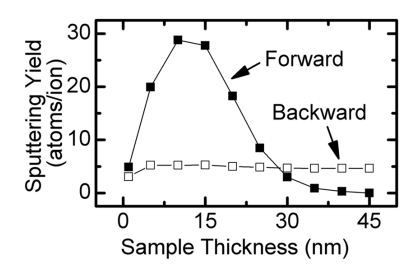


Figure 4.13: Sputtering yield of a 30-keV Ga⁺ ion in Si₃N₄ calculated by SRIM code as a function of sample thickness.

To better understand nanopore formation, the interaction of 30-keV Ga⁺ ions with Si₃N₄ was simulated using the stopping and range of ions in matter (SRIM [163]) code. We assumed a density of 3.44 g/cm³. Fig. 4.13 plots the calculated backward and forward sputtering yields as a function of sample thickness. Clearly, the backward sputtering yield is nearly constant, whereas the forward sputtering yield depends strongly on sample thickness.

4.5.4Discussion

One can make sub-10-nm-diameter nanopores by combining FIB milling and IBID using TEOS or CPC as precursor gas. The final pore diameter decreases with increasing gas exposure time. The formation sequence of a narrow nanopore is as follows: (1) formation of a small nanopore by FIB milling; (2) pore widening by continued milling; (3) pore shrinkage by IBID. Note that in this sequence, the external parameters such as beam intensity, focus, and gas supply are kept constant. An obvious caveat with regard to this process is why one needs deposition as the pore is small to begin with. In other words, how is it possible to make a small nanopore by first etching and then deposition without changing the beam and gas conditions? As put forward in the previous section, the most plausible explanation is the competition between sputtering and deposition during the various stages of the fabrication process. During the formation of the initial small nanopore, little material is deposited on the 45-nm-thick membrane, especially at the center of the illuminated area. Thus the presence of the gas hardly affects the etching process in that area. In the beginning, the substrate atoms are mostly sputtered away from the top surface because the ions do not reach the bottom surface. After milling 17 nm deep, the membrane reaches a thickness of about 28 nm, where forward sputtering starts to dominate over backward sputtering (Fig. 4.13). When the sample thickness is 10 nm, the forward sputtering yield is almost 6 times higher than the backward sputtering yield, which implies that the nanopore is created suddenly, followed by a very rapid increase in width, especially when FIB has a large diameter. Thus, given the size of the FIB (10-12 nm), a sub-10-nm-diameter pore is very difficult to make. However, the large nanopore can be shrunk to a small size with further exposure if a gas is present. With longer exposure time, more material is deposited on the surface of the membrane, thus increasing the thickness and reducing the forward sputtering yield (see the thickness increase between Figs. 4.10b.4 and 4.10c.4). Consequently, it gives rise to net deposition on the sidewall of the pore, and thus to pore shrinking. Besides direct deposition by IBID, other atomic transport phenomena [256, 262] also contribute to pore reduction and closure. As the diffusion of the surface atoms of the initial membrane material, which account for the pore closure in a Si₃N₄ membrane by a 3-keV Ar ion beam illumination in [256], lateral diffusion of Si and N were also evidently found in the EDX elemental map in our case. Diffusion happens in the deposits as well (see below). Moreover, it can be liquid-like as what was found in the pore closure in SiO₂/SiN membrane by an electron beam illumination [262]. In contrast to the creation of the nanopore, shrinkage by IBID is slow. Hence, the shrinking process is more controllable than the actual creation process. Overall, the present TEM analysis and the SRIM calculation support the mechanism of pore formation put forward in the previous section.

One can make nanopores of any predetermined diameter in the range of ~ 5 nm to ~ 50 nm with both gases. The disadvantage of this method, however, is that the composition at various parts near the pore is very complex. With TEOS as precursor gas, one obtains a $\mathrm{SiO}_x\mathrm{C}_y$ -coated with Ga particles embedded in the rim of the nanopore. For CPC the chemistry near the pore is even more complex. At the bottleneck of the nanopore the material distribution from the surface to the $\mathrm{Si}_3\mathrm{N}_4$ membrane is as follows: (1) a 2 to 4-nm-thick C layer with Pt particles embedded in the middle, (2) a ~ 2 -nm-thick highest Pt/C atomic ratio layer, (3) a medium Pt/C atomic ratio layer, and (4) a high C composition layer. Tanaka et al. found Ga-rich particles in SiO_2 and c-Si samples after exposure to a 25 keV Ga⁺ FIB [271]. They

attributed the formation of these Ga-rich particles to the low solid solubility of Ga in SiO_2 and Si. Selman et al. reported that carbon diffuses rapidly in heated Pt membranes, although its solubility in Pt is very low (about 0.02 by weight at 1700 $^{\circ}$ C) [272]. Their results can explain the continuous change of the chemical structure in the rim of the nanopore during IBID, where Ga^+ ions serve as a driving force.

4.6 Conclusions

Accompanying deposition, sputtering always happens during IBID. In most cases, sputtering is considered as a negative factor to be avoided as much as possible. However, nothing is 100% negative as long as we know how to make use of it. As demonstrated in this chapter, by carefully adjusting the standard IBID parameters to control the balance of sputtering and deposition, one can fabricate interesting structures, for instance, sub-10-nm-diameter nanopores. So far, the smallest pores fabricated by IBID are 5.5 nm in diameter. Compared to state-of-the-art techniques, the advantages of fabricating nanopores by IBID are clear. It is fast -a few seconds per pore- and simple- only a single processing step is required. Arrays of thousands of pores can be made within a reasonable time. However, the difficulties of fabricating large amounts of pores are the membrane distortion under FIB bombardment and the need for a homogeneous precursor distribution in a larger area. Furthermore, the IBID pore fabrication method offers substantial freedom regarding a broad choice of membrane and deposit material and thickness. Detailed 3D electron tomography and composition analysis show that, in the proximity of the nanopore, various regions with complicated chemical structures are present. The mechanism of the pore formation is supported by a SRIM theoretical simulation and TEM results.

We foresee that further optimization of the IBID method will bring the important range below 2 nanometers within reach. However, more efforts are required to functionalize IBID nanopores. One difficulty could be the purity issue of the IBID deposits, which is an intrinsic disadvantage of IBID. On the other hand, IBID nanopores are potentially good candidates for applications that need a large amount of nanopores but do not have high requirements with regard to purity, such as devices for light transmission and manipulation. In this chapter, we used Ga⁺ IBID to fabricate nanopores. In principle the novel helium ion microscope (HIM), which can provide sub-nanometer He⁺ ion beam, should work better than Ga⁺ does. However, in our first try we did not succeed to fabricate nanopores by He⁺ milling due to the low milling rate and undesired deposition from contamination in the HIM chamber.

Chapter 5

Multiple mechanisms of IBID

5.1 Abstract

As shown in the previous two chapters, ion-beam-induced deposition (IBID) is capable of fabricating three-dimensional (3D) nanostructures in a flexible manner. However, to gain full control over the dimensions of the deposits, a detailed understanding of IBID mechanisms is required. This chapter summarizes a series of our fundamental research work to distinguish the roles of different mechanisms involved in the Ga⁺ IBID process. In addition, the mechanisms of Ga⁺ IBID, He⁺ IBID and electron-beam-induced deposition (EBID) are compared.

Section 5.2 introduces the research topics. Section 5.3 presents the experimental procedure for the experiments described in Sections 5.4-5.6.

Section 5.4 shows a significant contribution of secondary particles to Ga^+ IBID by comparing the volume of a deposited box inside a crater and near the sidewall of this crater with that of the additional material deposited onto the sidewall. Section 5.5 discusses the investigation of two models that describe IBID in terms of the impact of secondary electrons and of sputtered atoms, respectively. For this purpose, the yields of deposition, sputtering, and secondary electron emission, as well as the energy spectra of the secondary electrons were measured in situ during IBID as functions of ion incident angle $(0^o - 45^o)$ and energy (5 - 30 keV). The deposition yield and the secondary electron yield have the same angular dependences but very different energy dependences. However, this very different energy dependence cannot be explained by the relatively small difference of the energy spectra of the secondary electrons for different ion energies. Furthermore, it is unlikely that the deposition yield per secondary electron (atoms/electron) can be as high as observed (>> 10). On the other hand, within the investigated angles and energy ranges, the deposition yield is

The work presented in this chapter has been published as (1) P. Chen, H. W. M. Salemink, and P. F. A. Alkemade, J. Vac. Sci. Technol. B 27, 2718 (2009). (2) P. Chen, P. F. A. Alkemade, and H. W. M. Salemink, Jpn. J. Appl. Phys. 47, 5123 (2008)

linearly related to the sputtering yield. The offset might be due to the contribution of primary ions. These results indicate that the sputtered atom model describes Ga⁺ IBID better than the secondary electron model. Section 5.6 illustrates the contribution of primary ions. In spot mode by varying the current and dwell time of the ion beam, a doughnut-like structure with a hole or a central tip was obtained, indicating that primary ions probably also contribute to Ga⁺ IBID.

The results presented in Sections 5.4-5.6 are discussed and concluded in Section 5.7 and 5.8. In addition, the conclusion compares the mechanisms of $\mathrm{Ga^{+}}$ IBID, $\mathrm{He^{+}}$ IBID and electron-beam-induced deposition (EBID) by reviewing the studies discussed in this work and published in the open literature. It highlights that IBID has to be explained by multiple mechanisms. Depending on the conditions, probably a single mechanism dominates.

5.2 Introduction

Owing to its high flexibility with respect to the shape and location of deposits, IBID is becoming increasingly interesting as a powerful tool for prototyping 3D nanostructures [108, 113]. We discussed the fabrication of nanopillars and nanopores in the previous two chapters. However, the qualities of 3D nanostructures grown by IBID, such as electrical and mechanical behaviors, are affected by various undesired phenomena. For instance, a typical IBID nanopillar has a surrounding halo and a rough sidewall (Fig. 5.1).

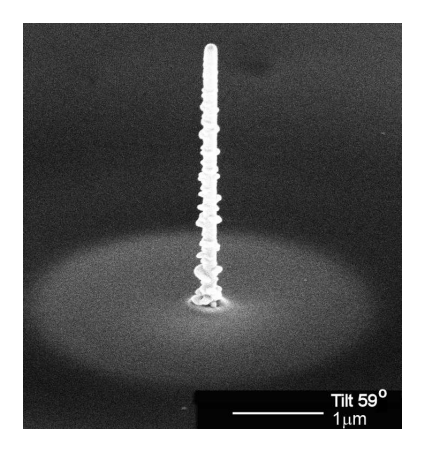


Figure 5.1: Typical pillar grown by IBID with a rough sidewall and a surrounding halo (irradiated with Ga⁺ FIB in spot mode for 180 s; the energy and current were 30 keV and 1 pA respectively)

A detailed understanding of IBID mechanisms is required to gain full control over the dimension and the composition of the deposits. Generally, IBID is considered a very complex process with possible contributions from primary ions, sputtered atom or ions, secondary electrons and thermal spikes [222]. However, the corresponding studies are still limited despite the fundamental drive. Some studies relate IBID to sputtered atom impact and others to secondary electron impact. Dubner et al. found that the deposition yield is proportional to the calculated stopping power by using He⁺, Ne⁺, Ar⁺, Kr⁺, Xe⁺ ion beams within the ion energy range of 2-10 keV and consequently explained IBID by the energy transfer via a cascade of atom-atom collisions to adsorbed precursor molecules [184–186]. Shuman et al. reported a significant contribution of secondary electrons to IBID [223]. Lipp et al. supported the secondary electron model, having observed a proportional relationship between the deposition yield and the secondary electron yield within the ion energy range of 10-30 keV [187]. However, it should be noted that Lipp et al. measured the secondary electron yield during ion beam milling instead of during deposition. Chen et al. found a charging effect on IBID pillar growth which suggests that secondary electrons play an important role [209]. Several other studies also reported contributions from secondary electrons to IBID pillar growth [105, 210, 211]. Moreover, theoretical

studies of EBID, which is closely related to IBID, show that secondary electrons play an important role in EBID [104, 227]. Hence, it is still unclear whether sputtering or secondary electron emission is the predominant mechanism in IBID. It is even unclear whether it is reasonable to rule out the possibility that primary ions are dominant in IBID.

Therefore, in this work, we concentrate on the separate roles of secondary atoms, secondary electrons, and primary ions in IBID. We investigate the two most popular IBID models by comparing in situ measured yields of deposition, sputtering and secondary electron emission as functions of ion incident angle and energy for a single ion-precursor combination. Processes of precursor gas on the solid surface, such as gas adsorption, desorption and diffusion are not discussed.

5.3 Experimental

The experiments were performed in a Ga⁺ focused ion beam (FIB) plus scanning electron microscope (SEM) system (FEI STRATA DualBeam DB235). The metalorganic gas (CH₃)₃Pt(C_PCH₃)-CPC for short- was used as the precursor. The substrates were conducting Si wafers with or without a 30-nm-thick Cu-coating layer. The background pressure was 5.5×10^{-7} mbar and the pressure during growth was 3.3×10^{-6} mbar. A nozzle with a 400- μ m-diameter opening was located 450 μ m above the substrate surface and at an angle of 34°. To ensure a constant precursor gas supply during growth, the gas was introduced into the chamber 60 s before the ion beam. The distance between the nozzle and the impact site was the same for all growths. All the experiments were performed at room temperature. Patterns were deposited or milled using the Ga⁺ FIB with various ion incident angles (0°-45°) and ion energies (5-30 keV). In practice, we cannot get a good focused beam below 5 keV.

We shall describe the procedure of determining the deposition yield and the sputtering yield during IBID. First, a Pt box was deposited on a conducting Si substrate by IBID (Fig. 5.2a). After the precursor gas supply was switched off, a smaller box was milled by the ion beam inside the deposited box at the same beam conditions. The deposited thickness and the sputtered depth were measured by cross sectioning and subsequent SEM inspection. In order to avoid errors by the rounding of the top edge during sectioning, an EBID marker layer and an IBID protection layer were deposited on top before sectioning (Fig. 5.2b). The deposited Pt box meausred about $10\times10\mu m^2$ large and was at least 500 nm thick. The resolution of SEM imaging is 1-2 nm. Considering the contrast of the image of the marker layer and of the deposit-substrate boundary as well as the calibration of the SEM, we estimate the error in the yield measurements to be 3% - 5%. The composition of the deposits is measured by energy dispersive x-ray spectrometry (EDX).

The procedure to determine the yield and the energy spectrum of the secondary electrons during IBID is as follows. The ion current I_{pi} was measured by a Faraday cup. The sample current I during IBID was measured by a picoampere current meter

(Fig. 5.2d). By far, most of the sputtered particles are neutrals [135], so the contribution of secondary ions to the sample current is negligible. Thus, the secondary electron yield Y_{se} is $Y_{se}=(I-I_{pi})/I_{pi}$. With a positive bias ΔV between the substrate and the current meter, secondary electrons with energy below $e \cdot \Delta V$ are attracted back to the substrate, resulting in a reduced sample current I. A shielded box with six 1.5 V batteries was used to apply various biases between 0 and 9 V. Furthermore, the sample currents measured on bare Si and Cu-coated Si are the same, which confirms that the conductivity of Si is sufficiently high to avoid the additional sample charging.

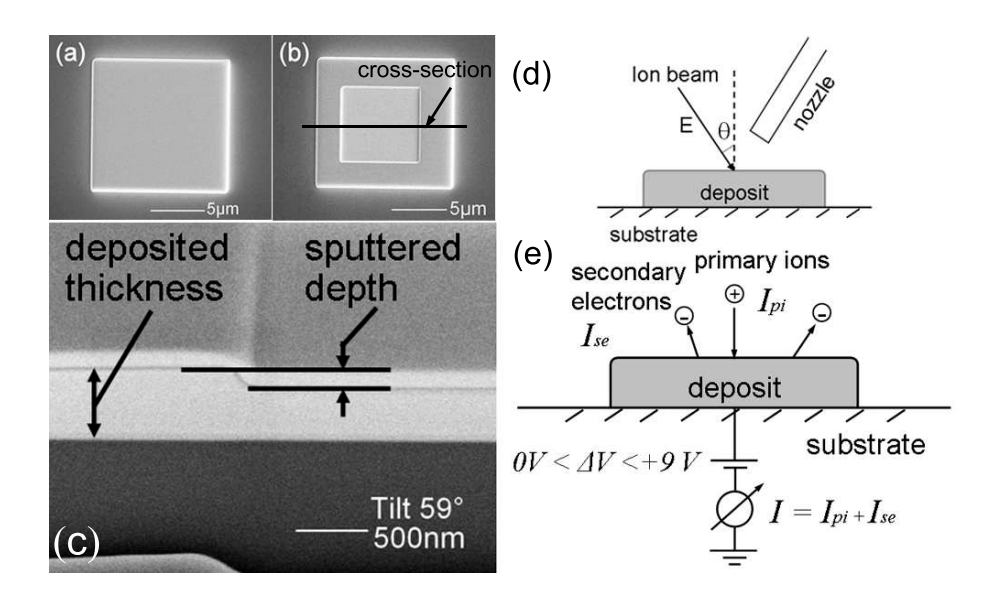


Figure 5.2: SEM top views and tilted view of (a) a Pt box grown by means of IBID. (b) The central part is removed by milling with the same FIB settings, then a marker layer is grown via EBID (black layer) plus an IBID protection layer. (c) Cross section (the cutting position is shown in (b)). (d) Sketch of the experimental setup with ion incident angle θ and energy E. (e) Measurement of the secondary electron current I_{se} and the energy spectrum of secondary electron with and without a positive bias ΔV .

5.4 Contributions of secondary particles in IBID mechanisms

It is well known that various secondary particles are produced during ion beam bombardment [167], including sputtered secondary atoms and emitted secondary electrons. Note that most of the sputtered secondary particles are neutral and very few are ionized. To investigate the contribution of secondary particles to IBID, we fabricated a special structure. A smooth wall was milled using FIB (Fig. 5.3a). Next, near the wall, a box was deposited by IBID with Ga⁺ FIB at normal incidence for 255 s. The energy and current were 30 keV and 1 pA, respectively. We note that the

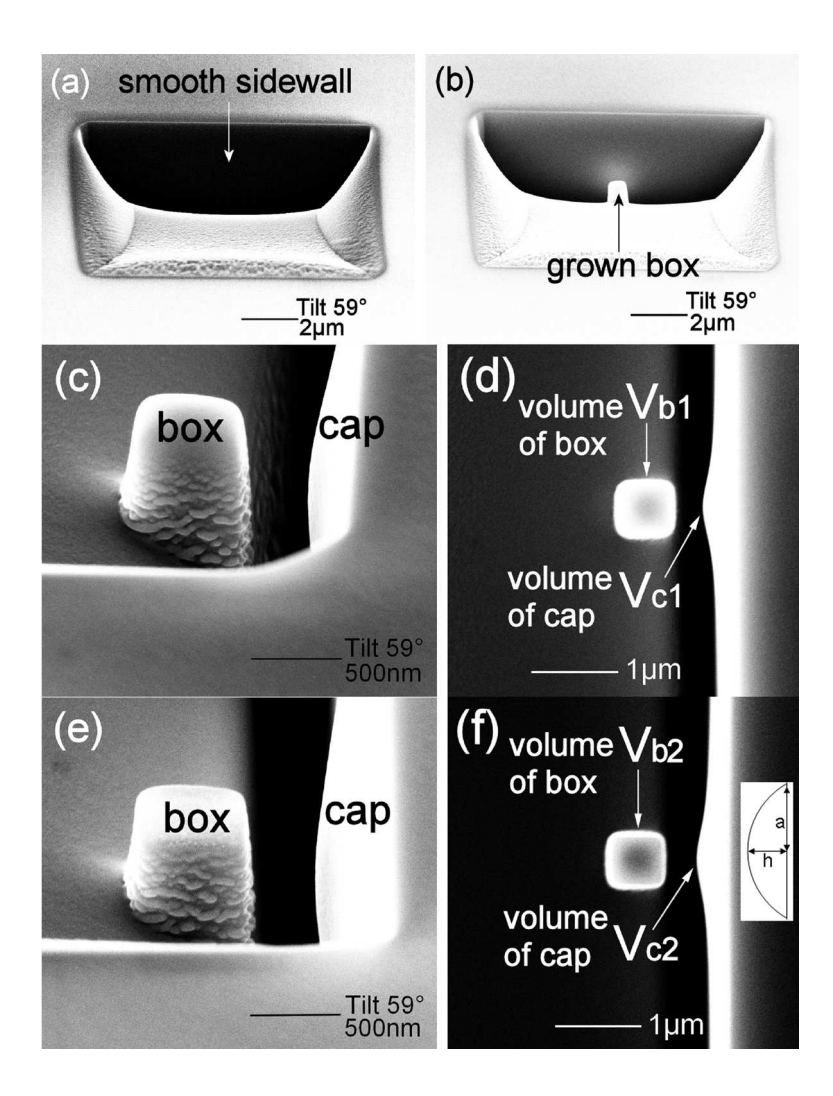


Figure 5.3: SEM images of (a) a smooth wall fabricated by FIB milling (b) a box deposited by IBID near wall, (c) sideview and (d) topview of box and a cap-shaped structure on sidewall, (e) sideview and (f) topview of box and cap after additional FIB milling.

volume of the box V_{b1} is the net deposited volume, which is equal to the deposited volume minus the sputtered volume. We saw that a cap-shaped structure had been growing on the wall during the deposition of the box (Fig. 5.3b-d). This cap layer originated from both the redeposition of sputtered particles [159] from the growing box and the precursor decomposition induced by sputtered particles and by emitted secondary electrons. Considering the short distance between the box to the wall (0.75 μm) and the height of the wall (3.2 μm), secondary particles emitted at an angle of at most 70° with respect to the surface can arrive at the wall. To estimate the redeposition contribution to the cap layer, the precursor gas was switched off after deposition. After the chamber pressure returned to the background, the deposited box was irradiated again with the same FIB setting for the same duration of 255 s (Fig. 5.3e-f). Because sputtering is caused mainly by ion-solid interactions, we assume that the gas absorption on the solid surface has little effect on the sputtering. Redeposition caused by sputtering is expected to remain the same with and without gas. Thus, we assume that during the second irradiation the redeposition onto the cap layer is equal to the redeposition during the first irradiation. This additional redeposition is equal to the difference in the volumes of the grown cap layer in Fig. 5.3 (f) and (d): $V_{c2}-V_{c1}$.

The contribution of secondary particles to IBID was determined by comparing the volume of the cap V_{c1} to that of the deposited box V_{b1} after correction for the volume of redeposition, which is equal to $V_{c2} - V_{c1}$.

$$\frac{V_{c1} - (V_{c2} - V_{c1})}{V_{b1}} \approx 17\% \tag{5.1}$$

The cap was assumed to be spherical for the volume calculation, $V = \pi h(3a^2 + h^2)/6$, where h is the height of the cap and a is the radius of the base of the cap. However, in this approach, we cannot separate the contributions of the secondary atoms and secondary electrons.

5.5 Roles of secondary electrons and sputtered atoms in IBID mechanisms

5.5.1 Incident ion energy and angular dependences of the yields of deposition, sputtering, and secondary electron emission during IBID

The experiments of current density dependence of the deposition yield are illustrated in Fig. 5.4. As expected, caused by ion-solid interaction, the sputtering yield Y_S is independent of the ion-beam current-density. The deposition yield decreases with increasing current density. At low current densities, the deposition yield is constant, otherwise it is a function of the precursor gas supply. To exclude the influence of this current density dependence or, in another words, to be sure the growth is in the ion-limited regime [188, 198, 270], a low ion current density of 0.5 pA/ μ m² was used in Figs. 5.5- 5.6 5.7 5.8. Accordingly, the ion current was 41 pA, the pixel dwell time

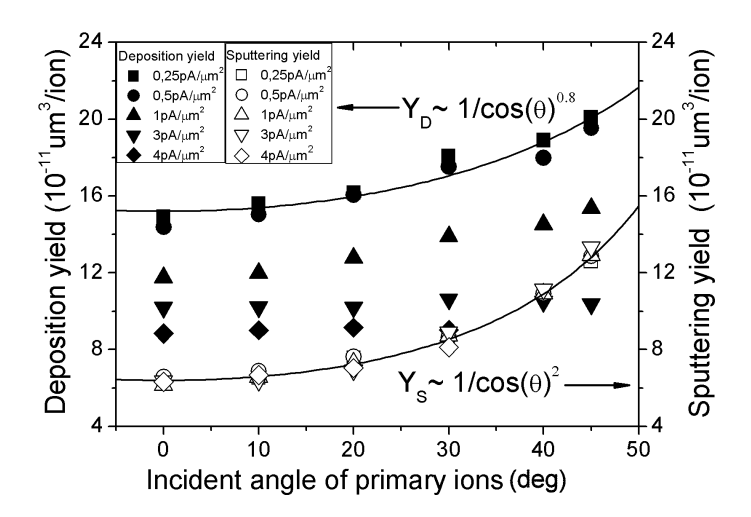


Figure 5.4: Current density dependence of the angular dependences of deposition yield and sputtering yield.

was $0.2 \mu s$ and the overlap was 0%.

The sputtering yield is assumed to be the same for bare deposit and the deposit covered by an adsorbed precursor layer. The deposition yield was defined by the measured net deposition yield plus the sputtering yield (Fig. 5.2a-c). Figure 5.5a shows the angular dependences of the yields of deposition Y_d , sputtering Y_s and secondary electron emission Y_{SE} for three different ion energies (5, 15, 30 keV). The deposition yield and the sputtering yield are expressed as volume per incident ion. The angular dependences are normalized at 0^o . One sees that the deposition yield has the same angular dependence as the secondary electron yield $(\cos\theta)^{-1.35}$, but a weaker dependence than that of the sputtering yield $(\cos\theta)^{-2.0}$. In Fig. 5.5b and c, the absolute deposition yield is plotted against the absolute yields of secondary electrons and sputtering, respectively. The deposition yield varies linearly with the sputtering yield having a slope of about 2.0 and an offset of about 0.09 nm³/ion. For constant ion energy, the deposition yield is proportional to the secondary electron yield. According to the EDX analysis, the composition of the deposit is $Ga_{0.15}Pt_{0.45}C_{0.40}$. We assume it has a typical atomic density of 100 atoms/nm³.

The normalized energy dependences of the yields of deposition Y_d , sputtering Y_s and secondary electron emission Y_{SE} at 0^o incidence are given in Fig. 5.6. The deposition yield decreases by 14%, with ion energy decreasing from 30 to 5 keV. The secondary electron yield decreases by 80%, whereas the sputtering yield decreases by 40%.

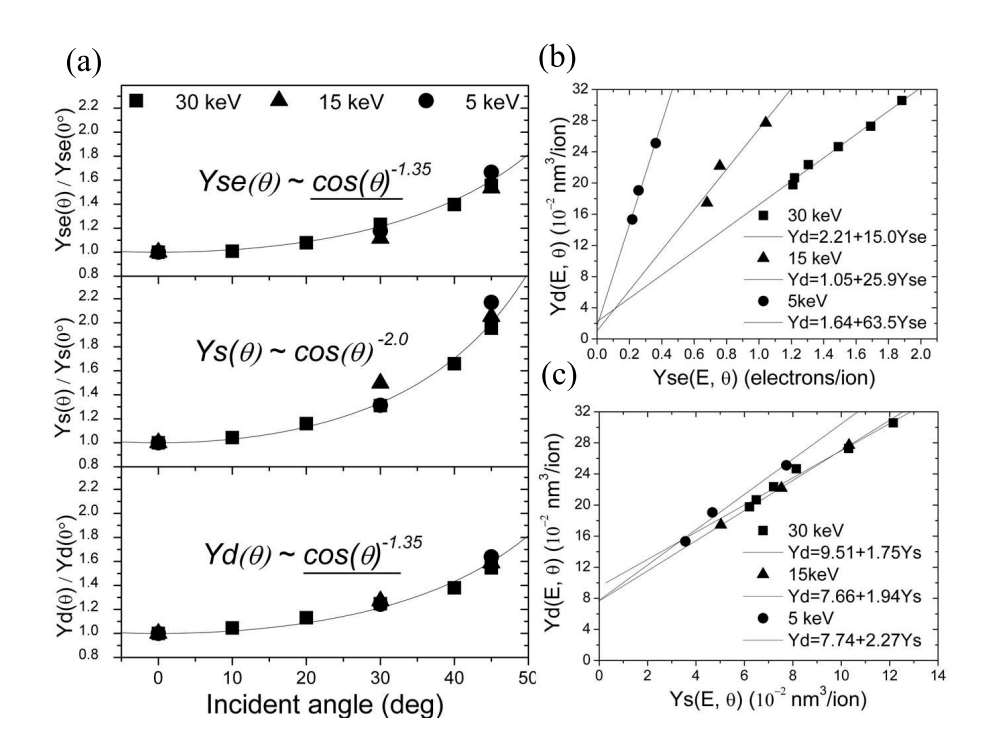


Figure 5.5: (a) Normalized secondary electron yield (Y_{SE}) , sputtering yield (Y_s) , and deposition yield (Y_d) as functions of the ion incident angle θ for three different ion energies E; (b) correlation between $Y_d(E, \theta)$ and $Y_{SE}(E, \theta)$); (c) correlation between $Y_d(E, \theta)$ and $Y_{SE}(E, \theta)$.

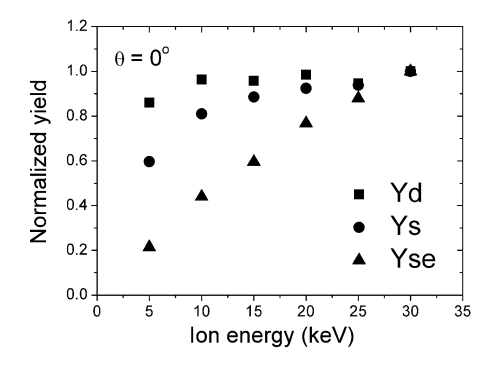


Figure 5.6: Normalized secondary electron yield (Y_{SE}) , sputtering yield (Y_s) , deposition yield (Y_d) as functions of ion energy E for an ion incident angle θ .

5.5.2 Incident ion energy and angular dependences of the energy spectrum of secondary electrons emitted during IBID

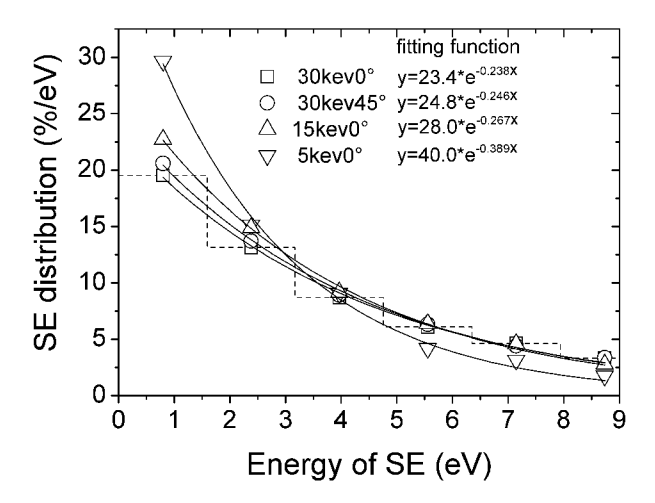


Figure 5.7: Observed energy spectra of secondary electrons (SE) during IBID for different ion incident angles and ion energies.

Figure 5.7 presents the energy spectra of secondary electrons in the range from 0 to 9.0 V in steps of 1.5 V (dash line). The secondary electron energy shown is the average energy of each energy step. The energy spectra are normalized to the same area. One sees that the energy spectra do not change with the ion incident angle. Furthermore, the lower energy part becomes more dominant with decreasing ion energy.

5.6 Contribution of primary ions in IBID mechanisms

By varying the Ga⁺ FIB current and the dwell time in spot mode, complex IBID shapes were obtained. At a relatively high current of 15 pA and at a shorter dwell time of 0.1 ms, a doughnut-like deposited structure with a central 30-nm-diameter tip was obtained (Fig. 5.8a,b). The exposure time was 20 s per spot. Furthermore, EDX results show that there is more Pt (30%) than Ga (10%) in our structures. Thus, it is unlikely that the central bright spot is due to the embedded Ga (Fig. 5.8a,b). At a longer dwell time of 1 ms but with the same exposure time, a 30-nm-diameter nanohole was obtained in the center of the deposited structure (Fig. 5.8c,d).

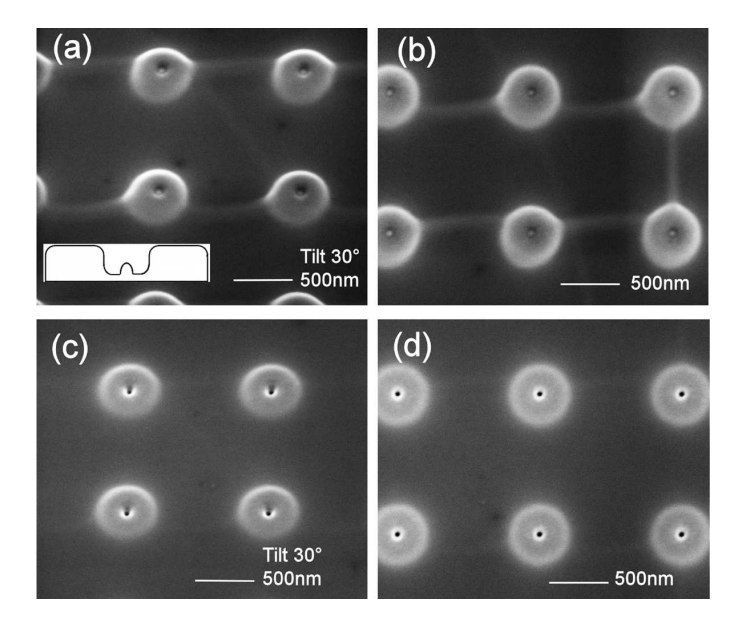


Figure 5.8: SEM images of doughnut-like structures grown in spot mode with 15 pA ion beam current (a,b) with a central tip (dwell time was 0.1 ms, exposure time was 20 s per spot); (c,d) with a central nanohole (dwell time was 1 ms, exposure time was 20 s per spot).

5.7 Discussion

The comparison of the volume of indirect deposition on the sidewall with that of direct deposition in Figure 5.3 shows that the contribution of secondary particles (atoms and electrons) is significant in IBID. If one takes all outward directions into account, the indirect deposition would be greater than $68\% = (4 \times 17\%)$ of the deposition at the irradiated area. Moreover, the distinct angular dependences of the deposition yield and the sputtering yield shown in Fig. 5.5 indicate that IBID cannot be explained solely in terms of ion-solid interactions (sputtering) as proposed by Dubner et al. [184–186].

The estimated diameter of a 15 pA ion beam is 13 nm, which is much smaller than the diameter of the doughnut-like structure of 440 nm (Fig. 5.8). Moreover, the deposited structure in this 440 nm region is not a thin layer. Thus, its large volume excludes the possibility that the doughnut-like structure is caused by the halo of the ion beam, because it is unlikely that there is such a large and intense halo. The central tip shown in Fig. 5.8, which grew at the site of incoming primary ions, suggests that primary ions also contribute to IBID. However, Shedd suggested that the primary ion contribution is small because of the low interaction cross section at the high primary ion energy [222]. To conclude, the results of this work indicate that different mechanisms are involved in IBID, and these mechanisms have their own

reaction zones.

The measured yields of sputtering, deposition and secondary electron emission increase with increasing incident angle and ion energy. These results are consistent with experimental [162, 168] and theoretical [165] work on sputtering, deposition [273, 274] and secondary electron emission [171, 173–179]. Moreover, the energy spectrum of the secondary electrons shifts slightly to higher energies with increasing ion energy, consistent with related studies [171, 180]. Here we will discuss our experimental results in light of the two models for IBID: the sputtered atom (atom-atom collision cascade) model [185, 186] and the secondary electron model [187].

We have observed a strong correlation between deposition and secondary electron emission: both exhibit the same dependences on ion incident angles. However, without detailed knowledge of the transport and interactions of primary ions, secondary atoms and secondary electrons, one cannot rule out the possibility that this observed proportionality is purely circumstantial. The proportionality between deposition yield and secondary electron emission depends strongly on the ion energy. For a density of 100 atoms/nm^3 several tens of precursor molecules are decomposed per secondary electron. This number is very high. If the secondary electron model for IBID is valid, secondary electrons must be more efficient in decomposing precursors molecules at low ion energies than at high ion energies. The measured difference is a factor of four between 5 and 30 keV ions (Fig. 5.5b). If true, the higher efficiency must be caused by the different characteristics of the secondary electrons plus the different responses of the precursor molecules to these different types of secondary electrons. Important characteristics are the angular and energy distributions of the emitted electrons. The measured energy spectra of the secondary electrons are indeed different, but the difference is small. Furthermore, decomposition in EBID is obviously caused by electrons, either primary or secondary (excluding decomposition by a thermal spike). Thus, if the secondary electron model is valid for IBID, strong similarities between EBID and IBID must exist. Little is known about precursor decomposition in EBID except that it depends on the primary or secondary electron energy [88, 275, 276]. Even if one assumes that only the very low-energy secondary electrons (<1.5 eV) decompose precursor molecules in EBID and IBID, their slightly higher relative intensity in our study (a factor of ~ 1.5 at 5 keV as compared to 30 keV) is insufficient to explain the observed fourfold efficiency. Therefore we conclude that the high deposition yield per secondary electron and its strong ion energy dependence are evidence against the validity of the secondary electron model for IBID.

The deposition yield and the sputtering yield have different angular dependences. However, all our data plotted together display a linear relationship between deposition and sputtering (Fig. 5.5c), independent of incidence angle and ion energy. Extrapolation of the measured relationship suggests that, in the limit of no sputtering, deposition is still possible. As Dubner et al. reported, the deposition yield is proportional to the nuclear stopping power [185, 186]. We note that from their work (Table II in [185]) for sputtering yields greater than 4 atoms/ion, a linear relationship with an offset between deposition and sputtering can be extracted (see Fig. 5.9). Even more interesting is the transition range for low sputtering yields. We did not observe

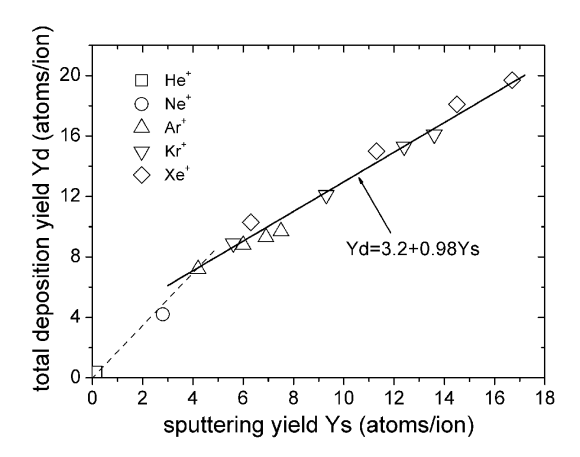


Figure 5.9: Relationship between deposition and sputtering using 2-10 keV He⁺, Ne⁺, Ar⁺, Kr⁺, Xe⁺ with $C_7H_7F_6O_2Au$ precursor gas. Data extracted from Table II in [185].

a similar transition in Fig. 5.5c because we could not make a well-focused ion beam with an energy of below $5~\rm keV$. The cause of the transition needs further investigation.

In summary, we conclude that the mechanism for Ga⁺ IBID is more likely linked to sputtering than to secondary electron emission.

5.8 Conclusions

Our investigations show that IBID is a very complex process. The additional deposition on a nearby sidewall clearly shows the contribution of secondary particles. In spot mode, the dependence of beam current and dwell time indicates that primary ions are also probably involved in IBID. The respective interactions of primary ions, secondary atoms, secondary electrons with the substrate, the deposited material, and the adsorbed precursor molecules determine the locally varying balances between material growth and material removal around the beam impact site. As a result, complex and useful shapes can be obtained by IBID with a proper choice of conditions. For instance, nanopores can be fabricated by IBID as discussed in the previous chapter.

The similar angular dependences of the deposition yield and the secondary electron yield support the secondary electron model. But the very different energy dependence and the high deposition yield (tens of atoms) per secondary electron defy this model. The deposition yield is linearly related to the sputtering yield with an offset, independent of the incident angle and the ion energy. This offset seems unphysical, but the data by Dubner et al. [185], see Fig. 5.9, suggest the existence of a

transition regime at low sputtering yields. From these observations we conclude that the sputtered-atom model describes more likely the dominant mechanism for Ga⁺ IBID than the secondary-electron model. A more detailed quantitative discussion requires additional experimental data, theory and modeling, but that is beyond the scope of the present dissertation.

Comparing our IBID results and the EBID results published in the open literature, we find that the deposition yield of Ga⁺ IBID is similar to that of He⁺ IBID [89, 226], and hundreds of times higher than that of EBID [88]. Nevertheless, the sputtering yield of Ga⁺ is much higher than that of He⁺ [88]. For instance, SRIM simulation shows that for Si the sputtering yield of 30 keV Ga⁺ (2.7 atoms/ion) is nearly 200 times higher than of He⁺ at the same energy. On the other hand, the secondary electron yields of Ga⁺ and He⁺ are similar, and hundreds of times higher than of electron beams [41, 88, 161, 277–281]. Moreover, for Ga⁺ bombardment of solids, the nuclear energy loss dominates [160], whereas for He⁺, the electronic energy loss dominates [160, 161]. These observations and considerations give rise to the following question: if sputtering plays an important role in Ga⁺ IBID, as we discussed in this chapter, does sputtering play an equally important role in He⁺ IBID?

To answer this question, we have to return to the basic principle of IBID: it is based on a dynamic balance between the supply and the consumption of ions and precursor molecules. In reality, at room temperature most IBID or EBID are carried out in a gas-limited condition [88]. Thus, the bottleneck in the dissociation lies in the supply of the precursor gas molecules, not of the energetic particles (primary ions or electrons, secondary atoms, ions or electrons) to the growth region. Particles with different energies have different dissociation cross sections. Generally, keV primary ions and primary electrons are considered to have much lower dissociation cross sections than 1-10 eV secondary particles [88, 275, 276]. Therefore, when several types of particles coexist during IBID or EBID, the ratios of their quantities and their respective dissociation cross sections determine which type of particle dominates the dissociation. Probably, different particles dominate in different situations. Secondary (sputtered) atoms dominate in Ga⁺ IBID, whereas secondary electrons dominate in He⁺ IBID and probably also in EBID [187, 227, 282, 283]. Nevertheless, the role of primary electrons in EBID [283, 284] cannot be ruled out as yet.

Summary

This thesis describes research work on a direct writing technology known as ion-beam-induced deposition (IBID). In IBID, precursor molecules adsorbed on a substrate surface are decomposed by an ion-beam induced reaction, resulting in localized material deposition. The work includes an exploration of the limits of IBID to fabricate nanopillars and nanopores in thin membranes, and a study of the IBID process mechanisms. Mainly the organometallic precursor gas $(CH_3)_3Pt(C_pCH_3)$ and either a conventional Ga^+ focused ion beam (FIB) or a novel FIB system with a focused He^+ beam were used. By virtue of its flexibility to deposit material locally as well as its high resolution, IBID is very suitable to prototype three-dimensional (3D) nanostructures.

This thesis demonstrates that at room temperature the resolution (the width) and the vertical growth rate of nanopillars fabricated by 1-pA, 30-keV Ga⁺ ions are about 140 nm and 20 nm/s, respectively. Under the same conditions, nanopillars fabricated by He⁺ IBID are 3-4 times narrower and 10 times taller than those fabricated by Ga⁺ IBID. He⁺ IBID results in a lower metal content (8-17%) than Ga⁺ IBID (35-45%). These differences can be attributed to the different projected ranges, lateral stragglings, and sputtering yields of Ga⁺ and He⁺ ions in the deposits. It is found that the dimension and the shape of IBID nanopillars are influenced by the precursor surface density and the ion-beam current. The width of the IBID nanopillars decreases with increasing precursor surface density and decreasing ion-beam current. This behavior reveals a complex interplay between the vertical and the lateral growth of the nanopillars; in particular, growth rates for these two directions respond differently on changes in e.g. precursor depletion and replenishment.

Furthermore, we study the formation of the irregularities on the pillar's sidewall and the deposits around the base of Ga⁺ IBID nanopillars (halos). Nanopillars grown on an insulating substrate have smoother sidewalls and smaller halos than those on a conductive substrate. An explanation might be that there is an effect of the charged surface on the secondary electron emission or on the movement of the polarized or charged precursor molecules or their fragments. Correspondingly, the irregularities on the sidewalls might be caused by either secondary electron emission during IBID or by roughening related to sputtering. The latter mechanism is more likely as the irregularities on the sidewall are absent in He⁺ IBID, in which the secondary electron yield is similar and the sputtering yield is much lower than in Ga⁺ IBID. The halo

might be caused by the scattering secondary particles from the growing pillar. The proximity effect for Ga⁺ and He⁺ nanopillar array growth during IBID has been studied as well. On a Si substrate, proximity effects are observed for Ga⁺ or He⁺ nanopillar growth when pillar separation is less than 3 μ m or 500 nm, respectively. This proximity effect can be explained by the scattering of incident ions and secondary particles, or by changes in the precursor supply or the conductivity of the substrate.

Furthermore, this thesis demonstrates that one can fabricate sub-10-nm-diameter nanopores in a 45-nm-thick $\mathrm{Si_3N_4}$ membrane in a single $\mathrm{Ga^+}$ IBID step by carefully adjusting the ion beam and gas exposure conditions. The successful fabrication of negative patterns by a deposition technology is explained by the competition between sputtering and deposition during IBID. We also study the chemical composition and the shape of pores at various stages of pore formation, which are the deciding factors with regard to the functionalization of nanopores. It is found that the chemical structure in the rim of the pore depends on the type of precursor gas.

In addition, this thesis aims to distinguish the roles of different mechanisms involved in the Ga⁺ IBID process. Firstly, a significant contribution of secondary particles in Ga⁺ IBID has been demonstrated. Then two models, which describe IBID in terms of the impact of secondary electrons and of sputtered atoms, respectively, have been investigated. The results indicate that for the case of Ga⁺ the sputtered-atom-model describes IBID better than the secondary-electron-model. Finally, a review of the studies on the mechanisms of Ga⁺ and He⁺ IBID and on the mechanisms of EBID (electron-beam-induced deposition) published in the literature is given. It reveals that IBID has to be explained by multiple mechanisms. Probably, different mechanisms dominate in different situations: secondary (sputtered) atoms dominate in Ga⁺ IBID, whereas secondary electrons dominate in He⁺ IBID and in EBID.

Samenvatting

Dit proefschrift bevat een studie naar een technologie voor direct-write, namelijk ionenbundel-geïnduceerde depositie (IBID). Bij IBID worden op een substraatoppervlak geadsorbeerde moleculen ontleed in een ionenbundel-geïnduceerde reactie, wat leidt tot lokale neerslag (depositie) van materiaal. Dit werk is zowel een verkennning van de grenzen van IBID voor de vervaardiging van (nano-)pilaren en (nano-)poriën in membranen, als een studie naar de mechanismen van IBID. Hoofdzakelijk werden het organometallische precursor gas $(CH_3)_3Pt(C_pCH_3)$ en een conventionele Ga^+ gefocuseerde ionenbundel (FIB) of een nieuwe He^+ FIB gebruikt. Dankzij de hoge flexibiliteit in het lokaal deponeren van materiaal en de hoge ruimtelijke precisie is IBID uitermate geschikt voor het vervaardigen van prototypen van driedimensionale (3D) nanostructuren.

Het proefschrift toont aan dat met een 1 pA en 30 keV Ga⁺ bundel de ruimtelijke precisie (resolutie) en de groeisnelheid voor nanopilaren bij kamertemperatuur respektievelijk ongeveer 140 nm en 20 nm/s zijn. Onder dezelfde omstandigheden zijn nanopilaren die met He⁺ IBID worden gegroeid drie tot vier keer zo smal en tien keer zo hoog. De He⁺ IBID pilaren hebben echter een lager metaalgehalte (8-17%) dan de Ga⁺ IBID pilaren (35-45%). Deze verschillen worden toegekend aan de verschillen in indringdiepte, verstrooiing en verstuiving van Ga⁺ en He⁺ ionen in de deposieten. Er werd tevens gevonden dat de grootte en vorm van de IBID nanopilaren bepaald worden door de oppervlaktedichtheid van de geadsorbeerde precursor moleculen en door de bundelstroom. De breedte van Ga-IBID pilaren neemt af bij toenemende dichtheid en afnemende bundelstroom. Dit gedrag wijst op een ingewikkeld samenspel tussen de groei van de pilaren in de hoogte en in de breedte. Beide groeiwijzes reageren bijvoorbeeld verschillend op veranderingen in uitputting of verversing van de precursor moleculen.

Daarnaast hebben we de onregelmatigheden op de zijkanten van en depositie ('halo's') rondom de Ga⁺ IBID nanopilaren onderzocht. Nanopilaren gegroeid op een isolerende ondergrond hebben gladdere zijkanten en kleinere halo's dan die op een geleidende ondergrond. Een verklaring hiervoor kan het effect zijn van het geladen oppervlak op de secundaire-elektronenemissie of op de beweging van gepolariseerde of geladen precursor moleculen of hun fragmenten. Evenzo vermoeden we dat de onregelmatigheden op de zijkanten worden veroorzaakt door secundaire-elektronenemissie of door verruwing tijdens verstuiving. Het tweede mechanisme lijkt

het meest waarschijnlijke omdat oppervlakteonregelmatigheden afwezig zijn bij He⁺ IBID, waarbij secundaire-elektronenemissie evengroot maar verstuiving veel geringer is dan bij Ga⁺ IBID. De halo's worden waarschijnlijk veroorzaakt door de verstrooiïng van secundaire deeltjes uit de groeiende pilaren. Ook het proximity-effect tijdens Ga⁺ en He⁺ pilaargroei is bestudeerd. Proximity-effecten op een silicium
ondergrond zijn zichtbaar wanneer de afstand tussen de pilaren minder is dan 3 μ m (bij Ga⁺ IBID) of 500 nm (bij He⁺ IBID). Het proximity-effect kan worden verklaard als gevolg van de verstrooiïng van invallende ionen of secundaire deeltjes of van veranderingen in de precursoraanvoer of de geleidbaarheid van de ondergrond.

Het proefschrift toont bovendien aan dat men sub-tien-nanometer poriën in 45-nanometer dikke siliciumnitride membranen kan maken met één enkele Ga⁺ IBID processtap. Dit is mogelijk door zorgvuldig de ionenbundel- en gastoevoeromstandigheden op elkaar af te stemmen. De mogelijkheid 'negatieve' patronen te maken met een depositieproces wordt verklaard aan de hand van de competitie tussen verstuiving en depositie tijdens IBID. Ook de chemische samenstelling rondom en de vorm van de poriën hebben we bestudeerd tijdens verschillende stadia van de vervaardiging. Vorm en samenstelling bepalen immers de mogelijke functionalisatie van de nanoporiën. We vonden dat de chemische structuur van de rand van de porie afhangt van de aard van het precursor gas. Uiteindelijk poogt dit proefschrift de rol van verschillende IBID-mechanismes te onderscheiden. Allereerst wordt een aanzienlijke bijdrage van secundaire deeltjes aangetoond. Daarna worden twee modellen onderzocht die IBID verklaren vanuit respectievelijk secundaire elektronen en verstoven atomen. De resultaten tonen aan dat het verstoven-atomenmodel Ga⁺ IBID beter beschrijft dan het secundaire-elektronenmodel. Tenslotte volgt een bespreking van de gepubliceerde studies over de mechanismes van Ga⁺ en He⁺ IBID en van elektronenbundel-geïnduceerde depositie (EBID). De bespreking laat zien dat IBID verklaard moet worden vanuit meerdere tegelijk werkzame mechanismes. Klaarblijkelijk hebben verschillende mechanismes de overhand in verschillende situaties: verstoven atomen domineren in Ga⁺ IBID en secundaire elektronen in He⁺ IBID en in EBID.

Bibliography

- [1] Taniguchi, N. On the basic concept of "Nanotechnology". Proc. Intl. Conf. Prod. Eng., Japan Society of Precision Engineering (1974).
- [2] Feynman, R. There is plenty of room at the bottom. Engineering and Science magazine, vol. XXIII, no. 5, February 1960 XXIII, 5 (1960).
- [3] International technology roadmap for semiconductors 2005. Tech. Rep. (2005).
- [4] Cui, Z. Nanofabrication: Principles, Capabilities and Limits (Springer, 2008).
- [5] Pease, R. F. & Chou, S. Y. Lithography and other patterning techniques for future electronics. *Proc. of the IEEE* **96**, 248 (2008).
- [6] Harriott, L. R. Limits of lithography. Proc. of the IEEE 89, 366 (2001).
- [7] Schift, H. Nanoimprint lithography: An old story in modern times? A review. J. Vac. Sci. Technol. 26, 458 (2008).
- [8] Wu, B. & Kumar, A. Extreme ultraviolet lithography: A review. J. Vac. Sci. Technol. B 25, 1743 (2007).
- [9] Nakayama, Y., Okazaki, S. & Saitou, N. Electron-beam cell projection lithography: A new high-throughput electron-beam direct-writing technology using a speciality trailored Si aperture. J. Vac. Sci. Technol. 8, 1836 (1990).
- [10] Berger, S. D. & Gibson, J. M. New approach to projection-electron lithography with demonstrated 0.1μ linewidth. *Appl. Phys. Lett.* **57**, 153 (1990).
- [11] Pfeiffer, H. C. & Stickel, W. PREVAIL- an e-beam stepper with variable axis immersion lenses. *Microelectron. Eng.* 27, 143 (1995).
- [12] Yamabe, M. Status and issues of electron projection lithography. J. Microlith., Microfab., Microsyst. 4, 011005 (2005).
- [13] Tseng, A. A. Recent development in nanofabrication using ion projection lithography. Small 1, 594 (2005).
- [14] Gross, G. Ion projection lithography: Next generation technology. J. Vac. Sci. Technol. 15, 2136 (1997).

- [15] Gross, G., Kaesmaier, R., Löschner, H. & Stengl, G. Ion projection lithography: status of the MEDEA project and United States/European cooperation. *J. Vac. Sci. Technol.* **16**, 3150 (1998).
- [16] Kaesmaier, R., Löschner, H., Stengl, G., Wolfe, J. C. & Ruchhoeft, P. Ion projection lithography: international development program. J. Vac. Sci. Technol. 17, 3091 (1999).
- [17] Melngailis, J. A review of ion projection lithography. J. Vac. Sci. Technol. 16, 927 (1998).
- [18] Stengl, G., Löschner, H., Maurer, W. & Wolf, P. Ion projection lithography machine IPLM-01: a new tool for sub-0.5-micron modification of materials. J. Vac. Sci. Technol. B 4, 194 (1986).
- [19] Lee, Y. et al. Axial energy spread measurements of an accelerated positive ion beam. Nucl. Instrum. Methods Phys. Res. A 385 (1997) 385, 204 (1997).
- [20] Bruenger, W. H. et al. Resolution improvement of ion projector with a low energy spread muticusp ion source. *Microelectron. Eng.* 46, 477 (1999).
- [21] Hirscher, S. et al. Ion projection lithography below 70 nm: tool performance and resist process. *Microelectron. Eng.* **61-62**, 301 (2002).
- [22] International technology roadmap for semiconductors 2003. Tech. Rep. (2003).
- [23] Chou, S. Y., Krauss, P. R. & Renstrom, P. J. Imprint of sub-25 nm vias and trenches in polymers. *Appl. Phys. Lett.* **67**, 3114 (1995).
- [24] Chou, S. Y., Krauss, P. R. & Renstrom, P. J. Imprint lithography with 25-nanometer resolution. *Science* **272**, 85 (1996).
- [25] Chou, S. Y., Krauss, P. R. & Renstrom, P. J. Imprint lithography with 25nanometer resolution. J. Vac. Sci. Technol. 14, 4129 (1996).
- [26] Haisma, J., Verheijen, M., van den Heuvel, K. & van den Berg, J. Mold-assisted nanolithography: A process for reliable pattern replication. J. Vac. Sci. Technol. 14, 4124 (1996).
- [27] Chou, S. Y., Krauss, P. R., Zhang, W., Guo, L. & Zhuang, L. Sub-10 nm imprint lithography and applications. J. Vac. Sci. Technol. 15, 2897 (1997).
- [28] Kuwabara, K. & Miyauchi, A. High-aspect-ratio nanopillar structures fabricated by nanoimprinting with elongation phenomenon. J. Vac. Sci. Technol. 26, 582 (2008).
- [29] Mayadas, A. F. & Laibowitz, R. B. One-dimensional superconductors. Phys. Rev. Lett. 28, 156 (1971).
- [30] Yamazaki, K. & Namatsu, H. 5-nm-order eletron-beam lithography for nanode-vice fabrication. *Jpn. J. Appl. Phys.* **43**, 3767 (2004).

- [31] Grigorescu, A. E., van der Kropt, M. C. & Hagen, C. W. Limiting factors for electron beam lithography when using ultra-thin hydrogen silsesquioxane layers. J. Micro/Nanolith. MEMS MOEMS 6, 043006 (2007).
- [32] Seliger, R. L., Ward, J. W., Wang, V. & Kubena, R. L. A high-intensity scanning ion probe with submicrometer spot size. *Appl. Phys. Lett.* **34**, 310 (1979).
- [33] Prewett, P. D., Mair, G. L. R. & Thompson, S. P. Some comments on the mechanism of emission from liquid metal ion sources. *J. Appl. Phys. D* **15**, 1339 (1982).
- [34] Swanson, L. W. Liquid metal ion sources: mechanism and applications. Nucl. Instr. and Meth. in Phys. Res. 218, 347 (1983).
- [35] Melngailis, J. Focused ion beam lithography. Nucl. Instr. and Meth. in Phys. Res. B 80-81, 1271 (1993).
- [36] Gierak, J. et al. Sub-5 nm FIB direct patterning of nanodevices. Microelectron. Eng. 84, 779 (2007).
- [37] Ryssel, H., Haberger, K. & Kranz, H. Ion-beam sensitivity of polymer resists. J. Vac. Sci. Tech. 19, 1358 (1981).
- [38] Karapiperis, L., Adesida, I., Lee, C. A. & Wolf, E. D. Ion beam exposure profiles in pmma-computer simulation. J. Vac. Sci. Technol. 19, 1259 (1981).
- [39] Kubena, R. L., Ward, J. W., Stratton, F. P., Joyce, R. J. & Atkinson, G. M. A low magnification focused ion beam system with 8 nm spot size. J. Vac. Sci. Technol. B 9, 3079 (1991).
- [40] Kubena, R. L. et al. Dot lithography for zero-dimensional quantum wells using focused ion beams. J. Vac. Sci. Technol. B 6, 353 (1988).
- [41] Morgan, J., Notte, J., Hill, R. & Ward, B. An introduction to the helium ion microscope. *Microscopy Today* **14**, 24 (2006).
- [42] Sidorkin, V. et al. Sub-10-nm nanolithography with a scanning helium beam. J. Vac. Sci. Technol. B 27, L18 (2008).
- [43] Kruit, P. High throughput electron lithography with the multiple aperture pixel by pixel enhancement of resolution concept. J. Vac. Sci. Technol. B 16, 3177 (1998).
- [44] Kampherbeek, B. J., Wieland, M. J., van Zuuk, A. & Kruit, P. An experimental setup to test the MAPPER electron lithography concept. *Microelectron. Eng.* 53, 279 (2000).
- [45] Slot, E. et al. MAPPER: high throughput maskless lithography. Proc. SPIE 6921, 69211P (2008).
- [46] Brandstatter, C. et al. Projection maskless lithography. Proc. SPIE 5374, 601 (2004).

- [47] Kapl, S. E. et al. Projection mask-less lithography (PML2): first results from the multi beam demonstrator. *Microelectron. Eng.* 83, 968 (2006).
- [48] Klein, C. *et al.* Projection maskless lithography (PML2): proof-of-concept setup and first experimental results. *Proc. SPIE* **6921**, 69211O (2008).
- [49] URL http://www.mapperlithography.com/press-en-2007.html.
- [50] Platzgummer, E., Loeschner, H. & Gross, G. Projection maskless patterning (PMLP) for the fabrication of leading-edge complex masks and nano-imprint templates. *Proc. SPIE* **6730**, 673033 (2007).
- [51] Platzgummer, E., Loeschner, H. & Gross, G. Projection maskless patterning for nanotechnology applications. J. Vac. Sci. Technol. B 26, 2059 (2008).
- [52] Binnig, G., Rohrer, H., Gerber, C. & Weibei, E. Tunneling through a controllable vacuum gap. *App. Phys. Lett.* **40**, 178 (1982).
- [53] Binnig, G., Rohrer, H., Gerber, C. & Weibei, E. Surface studies by scanning tunneling microscope. *Phys. Rev. Lett.* **49**, 57 (1982).
- [54] Pohl, D. W., Denk, W. & Lanz, M. Optical stethoscopy: Image recording with resolution $\lambda/20$. App. Phys. Lett. 44, 651 (1984).
- [55] Ringger, M., Hidber, H. R., Schlögl, R., Oelhafen, P. & Güntherodt, H. J. Nanometer lithography with the scanning tunneling microscope. Appl. Phys. Lett. 46, 832 (1985).
- [56] Tseng, A. A., Notargiacomo, A. & Chen, T. P. Nanofabrication by scanning probe microscope lithography: A review. J. Vac. Sci. Technol. B 23, 877 (2005).
- [57] Gates, B. D. *et al.* New approaches to nanofabrication: modeling, printing, and other techniques. *Chem. Rev.* **105**, 1171 (2005).
- [58] Eigler, D. M. & Schweizer, E. K. Positioning single atoms with a scanning tunneling microscope. *Nature* **344**, 524 (1990).
- [59] Crommie, M. F., Lutz, C. P. & Eiger, D. M. Confinement of electrons to quantum corrals on a metal surface. *Science* 262, 218 (1993).
- [60] McCord, M. A. & Pease, R. F. W. Lift-off metallization using poly(methyl methacrylate) exposed with a scanning tunneling microscope. J. Vac. Sci. Technol. B 6, 293 (1988).
- [61] Marrian, C. R. K. & Dobisz, E. A. Electron-beam lithography with the scanning tunneling microscope. J. Vac. Sci. Technol. B 10, 2877 (1992).
- [62] Majumdar, A., Oden, P. I. & Carrejo, J. P. Nanometer-scale lithography using the atomic force microscope. Appl. Phys. Lett. 61, 2293 (1992).
- [63] Royer, P., Brachiesi, D., Lerondel, G. & Bachelot, R. Near-field optical patterning and structuring based on local-field enhancement at the extremity of a metal tip. *Phil. Trans. R. Soc. Lond. A* 362, 821 (2004).

- [64] Dagata, J. A. et al. Modification of hydrogen-passivated silicon by a scanning tunneling microscope operating in air. Appl. Phys. Lett. **56**, 2001 (1990).
- [65] Avouris, P., Hertel, T. & Martel, R. Atomic force microscope tip-induced local oxidation of silicon: kinetics, mechanism, and nanofabrication. *Appl. Phys.* Lett. 71, 285 (1997).
- [66] Keyser, U. F., Schumacher, H. W., Zeitler, U. & Haug, R. J. Fabrication of a single-electron transistor by current-controlled local oxidation of a twodimensional electron system. Appl. Phys. Lett. 76, 457 (2000).
- [67] Matsumoto, K., Gotoh, Y., Maeda, T., Dagata, J. A. & Harris, J. S. Room-temperature single-electron memory made by pulse-mode atomic force microscopy nano oxidation process on atomically flat α -alumina substrate. *Appl. Phys. Lett.* **76**, 239 (2000).
- [68] Mamin, H. J., Chiang, S., Birk, H., Guethner, P. H. & Rugar, D. Gold deposition from a scanning tunneling microscope tip. J. Vac. Sci. Technol. B 9, 1398 (1991).
- [69] Houel, A., Tonneau, D., Bonnail, N., Dallaporta, H. & Safarov, V. I. Direct patterning of nanostructures by field-induced deposition from a scanning tunneling microscope tip. J. Vac. Sci. Technol. B 20, 2337 (2002).
- [70] Rauscher, H., Behrendt, F. & Behm, R. J. Fabrication of surface nanostructures by scanning tunneling microscope induced decomposition of (sih)₄ and (sih)₂Cl₂. J. Vac. Sci. Technol. B **15**, 1373 (1997).
- [71] Piner, R. D., Zhu, J., Xu, F., Hong, S. H. & Mirkin, C. A. "Dip-pen" nanolithography. Science 283, 661 (1999).
- [72] Basnar, B. & Willner, I. Dip-pen-nanolithographic patterning of metallic, semconductor, and metal oxide nanostructures on surfaces. *Small* 5, 28 (2009).
- [73] Rosa, L. G. & Liang, J. Atomic force microscope nanolithography: dip-pen, nanoshaving, nanografting, tapping mode, electrochemical and thermal nanolithography. *J. Phys.:Condens. Matter* **21**, 483001 (2009).
- [74] Salaita, K., Wang, Y. & Mirkin, C. A. Application of dip-pen nanolithography. Nature Nanotechnol. 2, 145 (2007).
- [75] Zhang, M. et al. A MEMS nanoplotter with high-density parallel dip-pen nanolithography probe arrays. Nanotechnol. 13, 212 (2002).
- [76] Ye, J. H., Murano, F. P., Barniol, N., Abadal, G. & Aymerich, X. Local modification of n-Si(100) surface in aqueous solutions under anodic and cathodic potential polarization with an in situ scanning tunneling microscope. *J. Vac. Sci. Technol. B* 13, 1423 (1995).
- [77] Nagahara, L. A., Thundat, T. & Lindsay, S. M. Nanolithography on semi-conductor surfaces under an etching solution. *Appl. Phys. Lett.* **57**, 270 (1990).

- [78] Kondo, S., Heike, S., Lutwyche, M. & Wada, Y. Surface modification mechanism of materials with scanning tunneling microscope. *J. Appl. Phys.* **78**, 155 (1995).
- [79] Li, Y. Z., Vazquez, L., Piner, R., Andres, R. P. & Reifenberger, R. Writing nanometer-scale symbols in gold using the scanning tunneling microscope. *Appl. Phys. Lett.* **54**, 1424 (1989).
- [80] Müller, M. et al. Controlled structuring of mica surfaces with the tip of an atomic force microscope by mechanically induced local etching. Surf. Interface Anal. 36, 189 (2004).
- [81] Stewart, R. L. Insulating films formed under electron and ion bombardment. Phys. Rev. 45, 488 (1934).
- [82] Watson, J. H. L. An effect of electron bombardment upon carbon black. J. App. Phys. 18, 153 (1947).
- [83] Cosslett, V. E. Particle "growth" in the electron microscope. J. App. Phys. 18, 844 (1947).
- [84] Hillier, J. On the investigation of specimen contamination in the electron microscope. J. App. Phys. 19, 226 (1948).
- [85] Christy, R. W. Formation of thin polymer films by electron bombardment. J. App. Phys. 31, 1680 (1960).
- [86] Möller, W., Pfeiffer, T. & Schluckebier, M. Carbon buildup by ion-induced polymerization under 100-400 kev H, He, and Li bombardment. *Nucl. Instr.* and Meth. 182-183, 297 (1981).
- [87] Gamo, K., Takakura, N., Samoto, N., Shimizu, R. & Namba, S. Ion beam assited deposition of metal organic films using focused ion beams:. *Jpn. J. Appl. Phys.* 23, L293 (1984).
- [88] Utke, I., Hoffmann, P. & Melngailis, J. Gas-assisted focused electron beam and ion beam processing and fabrication. *J. Vac. Sci. Technol. B* **26**, 1197 (2008).
- [89] Sanford, C. A. et al. Beam induced deposition of platinum using a helium ion microscope. J. Vac. Sci. Technol. B 27, 2660 (2009).
- [90] Botman, A. P. J. M. Towards high purity nanostructures from electron beam induced deposition of platinum. Ph.D. thesis, Delft University of Technology (2009).
- [91] van Dorp, W. F., van Someren, B., Hagen, C. W., KruitP, P. & Crozier, A. Approaching the resolution limites of nanometer-scale electron beam-induced deposition. *Nano. Lett.* 5, 1303 (2005).
- [92] van Dorp, W. F., van Someren, B., Hagen, C. W., KruitP, P. & Crozier, A. Statistical variation analysis of sub-5-nm-sized electron-beam-induced deposits. J. Vac. Sci. Technol. B 24, 618 (2006).

- [93] van Dorp, W., Hagen, C., Crozier, P., van Someren, B. & Kruit, P. One nanometer structure fabrication using electron beam induced deposition. *Microelectron. Eng.* 83, 1468 (2006).
- [94] Shimojo, M. et al. Selective growth and characterization of nanostructures with transmission electron microscopes. Appl. Surf. Sci. 241, 56 (2005).
- [95] Tanaka, M., Shimojo, M., Han, M., Mitsuishi, K. & Furuya, K. Ultimate sized nano-dots formed by electron beam-induced deposition using an ultrahigh vacuum transmission electron microscope. *Surf. Interface Anal.* **37**, 261 (2005).
- [96] Shimojo, M., Mitsuishi, K., Tanaka, M., Han, M. & Furuya, K. Application of transmission electron microscopes to nanometre-sized fabrication by means of electron beam-induced deposition. *J. Microsc.* **214**, 76 (2004).
- [97] Tanaka, M., Shimojo, M., Mitsuishi, K. & Furuya, K. The size dependence of the nano-dots formed by electron-beam-induced deposition on the partial pressure of the precursor. *Appl. Phys. A.* **78**, 543 (2004).
- [98] Guise, O. & Ahner, J. Formation and thermal stability of sub-10-nm carbon templates on Si(100). *Appl. Phys. Lett.* **85**, 2352 (2004).
- [99] Silvis-Cividjian, N., Hagen, C. W., Kruit, P., v.d. Stam, M. A. J. & Groen, H. B. Direct fabrication of nanowires in an electron microscope. *Appl. Phys. Lett.* 82, 3514 (2003).
- [100] Mitsuishi, K., Shimojo, M., Han, M. & Furuya, K. Electron-beam-induced deposition using a subnanometer-sized probe of high-energy electrons. *Appl. Phys. Lett.* 83, 2064 (2003).
- [101] Ochiai, Y., Baba, M., Watanabe, H. & Matsui, S. Ten-nanometer resolution nanolithography using newly developed 50-kv electron beam direct writing system. *Jpn. J. Appl. Phys.* **30**, 3266 (1991).
- [102] van Dorp, W., Hagen, C., Crozier, P. & Kruit, P. Growth behavior near the ultimate resolution of nanometer-scale focused electron beam-induced deposition. Nanotechnol. 19, 225305 (2008).
- [103] van Kouwen, L., Botman, A. & Hagen, C. W. Focused electron-beam-induced deposition of 3 nm dots in a scanning electron microscope. *Nano. Lett.* 9, 2149 (2009).
- [104] Silvis-Cividjian, N., Hagen, C. W. & Kruit, P. Spatial resolution limits in electron-beam-induced deposition. *J. App. Phys.* **98**, 084905 (2005).
- [105] Fujita, J. et al. Carbon nanopillar laterally grown with electron beam-induced chemical vapor deposition. J. Vac. Sci. Technol. B 21, 2990 (2003).
- [106] Botman, A., Mulders, J. J. & Hagen, C. W. Creating pure nanostructures from electron-beam-induced deposition using purification techniques: a technology perspective. *Nanotechnol.* 20, 372001 (2009).

- [107] FEI manual of STRATA DualBeam DB235 (xp Workstation User's Guide and Rference Guide.
- [108] Wagner, A. et al. X-ray mask repair with focused ion beam. J. Vac. Sci. Technol. B 8, 1557 (1990).
- [109] van Dorp, W. F. Sub-10 nm focused electron beam induced deposition. Ph.D. thesis, Delft University of Technology (2008).
- [110] Igaki, J. et al. Comparison of FIB-CVD and EB-CVD growth characteristics. Microelectron. Eng. 83, 1225 (2006).
- [111] Okada, S. et al. Growth manner and mechanical characteristics of amorphous carbon nanopillars grown by electron-beam-induced chemical vapor depoisition. Jpn. J. Appl. Phys. 44, 5646 (2005).
- [112] Okada, S. et al. Comparison of Young's modulus dependency on beam accelerating voltage between electron-beam- and focused ion-beam-induced chemical vapor deposition pillars. Jpn. J. Appl. Phys. 45, 5556 (2006).
- [113] Matsui, S. et al. Three-dimensional nanostructure fabrication by focused-ion-beam chemical vapor deposition. J. Vac. Sci. Technol. B 18, 3181 (2000).
- [114] Hoshino, T. et al. Development of three-dimensional pattern-generating system for focused-ion-beam chemical-vapor depoisition. J. Vac. Sci. Technol. B 21, 2732 (2003).
- [115] Morita, T., Kometani, R., Watanabe, K. & Kanda, K. Free-space-wiring fabrication in nano-space by focused-ion-beam chemical vapor deposition. *J. Vac. Sci. Technol. B* **21**, 2737 (2003).
- [116] Igaki, J. et al. Mechanical characteristics and applications of diamondlikecarbon cantilevers fabricated by focused-ion-beam chemical vapor deposition. J. Vac. Sci. Technol. B 24, 2911 (2006).
- [117] Ozasa, A. et al. Fabrication and evaluation of thermal nano-sensor by focused-ion-beam chemical-vapor-deposition. In 17th International Microprocesses and Nanotechnology Conference, Osaka, Japan (2004).
- [118] Igaki, J. et al. Three-dimensional rotor fabrication by focused-ion-beam chemical-vapor-deposition. *Microelectron. Eng.* **83**, 1221 (2006).
- [119] Kometani, R. et al. Performance of nanomanipulator fabricated on glass capillary by focused-ion-beam chemical vapor deposition. J. Vac. Sci. Technol. B 23, 298 (2005).
- [120] Kometani, R. et al. Charateristics of nano-electrostatic actuator fabricated by focused ion beam chemical vapor deposition. Jpn. J. Appl. Phys. 43, 7187 (2004).
- [121] Kometani, R. et al. Nozzle-nanostructure fabrication on glass capillary by focused-ion-beam chemical vapor deposition and etching. Jpn. J. Appl. Phys. 42, 4107 (2003).

- [122] Kometani, R. et al. Three-dimensional high-performance nano-tools fabricated using focused-ion-beam chemical-vapor- deposition. Nucl. Instr. and Meth. in Phys. Res. B 232, 362 (2005).
- [123] Kometani, R. et al. Cell wall cutting tool and nano-net fabrication by FIB-CVD for subcellular operations and analysis. *Microelectron. Eng.* 83, 1642 (2006).
- [124] Kometani, R. et al. Evaluation of a bio nano-sensing proble fabricated by focused-ion-beam chemical vapor deposition for single organelle analyses. Jpn. J. Appl. Phys. 46, 7963 (2007).
- [125] Kometani, R., Haruyama, Y., Kanda, K., Kaito, T. & Matsui, S. Evaluation of vacuum microcapsule fabricated using Focused-Ion-Beam Chemical-Vapor-Deposition. *Jpn. J. Appl. Phys.* **46**, L180 (2006).
- [126] Fujita, J. et al. Iinducing graphite tube tranformation with liquid gallium and flash discharge. App. Phys. Lett. 88, 083109 (2006).
- [127] Kometani, R., Kanda, K., Haruyama, Y., Kaito, T. & Matsui, S. Evaluation of field electron emitter fabricated using focused-ion-beam chemical vapor deposition. Jpn. J. Appl. Phys. 45, L711 (2006).
- [128] Kometani, R., Haruyama, Y., Kanda, K., Kaito, T. & Matsui, S. Relationship between field emission properties and material characteristics of diamond-like carbon fabricated by focused-ion-beam chemical vapor deposition. *Jpn. J. Appl. Phys.* 46, 7987 (2007).
- [129] Xu, Q. Y., Kageyama, Y. & Suzuki, T. Novel fabrication method of IBICVD for FePt and CoPt particles. *IEEE transactions on magnetics* **41**, 3379 (2005).
- [130] Xu, Q. Y., Kageyama, Y. & Suzuki, T. Ion-beam-induced chemical-vapor deposition of FePt and CoPt particles. J. App. Phys. 97, 10K308 (2005).
- [131] Lapicki, A., Kang, K. & Suzuki, T. Fabrication of magnetic dot arrays by ion beam induced chemical vapor deposition (IBICVD). *IEEE transactions on* magnetics 38, 2589 (2002).
- [132] Lapicki, A., Kang, K. & Suzuki, T. Ion beam induced chemical vapor deposition (IBICVD) of cobalt particles. *J. Magn. Magn. Mater.* **240**, 47 (2002).
- [133] Kasumov, A. Y. *et al.* Proximity effect in a superconductor-metallofullerene-superconductor molecular junction. *Phys. Rev. B* **72**, 033414 (2005).
- [134] Shigeto, K. et al. Reproducible formation of nanoscale-gap electrodes for single-molecule measurements by combination of fib deposition and tunneling current detection. Microelectron. Eng. 83, 1471 (2006).
- [135] Orloff, J., Utlaut, M. & Swanson, L. High resolution focused ion beam: FIB and its application—The physics of liquid metal ion sources and ion optics and their application to focused ion beam technology (Kluwer Academic/Plenum Publishers, 2003).

- [136] Müller, E. W. Das feldionenmikroskop. Z. Physik 131, 136 (1951).
- [137] Müller, E. W. & Bahadur, K. Field ionization of gases at a metal surface and the resolution of the field ion microscope. *Phys. Rev.* **102**, 624 (1956).
- [138] Müller, E. W. Study of atomic structure of metal surfaces in the field ion microscope. J. Appl. Phys. 28, 1 (1957).
- [139] Gomer, R. A. Field emission and field ionziation (Harvard University Press, 1961).
- [140] Müller, E. W. & Tsong, T. T. Field ion microcopy principles and applications (American Elsevier Publishing Company, 1969).
- [141] Escovitz, W., Fox, T. & Levi-Setti, R. Metaphase chromosomes in the scanning proton microscope. *Proc. 23nd Ann. Mtg. Elect. Mic. Soc. America* **23**, 304 (1975).
- [142] Escovitz, W., Fox, T. & Levi-Setti, R. Scanning transmission ion microscopy with a field ionization source. *Proc. Nat. Acad. Sci.* **72**, 1826 (1975).
- [143] Levi-Setti, R. Proton scanning microscopy: feasiblity and promise. *Scanning Electron Microscopy* 125 (1974).
- [144] Orloff, J. & Swanson, L. W. Study of a field-ionization source for microprobe applications. J. Vac. Sci. Technol. 12, 1209 (1975).
- [145] Orloff, J. & Swanson, L. W. A scanning ion microscope with a field ionization source. *Scanning Electron Microscopy* 1, 57 (1977).
- [146] Orloff, J. & Swanson, L. W. Fine-focus ion beams with field ionization source. J. Vac. Sci. Technol. 15, 845 (1978).
- [147] Orloff, J. & Swanson, L. W. Angular intensity of a gas-phase field ionization source. J. Appl. Phys. **50**, 6026 (1979).
- [148] Scipioni, L., Stern, L. A. & Notte, J. Applications of the helium ion microscope. Microscopy Today 15, 12 (2007).
- [149] Scipioni, L., Stern, L. A., Notte, J., Sijbrandij, S. & Griffin, B. Helium ion microscope. Adv. Mater & Proc. 166, 27 (2008).
- [150] Ward, B. W., Notte, J. A. & Economou, N. P. Helium ion microscope: A new tool for nanoscale microscopy and metrology. J. Vac. Sci. Technol. B 24, 2871 (2006).
- [151] Taylor, G. I. Disintegration of water drops in an electri field. Proc. Royal Soc. London A 280, 383 (1964).
- [152] Driesel, W., Dietzsch, C. & Mühle, R. In-situ observation of the tip shape of AuGe liquid alloy sources using a high voltage transmission electron microscope. J. Vac. Sci. Technol. B 14, 3367 (1996).

- [153] Melngailis, J. Focused ion beam technology and applications. *J. Vac. Sci. Technol. B* **5**, 469 (1987).
- [154] Ward, J. W. A Monte Carlo calculation of the virtual source size for a liquid metal ion source. J. Vac. Sci. Technol. B 3, 207 (1985).
- [155] Callegari, V. & Nellen, P. M. Spontaneous growth of uniformly distributed in nanodots and ini₃ nanowires on InP induced by a focused ion beam. *Phys. Stat.* Sol. A 204, 1665 (2007).
- [156] J.Bi, de Jager, P. W. H., Barth, J. E. & Kruit, P. Influence of Coulomb interactions on current density distribution in a two-lens focused ion beam system. *Microelectronic Engineering* 41/42, 1998, 249-252 41-42, 249 (1998).
- [157] Ward, J. W., Kubena, R. L. & Utlaut, M. W. Transverse thermal velocity broadening of focused beams from liquid metal ion sources. J. Vac. Sci. Technol. B 6, 2090 (1988).
- [158] Fredili, V. & Utke, I. Optimized molecule supply from nozzle-based gas injection systems for focused electron- and ion-beam induced deposition and etching: simulation and experiment. *J. Phys. D: Appl. Phys.* **42**, 125305 (2009).
- [159] Giannuzzi, L. A. & Stevie, F. A. Introduction of focused ion beams (Springer, 2005).
- [160] Ziegler, J. F. SRIM-2003. Nucl. Instr. and Meth. in Phys. Res. 219, 1027 (2004).
- [161] Ramachandra, R., Griffin, B. & Joy, D. A model of secondary electron imaging in the helium ion scanning microscope. *Ultramicroscopy* **109**, 748 (2009).
- [162] Benninghoven, A., Rüdenauer, F. G. & Werner, H. W. Secondary ion mass spectrometry (Wiley, 1987).
- [163] Ziegler, J. F., Biersack, J. P. & Littmark, U. The Stopping and Range of Ions in Solids (New York: Pergamon, 1985).
- [164] Andersen, H. H. & Bay, H. L. Sputtering-yield studies on silicon and silver targets. Radiation Effects 19, 139 (1973).
- [165] Sigmund, P. Sputtering by particle bombardment I (Springer, 1981).
- [166] Sigmund, P. Theory of sputtering i: sputtering yield of amporphous and polycrytalline targets. *Phys. Rev. B* **184**, 383 (1969).
- [167] Carter, G. & Colligon, J. S. Ion bombardment of solids (Heinemann, 1968).
- [168] Andersen, H. H. & Bay, H. L. Sputtering by particle bombardment I (Springer, 1981).
- [169] Sigmund, P. Inelastic Ion-Surface Collision (Academic Press, 1977).
- [170] Baragiola, R. A. Principles and mechanisms of ion induced electron emission. Nucl. Instr. and Meth. in Phys. Res. B 78, 223 (1993).

- [171] Brusilovsky, B. A. Kinetic ion-induced electron emission from the surface of random solids. *App. Phys. A* **50**, 111 (1990).
- [172] Schou, J. Ttransport theory of kinetic emission of secondary electrons from solids. *Phys. Rev. B* **22**, 2141 (1980).
- [173] Krása, J., Láska, L., Stockli, M. P. & Fry, D. Electron yield per ion charge-state correction for an ion collector with unsuppressed secondary electron emission. *Czechoslovak J. of Phys.* **50**, 797 (2000).
- [174] Zalm, P. C. & Beckers, L. J. Ion-induced secondary electron emission from copper and zinc. Surf. Sci. 152-153, 135 (1985).
- [175] von Gemmingen, U. Ion induced secondary electron emission from single crystal surfaces. Surf. Sci. 120, 334 (1982).
- [176] Svenssen, B. & Holmen, G. Electron emission from ion-bombarded aluminum. J. App. Phys. **52**, 6928 (1981).
- [177] Svenssen, B., Holmen, G. & Buren, A. Angular dependence of the ion-induced secondary-electron yield from solids. *Phys. Rev. B* **24**, 3749 (1981).
- [178] Klein, H. J. Ausbeuten und winkelverteilungen der durch edelgasionen an reinen wolframoberflächen ausgelösten sekundärelektronen. Z. Phys. 188, 78 (1965).
- [179] Jonker, J. L. H. Philips Res. Rep. 6, 372 (1951).
- [180] Rudd, M. E. Energy and angular distributions of secondary electrons from 5-100-keV-proton collisions with hydrogen and nitrogen molecules. *Phys. Rev. A* **20**, 787 (1979).
- [181] Li, W. & Joy, D. C. Study of temperature influence on electron beam induced deposition. J. Vac. Sci. Technol. A 24, 431 (2006).
- [182] Smith, D. A., Fowlkes, J. D. & Rack, P. D. Simulating the effects of surface diffusion on electron beam induced deposition via a three-dimensional Monte Carlo simulation. *Nanotechnol.* **19**, 415704 (2008).
- [183] Utke, I., Friedli, V., Purrucker, M. & Michler, J. Resolution in focused electronand ion-beam induced processing. *J. Vac. Sci. Technol. B* **25**, 2219 (2007).
- [184] Dubner, A. D. & Wagner, A. Mechanism of ion beam induced deposition of gold. J. Vac. Sci. Technol. B 7, 1950 (1989).
- [185] Dubner, A. D., Wagner, A., Melngailis, J. & Thompson, C. V. The role of the ion-solid interaction in ion-beam-induced deposition of gold. J. App. Phy. 70, 665 (1991).
- [186] Ro, J. S., Thompson, C. V. & Melngailis, J. Mechanism of ion beam induced deposition of gold. J. Vac. Sci. Technol. B 12, 73 (1994).
- [187] Lipp, S. et al. A comparsion of focused ion beam and electron beam induced deposition process. *Microelectron. Reliab.* **36**, 1779 (1996).

- [188] Chen, P., Salemink, H. W. M. & Alkemade, P. F. A. The complex mechanisms of ion-beam-induced deposition. *Jpn. J. Appl. Phys.* 47, 5123 (2008).
- [189] Petzold, H. C. & Heard, P. J. Ion-induced deposition for x-ray mask repair: rate optimization using a time-dependent model. *J. Vac. Sci. Technol. B* **9**, 2664 (1991).
- [190] Blauner, P. G., Ro, J. S., Butt, Y. & Melngailis, J. Focused ion beam fabrication of submicron gold structures. J. Vac. Sci. Technol. B 7, 609 (1989).
- [191] Hoyle, P. C., Cleaver, J. R. A. & Ahmed, H. Electrical resistance of electron beam induced depoisits from tungsten hexacarbonyl. Appl. Phys. Lett. 64, 1448 (1994).
- [192] Botman, A., de Winter, M. & Mulders, J. J. L. Electron-beam-induced deposition of platinum at low landing energies. J. Vac. Sci. Technol. B 26, 2460 (2008).
- [193] van Dorp, W. F. Private communication.
- [194] Mezhenny, S., Lyubinetsky, I., Choyke, W. J. & Yates, J. T. Electron stimuated decomposition of adsorbed hexafluoroacetylacetonate, Cu (I) vinyltrimethylsilane, Cu (I)(hfac)(vtms). J. App. Phys. 85, 3368 (1999).
- [195] Bell, D. C. Contrast mechanisms and image formation in helium ion microscopy. *Micros. Microanal.* 15, 147 (2009).
- [196] Choi, Y. R., Rack, P. D., Randolph, S. J., Smith, D. A. & Joy, D. C. Pressure effect of growing with electron beam-induced deposition with tungsten hexafluoride and tetraethylorthosilicate precursor. *Scanning* **28**, 311 (2006).
- [197] Wang, S., Sun, Y.-M., Wang, Q. & White, J. M. Electron-beam induced initial growth of platinum films using Pt(PF₃)₄. J. Vac. Sci. Technol. B **22**, 1803 (2004).
- [198] Chiang, T. P., Sawin, H. H. & Thompson, C. V. Surface kinetic study of ion-beam-induced chemical vapor deposition of copper for focused ion beam applications. J. Vac. Sci. Technol. A 15, 3104 (1997).
- [199] Dubner, A. D. & Wagner, A. The role of gas adsorption in ion-beam-induced deposition of gold. J. Appl. Phys. 66, 870 (1989).
- [200] Matsui, S., Ichihashi, T. & Mito, M. Electron beam induced selective etching and deposition technology. J. Vac. Sci. Technol. B 7, 1182 (1989).
- [201] Koops, H. W. P., Weiel, R. & Kern, D. P. High-resolution electron-beam induced deposition. J. Vac. Sci. Technol. B 6, 477 (1988).
- [202] Matsui, S. & Mori, K. New selective depoisition technology by electron beam induced surface reaction. J. Vac. Sci. Technol. B 4, 299 (1986).
- [203] Fowlkes, J. D. & Rack, P. D. Fundamental electron-precursor-solid interaction derived from time-dependent electron-beam-induced deposition simulations and experiments. J. Vac. Sci. Technol. B 4, 1619 (2010).

- [204] Plank, H., Gspan, C., Dienstleder, M., Kothleitner, G. & Hofer, F. The influence of beam defocus on volume growth rates for electron beam induced platinum deposition. *Nanotechnol.* 19, 485302 (2008).
- [205] von Platen, K. T. K., Buchmann, L.-M., Petzold, H. C. & Brünger, W. H. Electron-beam induced tungsten deposition: Growth rate enhancement and applications in microelectronics. J. Vac. Sci. Technol. B 10, 2690 (1992).
- [206] Smith, D. A., Fowlkes, J. D. & Rack, P. D. Understanding the kinetics and nanoscale morphology of Electron-Beam-Induced Deposition via a three-dimensional Monte Carlo simulation: The effects of the precursor molecule and the deposited material. *Small* 4, 1382 (2008).
- [207] Smith, D. A., Fowlkes, J. D. & Rack, P. D. A nanoscale three-dimensional Monte Carlo simulation of electron-beam-induced deposition with gas dynamics. *Nanotechnol.* 18, 265308 (2007).
- [208] Lobo, C. J., Toth, M., Wagner, R., Thiel, B. L. & Lysaght, M. High resolution radially symmetric nanostructures from simultaneous electron beam induced etching and deposition. *Nanotechnol.* **19**, 025303 (2008).
- [209] Chen, P., Salemink, H. W. M. & Alkemade, P. F. A. Smooth and narrow nanopillars fabricated by ion-beam-induced deposition under charging conditions. *Jpn. J. Appl. Phys.* 47, 8120 (2008).
- [210] Fujita, J. et al. Sstructure and resonant characteristics of amorphous carbon pillars grown by focused-ion-beam-indeued chemical vapor deposition. Jpn. J. Appl. Phys. 41, 4423 (2002).
- [211] Fujita, J. et al. Graphitization of Fe-doped amporphous carbon pillars grown by focused-ion-beam-indcued chemical-vapor deposition. J. Vac. Sci. Technol. B 20, 2686 (2002).
- [212] Vladár, A. E., Postek, M. T. & Ming, B. On the sub-nanometer resolution of scanning electron and helium ion microscopes. *Microscopy Today* **17**, 6 (2009).
- [213] Hill, R., Notte, J. & Ward, B. The ALIS He ion source and its application to high resolution microscopy. *Physics Procedia* 1, 135 (2008).
- [214] Sidorkin, V. et al. Sub-10-nm nanolithography with a scanning helium beam. J. Vac. Sci. Technol. B 27, L18 (2009).
- [215] Weber, M., Koops, H. W. P., Rudolph, M., Kretz, J. & Schmidt, G. New compound quantum dot materials produced by electron-beam induced depoisition. J. Vac. Sci. Technol. B 13, 1364 (1995).
- [216] Lau, Y. M., Chee, P. C., Thong, J. T. & Ng, V. Properties and applications of cobalt-based material produced by electron-beam-induced deposition. J. Vac. Sci. Technol. A 20, 1295 (2002).
- [217] Utke, I. et al. Thermal effects during focused electron beam induced deposition of nanocomposite magnetic-cobalt-containing tips. Microelectron. Eng. 73-74, 553 (2004).

- [218] Utke, I. et al. Cross section investigations of compositions and sub-structures of tips obtained by focused electron beam induced deposition. Adv. Eng. Mater. 7, 323 (2005).
- [219] Utke, I., Luisier, A., Hoffmann, P., Laub, D. & Buffat, P. A. Focused-electron-beam-induced deposition of freestanding three-dimensional nanostructures of pure coalesced copper crystals. *App. Phys. Lett.* **81**, 3245 (2002).
- [220] Bret, T., Utke, I., Hoffmann, P., Abourida, M. & Doppelt, P. Electron range effects in focused electron beam induced deposition of 3D nanostructures. *Mi-croelectron. Eng.* 83, 1482 (2006).
- [221] Ishida, M. et al. Focused ion beam-induced fabrication of tungsten structures. J. Vac. Sci. Technol. B 21, 2728 (2003).
- [222] Shedd, G. M., Lezec, H., Dubner, A. D. & Melngailis, J. Focused ion beam induced deposition of gold. Appl. Phys. Lett. 49, 1584 (1986).
- [223] Shuman, R., Sundaram, G., Lezec, H. J. & Bromley-Barratt, J. In 12th Int. Microprocesses and Nanotechnology Conf. (1999).
- [224] Kislov, N. A. & Khodos, I. I. Direct electron-beam-induced formation of nanometer-scale carbon structures in STEM. *Microsc. Microanal. Microstruct.* 3, 323 (1992).
- [225] Mitsuishi, K., Shimojo, M., Takeguchi, M., Tanaka, M. & Furuya, K. Proximity effect in electron-beam-induced deposition. *Jpn. J. Appl. Phys.* 45, 5517 (2006).
- [226] Chen, P., Salemink, H. W. M. & Alkemade, P. F. A. Roles of secondary electrons and sputtered atoms in ion-beam-induced deposition. *J. Vac. Sci. Technol. B* **27**, 2718 (2009).
- [227] Silvis-Cividjian, N., Hagen, C. W., Leunissen, L. H. A. & Kruit, P. The role of secondary electrons in electron-beam-induced-deposition spatial resolution. *Microelectron. Eng.* **61-62**, 693 (2002).
- [228] Randolph, S. J., Fowlkes, J. D. & Rack, P. D. Effects of heat generation during electron-beam-induced deposition of nanostructures. J. of Appl. Phys. 97, 124312 (2005).
- [229] Steckelmacher, W. Molecular flow conductance of long tubes with uniform elliptical cross-section and the effect of different cross-sectional shapes. *J. Phys. D: Appl. Phys.* 11, 473 (1978).
- [230] Puretz, J. & Swanson, L. W. Focused ion beam deposition of pt containing films. J. Vac. Sci. Technol. B 10, 2695 (1992).
- [231] Friedli, V. Focused electron- and ion- beam induced processes: in situ monitoring, analysis and modeling. Ph.D. thesis, école polytechnique fédérale de lausanne (2008).
- [232] Wilson, R. G., Stevie, F. A. & Magee, C. W. Secondary ion mass spectrometry (Wiley, 1989).

- [233] Dietze, L. A. & Sheffield, J. C. Secondary electron emission induced by 5-30 kev monatomic ions striking thin oxide films. *J. Appl. Phys.* **46**, 4361 (1975).
- [234] Wittmaack, K. Ion-induced electron emission as a means of studying energyand angle-dependent compositional changes of solids bombarded with reactive ions I. Oxygen bombardment of silicon. *Surf. Sci.* **419**, 249 (1999).
- [235] Wittmaack, K. Electron emission and ion reflection from Mg, Aland Si bombarded with 1-10 kev O⁺ and Ne⁺ at impact angles between 0° and 84°. *Nucl. Instr. and Meth. in Phys. Res. B* **115**, 288 (1996).
- [236] Wittmaack, K. Energy dependence of ion induced electron yields of aluminium and silicon bombarded with Ne⁺, O⁺, andO₂⁺. Nucl. Instr. and Meth. in Phys. Res. B **58**, 317 (1991).
- [237] Banhart, F. Laplacian growth of amorphous carbon filaments in a non-diffusion-limited experiment. *Phys. Rev. E* **52**, 5156 (1995).
- [238] Zhang, J. Z., Ye, X. Y., Yang, X. J. & Liu, D. Fabrication of self-standing nanowires, nanodendrites, and nanofractal-like trees on insulator substrates with an electron-beam-induced deposition. *Phys. Rev. E* **55**, 5796 (1997).
- [239] Wang, H. Z., Liu, X. H., Yang, X. J. & Wang, X. Intergrowth of a carbon layer and fractal-like trees on 3Y-TZP in TEM observations. *Mater. Sci. Eng. A* 311, 180 (2001).
- [240] Song, M. et al. Fabrication of self-standing nanowires, nanodendrites, and nanofractal-like trees on insulator substrates with an electron-beam-induced deposition. Appl. Phys. A 80, 1431 (2005).
- [241] Xie, G., Song, M., Mitsuishi, K. & Furuya, K. Fabrication and characterization of self-standing W-nanodendrites on insulator SiO₂ substrate by electron-beam-induced deposition under HVTEM. *Jpn. J. Appl. Phys.* 44, 5654 (2005).
- [242] Gnaser, H. Sputtering by particle bombardment (Springer, 2007).
- [243] DeMarco, A. J. & Melngailis, J. Lateral growth of focused ion beam deposited platinum for stencil mask repair. J. Vac. Sci. Technol. B 17, 3154 (1999).
- [244] Bret, T., Utke, I. & Hoffmann, P. Influence of the beam scan direction during focused electron beam induced deposition of 3D nanostructures. *Microelectron*. Eng. 78-79, 307 (2005).
- [245] Gibbon, D. J. Handbook of Vacuum Physics (Pergamon, 1966).
- [246] Dekker, C. Solid-state nanopores. Nat. Nanotechnol. 2, 209 (2007).
- [247] Rhee, M. & Burns, M. A. Nanopore sequencing technology: nanopore preparations. *Trends Biotechnol.* **25**, 174 (2007).
- [248] Zhou, C., Deshpande, M. R. & Reed, M. A. Nanoscale metal/self-assembled monolayer/metal heterostructures. *App. Phys. Lett.* **71**, 611 (1997).

- [249] Ralph, D. C., Black, C. T. & Tinkham, M. Spectroscopic measurements of discrete electronic states in single metal particles. *Phys. Rev. Lett.* 74, 3241 (1995).
- [250] Ralls, K. S., Buhrman, R. A. & Tiberio, R. C. Fabrication of thin-film metal nanobridges. *Appl. Phys. Lett.* **55**, 2459 (1989).
- [251] Wei, H. X., Langford, R. M., Han, X. & Coey, J. M. D. Controlled fabrication of nickel perpendicular nanocontacts using focused ion beam milling. *J. App. Phys.* 99, 08C501 (2005).
- [252] Krapt, D. et al. Fabrication and characterizaition of nanopore-based electrodes with radii down to 2 nm. Nano. Lett. 6, 105 (2006).
- [253] Keyser, U. F. et al. Nanopore tomography of a laser focus. Nano. Lett. 5, 2253 (2005).
- [254] Patterson, N. et al. Controlled fabrication of nanopores using a direct focused ion beam approach with back face particle detection. nanotechnology 19, 235304 (2008).
- [255] Tong, H. D. et al. Silicon nitride nanosieve membrane. Nano. Lett. 4, 283 (2004).
- [256] Li, J. et al. Ion-beam sculpting at nanometre length scales. Nature 412, 166 (2001).
- [257] Storm, A. J., Chen, J. H., X. S. Ling, H. W. Z. & Dekker, C. Fabrication of solid-state nanopores with single-nanometre precision. *Nat. Mater.* 2, 537 (2003).
- [258] Lo, C. J., Aref, T. & Bezryadin, A. Fabrication of symmetric sub-5 nm nanopores using focused ion and eletron beams. *nanotechnology* **17**, 3264 (2006).
- [259] Biance, A. L. et al. Focused ion beam sculpted membranes for nanoscience tooling. *Microelectron. Eng.* 83, 1474 (2006).
- [260] Chang, H. et al. Fabrication and characterization of solid-state nanopores using a field emission scanning electron microscope. Appl. Phys. Lett. 88, 103109 (2006).
- [261] Wu, S. S., Park, S. R. & Ling, X. S. Lithography-free formation of nanopores in plastic membranes using laser heating. *Nano. Lett.* 6, 2571 (2006).
- [262] Wu, M. Y., Krapt, D., Zandbergen, M. & Zandbergen, H. Formation of nanopores in a SiN/Sio₂membrane with an electron beam. Appl. Phys. Lett. 87, 113106 (2005).
- [263] Schenkel, T., Radmilovic, V., Stach, E. A., Park, S. J. & Persaud, A. Formation of a few nanometer wide holes in membranes with a dual beam focused ion beam system. *J. Vac. Sci. Technol. B* **21**, 2720 (2003).

- [264] Allen, F. I. et al. Transport of multiply and highly charged ions through nanoscale apertures in silicon nitride membranes. Nucl. Instr. and Meth. in Phys. Res. B 244, 323 (2006).
- [265] Nilsson, J., Lee, J. R. I., Ratto, T. V. & Létant, S. E. Localized funcationalization of single nanopores. *Adv. Mater.* **18**, 427 (2006).
- [266] Danelon, C., Santschi, C., Brugger, J. & Vogel, H. Fabrication and funcationalization of nanochannels by electron-beam-induced silicon oxide depoisition. Langmuir 22, 10711 (2006).
- [267] Chen, P. et al. Atomic layer depoisiton to fine-tune the surface properties and diameters of fabricated nanopores. Nano. Lett. 4, 1333 (2004).
- [268] Chen, P. et al. Probing single DNA molecule transport using fabricated nanopores. Nano. Lett. 4, 2293 (2004).
- [269] Kremer, J. R., Mastronarde, D. N. & McIntosh, J. R. Computer visualization of three-dimensional image data using imod. *J. Struct. Biol.* **116**, 71 (1996).
- [270] Dubner, A. D. & Wagner, A. In-situ measurement of ion-beam-induced deposition of gold. J. App. Phy. 65, 3636 (1989).
- [271] Tanaka, M., Furuya, K. & Saito, T. In-situ observation of focused ion beam micropatterns on semiconductors and insulators. J. Jpn. J. Appl. Phys. 37, 7010 (1998).
- [272] Selman, G. L., Ellison, P. J. & Darling, A. S. Carbon in platinum and palladium solubility determinations and diffusion at high temperatures. *Platinum Metals Rev.* 14, 14 (1970).
- [273] Langford, R. M., Wang, T.-X. & Ozkaya, D. Reducing the resisitivity of electron and ion beam assited depsited Pt. *Microelectron. Eng.* 84, 784 (2007).
- [274] Teresa, J. M. D. et al. Origin of the difference in the resisitivity of as-grown focused-ion- and focused-electron-beam-induced Pt nanodeposits. J. Nanomater. 2009, 936863 (2009).
- [275] Cosby, P. C. Electron-impact dissociation of carbon monoxide. *J. Chem. Phys.* **98**, 7804 (1993).
- [276] Winters, H. F. & Inokuti, M. Total dissociation cross section of CF₄ and other fluoroalkanes for electron impact. *Phys. Rev. A* **25**, 1420 (1982).
- [277] Ramachandra, R., Griffin, B. J. & Joy, D. A study of helium ion induced secondary electron emission. *Microsc. Microanal.* **14**, 1192 (2008).
- [278] Hasselkamp, D., Hippler, S., Scharmann, A. & Schmehl, T. Electron emission from clean solid surfaces by fast ions. *Ann. Phys.* 47, 555 (1990).
- [279] Ferron, J., Alonso, E. V., Baragiola, R. A. & Oliva-Florio, A. Dependence of ion-electron emission from clean metals on the incidence angle of the projectile. *Phys. Rev. B* 24, 4412 (1981).

- [280] Baragiola, R. A., Alonso, E. V. & Oliva-Florio, A. Electron emission from clean metal surfaces induced by low-energy light ions. *Phys. Rev. B* **19**, 121 (1979).
- [281] Evdokimov, I. N., Mashkova, E. S., Molchanov, V. A. & Odintsov, D. D. Dependence of the ion-electron emission coefficient on the angle of incidence. *Phys. Status Solidi* 19, 407 (1967).
- [282] Hoyle, P. C., Cleaver, J. R. A. & Rack, P. D. Electron beam induced depoisition from $W(CO)_6$ at 2 to 20 kev and its applications. *J. Vac. Sci. Technol. B* **14**, 662 (1996).
- [283] Kunz, R. R. & Mayer, T. M. Summary abstract: Surface reaction enhancement via low energy electron bombardment and secondary electron emission. *J. Vac. Sci. Technol. B* 5, 427 (1987).
- [284] Fowlkes, J. D., Randolph, S. J. & Rack, P. D. Growth and simulation of high-aspect ratio nanopillars by primary and secondary electron-induced deposition. J. Vac. Sci. Technol. B 23, 2825 (2005).

List of publications

Journal contributions

- P. Chen, E. van Veldhoven, C. Sanford, H. Salemink, D. Maas, D. Smith, P. Rack, and P. F. A. Alkemade, Nanopillar growth by focused helium-ion-beam-induced deposition, submitted to *Nanotechnology* (2010).
- P. F. A. Alkemade, P. Chen, E. van Veldhoven, and Diederik Maas, Analytical model for nanopillar growth by focused helium-ion-beam-induced deposition, submitted to *J. Vac. Sci. Technol. B* (2010).
- D. Maas, E. van Veldhoven, P. Chen, V. Sidorkin, H. W. M. Salemink, E. van der Drift, and P. F. A. Alkemade, Nanofabrication with a helium ion microscope, SPIE7638, 14 (2010).
- M-Y. Wu, P. Chen, P. F. A. Alkemade, H. W. M. Salemink, and H. W. Zandbergen, Characterization of the local-coated nanopores fabricated by FIB and IBID in a thin membrane, Accepted by *Micro* (2010).
- P. Chen, H. W. M. Salemink, and P. F. A. Alkemade, Roles of secondary electrons and sputtered atoms in ion-beam-induced deposition, *J. Vac. Sci. Technol. B27*, 2718 (2009).
- P. Chen, H. W. M. Salemink, and P. F. A. Alkemade, Proximity effect in ion-beam-induced deposition of nanopillars, *J. Vac. Sci. Technol. B27*, 1838 (2009).
- P. Chen, M-Y. Wu, H. W. M. Salemink, and P. F. A. Alkemade, Fast single-step fabrication of nanopores, *Nanotechnology* 20, 015302 (2009).
- P. Chen, H. W. M. Salemink, and P. F. A. Alkemade, Smooth and narrow nanopillars fabricated by ion-beam-induced deposition under charging conditions, Jpn. J. Appl. Phys. 47, 8120 (2008).
- P. Chen, P. F. A. Alkemade, and H. W. M. Salemink, The complex mechanisms of ion-beam-induced deposition, *Jpn. J. Appl. Phys.* 47, 5123 (2008).

Conference contributions

- P. Chen, E. van Veldhoven, P. F. A. Alkemade, E. van der Drift, H. W. M. Salemink and D. Mass, Nanopillar growth by helium ion-beam-induced deposition, *Oral presentation* at Netherlands MicroNano Conference '09, Delft, NL, Nov 2009
- P. Chen, H. W. M. Salemink, and P. F. A. Alkemade, Growth rate control of nanopillars fabricated by ion-beam-induced deposition, *Poster presentation* at 35rd International Conference on Micro- and Nano-Engineering 2009, Gent, BE, Sep 2009
- P. Chen, H. W. M. Salemink, and P. F. A. Alkemade, Pillar growth rate dependences in ion-beam-induced deposition, *Poster presentation* at 53rd International Conference on Electron, Ion, and Photon Beam Technology 2009, FL, US, 2009.
- P. Chen, H. W. M. Salemink, and P. F. A. Alkemade, Roles of secondary electrons and sputtered atoms in ion-beam-induced deposition, *Poster presentation* at 53rd International Conference on Electron, Ion, and Photon Beam Technology 2009, FL, US, 2009.
- P. Chen, H. W. M. Salemink, and P. F. A. Alkemade, Ion-beam-induced deposition of platinum", *Poster presentation* at NanoFIB 2009, Oxford UK, 2009.
- P. Chen, H. W. M. Salemink, and P. F. A. Alkemade, Proximity effect in ion-beam-induced deposition of nano-pillars, *Poster presentation* at the 34rd International Conference on Micr- and Nano-Engineering, Athen, Greece, 2008.
- P. Chen, M-Y. Wu, H. W. M. Salemink, and P. F. A. Alkemade, Single step fabrication of nanopores by ion-beam-induced deposition, *Oral presentation* at the 2nd international workshop on Focused Electron-beam-induced Processing (FEBIP), Tune, Switzerland, 2008.
- P. Chen, M-Y. Wu, H. W. M. Salemink, and P. F. A. Alkemade, Nanopillars and nanopores fabricated by ion-beam-induced deposition, *Oral presentation* at MICROSCIENCE 2008, London, UK, 2008.
- P. Chen, M-Y. Wu, H. W. M. Salemink, and P. F. A. Alkemade, Nano-holes fabricated by Ion-beam-induced Deposition, *Poster presentation* at the 4rd European FIB & DualBeamTM UserClub Meeting, Eindhoven, the Netherlands, 2008.
- P. Chen, H. W. M. Salemink, and P. F. A. Alkemade, The complex mechanisms of Ion Beam Induced Deposition, *Poster presentation* at the 20th International Microprocesses and Nanotechnology Conference, Kyoto, Japan, 2007.
- P. Chen, M-Y. Wu, H. W. M. Salemink, and P. F. A. Alkemade, Nano-holes fabricated by Ion-beam-induced Deposition, *Poster presentation* at the 20th International Microprocesses and Nanotechnology Conference, Kyoto, Japan, 2007.

- P. Chen, M-Y. Wu, H. W. M. Salemink, and P. F. A. Alkemade, Nanopillars and nanoholes fabricated by ion-beam-induced Deposition, *Invited talk* at the 33rd International Conference on Micro- and Nano-Engineering, Copenhagen, Denmark, 2007.
- P. Chen, P. F. A. Alkemade and H. W. M. Salemink, Pt nanostructures fabricated by ion-beam-induced deposition, *Oral presentation* at the 3rd European FIB & DualBeamTM UserClub Meeting, Eindhoven, the Netherlands, 2007.

Curriculum Vitae

Ping Chen Date of Birth: September 07, 1979

2006 - 2010	PhD at Delft University of Technology, Delft, the Netherlands
2003 - 2005	Research Assistant in IMEC, Leuven, Belgium
2000 - 2003	Master's degree, Tsinghua University, Beijing, China
1996 - 2000	Bachelor's degree, Tsinghua University, Beijing, China

Acknowledgments

Upon finishing this thesis, I would like to thank my co-promoter Dr. Paul Alkemade and promoter Prof. dr. Huub Salemink who gave me the opportunity to carry out this PhD and their following extensive guidance to help me complete it.

I am grateful for the useful contributions of Emile van Veldhoven and Diederik Maas from TNO Science and Industry, and Mengyue Wu from TU Delft; the helpful discussions of Pieter Kruit, Emile van der Drift, Kees Hagen, Vadim Sidorkin and Ivan Lazić; the technical support of Vladimir Kutchoukov, Ulrike Ziese, Vasili Svechnikov, Tom de Kruijff, Frans Tichelaar, Ron Hoogerheide, and Marc Zuiddam; the administration assistance of Simone Bots and Marja Plas, the English correction of Lilli-Marie Pavka. Special thanks for my officemates Hozan Miro and Vadim Sidorkin for friendship, and all other NAF members for the fun we have shared. I also like to thank my ex-supervisors in IMEC, Wilfried Vandervorst and Tom Janssens, for the knowledge I learned from them and their support on my decision to move to Delft.

To friends I met in Leuven and Delft: indeed, I am used to move all over the world. However, when some of you say nothing can stop me, you should also know that one thread of the kite is still in your hands. Take care.

In the end, I would like to thank my family for their connections with me, which make me comprehend the subtle difference between being independent and alone. It means a lot for a person like me. I appreciate my best friend, colleague – my husband for... He will get what I want to say when I myself do not know. But I am not going to say "This thesis is for my family.", which simply does not make me feel any better for the fact that I could not be there when you needed. I can only give all of you my word "It was the last time I put career over family. This thesis is done.".